NORTHWESTERN UNIVERSITY

The Natural Element Method in Solid Mechanics

A DISSERTATION

SUBMITTED TO THE GRADUATE SCHOOL
IN PARTIAL FULFILLMENT OF THE REQUIREMENTS

for the degree

DOCTOR OF PHILOSOPHY

Field of Theoretical and Applied Mechanics

By

Natarajan Sukumar

EVANSTON, ILLINOIS

June 1998

© Copyright by Natarajan Sukumar 1998
All Rights Reserved

ABSTRACT

The Natural Element Method in Solid Mechanics

Natarajan Sukumar

The Natural Element Method (NEM) is a recently proposed novel numerical tool for the solution of partial differential equations. In this work, the development and application of the natural element method to two-dimensional elliptic boundary value problems in solid mechanics is presented.

We assume the discrete model of a body $\Omega \subset \mathbb{R}^2$ consists of a set of distinct nodes N, and a polygonal description of the boundary $\partial\Omega$. In the natural element method, the trial and test functions are constructed using natural neighbor interpolants. These interpolants are based on the Voronoi tessellation of the set of nodes N. The NEM interpolant is strictly linear between adjacent nodes on the boundary of the convex hull, which facilitates imposition of essential boundary conditions. A methodology to model material discontinuities and non-convex bodies such as cracks is described. A standard displacement-based Galerkin procedure is used to obtain the discrete system of linear equations. Application of NEM to various problems in two-dimensional elastostatics is presented.

The construction and computational implementation of a C^1 natural neighbor interpolant for fourth-order elliptic PDEs is presented. By embedding natural neighbor interpolants in the surface representation of a Bernstein-Bézier cubic simplex, a C^1 interpolant is realized (Farin, 1990b). We present the C^1 formulation and pro-

pose a computational methodology for its numerical implementation for the solution of PDEs. Numerical results for the biharmonic equation with Dirichlet boundary conditions are presented.

A mixed formulation for the natural element method in linear elastostatics is presented. A displacement-pressure mixed formulation is adopted with displacements interpolated by C^0 natural neighbor interpolants; C^0 and C^{-1} interpolation schemes are considered for the interpolation of the pressure. The mixed C^0–C^{-1} NEM formulation alleviates locking in the near incompressible limit ($\nu \to 0.5$) for the elastostatic boundary value problem; moreover, convergence rates in displacement and energy are optimal for all $\nu \in [0, 0.5)$. Results for benchmark problems in compressible and incompressible elasticity are presented.

ACKNOWLEDGMENTS

I am grateful to my advisor, Brian Moran, for his advice and encouragement during the course of my graduate studies at Northwestern University. I also thank Professors Ted Belytschko and Vladimir Volpert for serving on my thesis committee.

The many fruitful discussions over e-mail with Dr. David Watson and Professor Gerald Farin were extremely helpful in formalizing ideas as well as in pursuing new directions in my research. In particular, I thank Dr. Watson for taking the time to share his views and insights on natural neighbor interpolation with me. The contributors to the Usenet newsgroups `sci.math.num-analysis`, `comp.graphics.algorithms`, and `comp.text.tex` deserve special mention for having provided me with tips and answers to many lingering doubts and questions.

I have greatly benefited from the friendship and association with many individuals during the course of my study at Northwestern University. The members of the computational mechanics group have been a valuable source of knowledge in the field of solid mechanics: former graduate students Yi-An Chu, Michael Utschig, Yury Krongauz, Dan Organ, Mark Fleming, and Brian Donning; former post-docs Petr Krysl and Jean-Philippe Ponthot; and current graduate students Charles Gerlach, Laurrie Wittig, Frank Günther, Tom Black, Arancha Alarcón, Yong Guo, Vincent Tan, John Dolbow, Darin Diachin, Mike Singer, and Greg Wagner have contributed to my education-experience. The frequent research discussions with Tom and John over the past year have been especially helpful in developing a better understanding of the theoretical and computational issues in numerical methods.

Finally, I would like to express my whole-hearted gratitude to my parents for the values they instilled in me, and for their love and support in my academic endeavors.

Contents

Abstract **iii**

Acknowledgements **v**

Contents **vi**

List of Figures **ix**

List of Tables **xi**

1 Introduction **1**

2 Galerkin Method for Linear Elliptic Problems **9**
2.1 Linear Functional Analysis 9
2.1.1 Sobolev Spaces 10
2.1.2 Linear Functionals 13
2.1.3 Bilinear Forms 14
2.2 Variational Boundary Value Problem 15
2.3 Galerkin Method 18
2.3.1 Approximability, Stability, and Convergence 20

3 Natural Neighbor Interpolation **24**
3.1 Voronoi Diagram and Delaunay Tessellation 24
3.2 Construction 27
3.3 Properties 33
3.3.1 Interpolation 33
3.3.2 Partition of Unity 34
3.3.3 Linear Completeness 34
3.3.4 Supports and Natural Neighbors 36
3.3.5 Smoothness 39
3.3.6 Interpolation in One-Dimension 42

3.3.7 Interpolation in Two-Dimensions 43
3.3.8 Interpolation in Multi-Dimensions 50
3.3.9 Linear Precision on the Boundary $\partial\Omega$ 50
3.4 Numerical Computational Procedure for NEM Shape Functions . . . 56
3.4.1 Area of a Triangle 56
3.4.2 Circumcenter and Circumradius of a Triangle 57
3.4.3 Shape Function Computations 59
3.4.4 Computational Costs 68
3.5 NEM, FEM, and Meshless Methods 69

4 Natural Element Method for Two-Dimensional Elasticity 72
4.1 Treatment of Material Discontinuities 72
4.2 Modeling of Non-Convex Bodies 74
4.2.1 Enriching the Interpolant for Crack Problems 76
4.3 Governing Equations and Weak Form 78
4.3.1 Strong Form 78
4.3.2 Weak Form 80
4.3.3 Discrete System and NEM Implementation 82
4.4 Numerical Results and Discussions 85
4.4.1 Eigenanalysis 85
4.4.2 Patch Tests 86
4.4.3 Infinite Plate with a Circular Hole 93
4.4.4 Cantilever Beam 98
4.4.5 Hollow Cylinder under Internal Pressure 102
4.4.6 Infinite Plate with an Inclusion 109
4.4.7 Edge-Cracked Plate under Tension 113

5 C^1 Natural Neighbor Interpolant for the Biharmonic Equation 121
5.1 Background 122
5.2 C^1 Natural Neighbor Interpolant 123
5.2.1 Properties 128
5.2.2 NEM Trial Function 132
5.3 Numerical Computation of Shape Functions 135
5.3.1 Bernstein-Bézier Basis Functions 135
5.3.2 Construction of Transformation Matrix [T] 138
5.3.3 Properties 147
5.4 Governing Equations and Weak Form 153
5.5 Numerical Results 157
5.5.1 Airy Stress Function 157
5.5.2 Clamped Circular Plate 161

5.5.3 Eigenanalysis 163

6 Mixed Natural Element Method in Linear Elasticity 170

6.1 Background 170
6.2 Displacement and Pressure Interpolation 173
6.3 Governing Equations and Mixed Formulation 175
6.3.1 Strong Form 175
6.3.2 Weak Form 176
6.3.3 Discrete System for NEM 179
6.4 Numerical Results and Discussions 181
6.4.1 Cantilever Beam 181
6.4.2 Infinite Plate with a Circular Hole 186

7 Conclusions 191

References 196

List of Figures

2.1 Schematic representation of convergence in Galerkin methods. 22

3.1 Geometric structures for a set N of seven nodes. 29
3.2 Construction of natural neighbor coordinates. 31
3.3 Support for NEM shape function. 37
3.4 Voronoi neighbors. 39
3.5 Variation of natural neighbors for a regular grid. 40
3.6 Variation of natural neighbors for an irregular grid. 41
3.7 NEM shape functions in one-dimension. 44
3.8 Barycentric coordinates ($n = 3$). 48
3.9 Bilinear interpolation on a regular grid ($n = 4$). 48
3.10 Linear behavior of $\mathbf{u}^h(\xi)$ along the boundary of a convex domain. . . 53
3.11 Linear behavior of $\mathbf{u}^h(\mathbf{x})$ along the boundary of a non-convex domain. 55
3.12 Circumcenter and circumradius of a triangle. 59
3.13 Computation of natural neighbor shape functions. 62

4.1 Bimaterial configuration ($\Omega = \Omega_1 \cup \Omega_2$). 73
4.2 Crack modeling. 77
4.3 Elastostatic boundary value problem. 78
4.4 Displacement patch test. 90
4.5 Equilibrium (uniaxial tension) patch test. 94
4.6 Plate with a circular hole under tension. 95
4.7 Nodal discretization for the plate with a hole problem. 97
4.8 Comparison of σ_{11} for NEM and the exact solution along a radial line. 98
4.9 Rate of convergence for the plate with a hole problem. 99
4.10 Cantilever beam model. 101
4.11 Nodal discretization for cantilever beam model (85 nodes). 102
4.12 Rate of convergence for the cantilever beam problem. 103
4.13 Comparison of NEM and analytical stresses for the cantilever beam model. 104
4.14 Hollow cylinder under internal pressure p_i. 106

4.15 Sample nodal discretizations for the hollow cylinder under internal pressure problem. 107
4.16 Rate of convergence for the hollow cylinder under internal pressure problem. 108
4.17 Comparison of the radial and hoop stresses for the hollow cylinder under internal pressure problem. 110
4.18 Inclusion embedded in an infinite matrix. 111
4.19 Nodal discretization for inclusion in an infinite matrix problem. . . . 112
4.20 Comparison of NEM and the exact solution for an inclusion with a dilatational eigenstrain in an infinite matrix. 116
4.21 Edge-cracked plate under tension. 119

5.1 Cubic Bernstein-Bézier triangular patch. 125
5.2 Projection of the control net of a cubic tetrahedron onto the plane. . 127
5.3 Evaluation of the Bézier ordinates for a cubic triangular surface patch. 131
5.4 Support for $C^1(\Omega)$ NEM shape function. 136
5.5 Storage structure for the transformation matrix $[\mathbf{T}]$. 142
5.6 Bézier ordinates used in the algorithm for a pentagonal simplex. . . . 142
5.7 Quarter circular plate. 159
5.8 Plot of w and $w_{,r}$ versus r for the Airy stress function problem. . . . 161
5.9 Variation of normalized center displacement with number of nodes for the uniformly loaded clamped circular plate. 164
5.10 Plot of w and $w_{,r}$ versus r for the uniformly loaded clamped circular plate. 165
5.11 Rate of convergence in displacement and energy for the uniformly loaded clamped circular plate. 166

6.1 Rate of convergence in displacement for the cantilever beam problem. 184
6.2 Rate of convergence in energy for the cantilever beam problem. 185
6.3 Variation of the pressure parameter p for the beam model. 186
6.4 Variation of hydrostatic pressure for the beam model. 187
6.5 Rate of convergence in displacement for the plate with a hole problem. 189
6.6 Rate of convergence in energy for the plate with a hole problem. . . . 190

List of Tables

3.1 Pseudo-code for natural neighbor shape function computations at $\mathbf{x}$. . 65

4.1 Linear independence of C^0 shape functions. 87
4.2 Relative error norms for the displacement patch test. 92
4.3 Relative error norms for the equilibrium patch test. 94
4.4 Normalized K_I: Edge-cracked plate under tension. 120

5.1 Pseudo-code for construction of the transformation matrix $[\mathbf{T}]$. 143
5.2 Relative error norms for the Airy stress function problem. 160
5.3 Normalized center displacement for the uniformly loaded circular plate. 163
5.4 Condition number of the mass matrix. 167
5.5 Normalized fundamental frequency for the clamped circular plate. . . 169

6.1 Normalized end displacement for the cantilever beam problem. 183

Chapter 1

Introduction

The Finite Element Method (FEM) is a well-established numerical method which has been applied to boundary value problems in different fields of engineering and the applied sciences. In spite of its numerous advantages and unparalleled success, there is an on-going thrust in the development and application of new numerical tools which hold promise for certain classes of problems, such as crack growth, plate bending, large deformations, higher-order partial differential equations (PDEs), moving phase boundaries, and modeling of multi-scale phenomena. To this end, the emergence of *meshless methods*, a new paradigm for the solution of partial differential equations, has engendered significant interest and is viewed as a step in the right direction.

The term *meshless methods* refers to Galerkin methods in which the *approximant* is constructed solely on the basis of a set of scattered nodes in $\mathbb{R}^d$ ($d = 1, 2, 3$), with no notion of an element structure required to construct the *approximant*. At the outset, we make the pointed distinction between interpolants and approximants—for the former, the function passes through the nodal data, while it is not so in the case of the latter. An element structure is used to construct finite elements which interpolate nodal data. This in essence can be viewed as the key feature that

distinguish finite element methods from meshless methods; it is to be noted that in a Galerkin implementation, a background cell structure is used in both classes of methods for the purpose of numerical integration.

Some of the prominent and widely-used methods that fall under the rubric of meshless methods are: Smoothed Particle Hydrodynamics (Lucy, 1977; Gingold and Monaghan, 1977), Diffuse Element Method (DEM) ((Nayroles, Touzot, and Villon, 1992), Element-Free Galerkin (EFG) (Belytschko, Lu, and Gu, 1994), Material Point Method (MPM) (Sulsky, Chen, and Schreyer, 1994), Reproducing Kernel Particle Method (RKPM) (Liu, Jun, and Zhang, 1995), Finite Point Method (Oñate, Idelsohn, Zienkiewicz, Taylor, and Sacco, 1996), Partition of Unity Method (PUM) (Melenk and Babuška, 1996), and H-p Clouds (Duarte and Oden, 1996). Although differing in forms and construction, most of these methods are strikingly similar in many respect which enables one to view them under a common theoretical framework. Apart from the challenges confronting meshless methods in the realm of solid and fluid mechanics today, it is envisaged that meshless methods could shed light on the mathematical structure and composition of existing finite element methods. As with any Galerkin method, the main ingredients that would demonstrate the robustness of these methods lie in the selection of conforming spaces with good approximability and stability, which would lead to convergence for a broad class of problems in computational mechanics.

Smoothed particle hydrodynamics is a particle method that was pioneered by Lucy (1977) and Gingold and Monaghan (1977) in the late 1970s. The applications of SPH have primarily been focused in the area of hydrodynamics and in the simulation of astrophysical phenomena. Of late, there has been some interest in developing modifications of SPH for elliptic PDEs that arise in computational mechanics. Even

though SPH is not a Galerkin method, its particle-nature renders it as a truly meshless method, and in that sense, it is indeed a desirable end for all meshless methods.

In comparison to SPH, a parallel, but yet distinctly different path was taken by Nayroles, Touzot, and Villon (1992) who proposed the Diffuse Element Method. In DEM, moving least squares (MLS) approximations (Lancaster and Salkauskas, 1981) are used to construct the approximant. Belytschko, Lu, and Gu (1994) modified DEM and substantiated it with supportive examples from solid mechanics and heat conduction to call their implementation as the Element-Free Galerkin method. EFG has been applied to a wide range of problems in solid mechanics, with particular emphasis in the area of computational fracture mechanics, such as two-dimensional and three-dimensional crack growth modeling (Belytschko et al., 1996). In proposing a reproducing kernel method, Liu, Jun, and Zhang (1995) used the continuous kernel (convolution integral) as their starting point. A discrete approximation of the continuous kernel is developed, and by correcting the discrete kernel so as to satisfy the linear reproducing conditions, a linearly complete approximation is realized. If the same weight function with identical support radius for all nodes is used, the MLS approximant is the same as the corrected discrete kernel approximation used in RKPM (Belytschko et al., 1996). In essence, there is no distinction between EFG and RKPM since the approximants are identical; the differences, if any, stem from algorithmic and implementational issues that are adopted in the two methods. The primary focus of RKPM has been in solving computational fluid mechanics problems governed by the compressible Navier-Stokes equations. We remark that contrary to that suggested by its name and the acronym used, RKPM in its current form is a meshless method and not a particle method.

A significant contribution to the mathematical structure and to the understanding of meshless methods was put forth by Melenk and Babuška (1996) and Duarte and Oden (1996). In proposing the partition of unity method, Melenk and Babuška (1996) recognized that meshless methods based on MLS approximations are specific instances of partitions of unity. The essence of PUM lies in the fact that a conforming space is easily constructing by using any system of local approximation spaces without any loss in the approximation properties. As is well-known, creating conforming finite element spaces (C^k, $k > 0$) is a non-trivial task, and in light of this, PUM provides greater flexibility in the choice of local nodal basis functions that can be tailored to the structure of the partial differential equation under consideration. *H-p* clouds (Duarte and Oden, 1996) use moving least squares approximation as a partition of unity to locally enrich approximation spaces. In *H-p* clouds, local approximation spaces are constructed by multiplying a partition of unity by polynomials or other classes of functions, such as $\sqrt{r}$ for crack problems to cite an example. The ease of *p*-adaptivity in *H-p* clouds is particularly attractive and is a very promising element of the method. In the Finite Point Method, Oñate et al. (1996) used a weighted least-squares approximation scheme in conjunction with point collocation to solve fluid mechanics problems. In an attempt to obviate issues involving numerical dissipation of Eulerian methods and mesh distortion of purely Lagrangian methods, Sulsky, Chen, and Schreyer (1994) used a Lagrangian mesh that follow particles and an Eulerian mesh defined over the computational domain in the implementation of the Material Point Method. The interested reader can refer to the review article by Belytschko et al. (1996) and the references therein for further details on meshless methods.

In this thesis, we assess the potential and capabilities of a recently developed

numerical method—coined as Natural Neighbor Finite Elements (Traversoni, 1994) or Natural Element Method (Braun and Sambridge, 1995). A detailed description of its implementation for PDEs is given by Braun and Sambridge (1995), who refer to the method as Natural Element Method (NEM), which is the name we choose to use here. The application of NEM to the solution of elliptic boundary value problems in solid mechanics is explored.

The interpolation scheme used in NEM is known as natural neighbor (n-n) interpolation. Natural neighbor interpolation (Sibson, 1980; Sibson, 1981) is a multivariate data interpolation scheme (Alfeld, 1989), which has primarily been used in data interpolation and modeling of geophysical phenomena. For some of the previous works and typical applications of natural neighbor interpolation, see Watson and Philip (1987), Watson (1988), Gold (1989), Farin (1990b), Owens (1992), Watson (1992), Traversoni (1993), Piper (1993), Watson (1994), Traversoni (1994), Brown (1994), Jones, Owens, and Perry (1995), Robinson (1995), Braun, Sambridge, and McQueen (1995), Braun and Sambridge (1995) and Perez and Traversoni (1996). Natural neighbor interpolation relies on concepts such as Voronoi diagrams (Voronoi, 1908) and Delaunay tessellations (Delaunay, 1934) in computational geometry (Shamos, 1978; Preparata and Shamos, 1985; O'Rourke, 1994), to construct the interpolant. In spite of its fairly simple and appealing structure, sound theoretical basis for construction, and desirable smoothness properties, n-n interpolation has received little attention in the area of multivariate data interpolation, when compared to other schemes such as Shepard's interpolant (Shepard, 1968), moving least squares approximants (Lancaster and Salkauskas, 1981), radial basis functions (Rippa, 1984; Powell, 1987), or Hardy's multiquadrics (Hardy, 1971). Recent work on n-n interpolation (Braun, Sambridge,

and McQueen, 1995) and its application to the modeling of complex fluid-structure interaction phenomena (Braun and Sambridge, 1995) does indicate the merits of the method for the solution of PDEs and suggests that it could be a promising numerical tool in the realm of computational mechanics.

We assume the discrete model of a body $\Omega \subset \mathbb{R}^2$ consists of a set of distinct nodes N, and a polygonal description of the boundary $\partial\Omega$. In the natural element method, the trial and test functions are constructed using natural neighbor interpolants. These interpolants are based on the Voronoi tessellation of the nodal set N. The Voronoi tessellation is a unique geometric structure that partitions the domain into disjoint nodal regions on the basis of shortest Euclidean distances. The interpolants are smooth everywhere, except at the nodes where they are C^0. The NEM interpolant is strictly linear between adjacent nodes on the boundary of the convex hull, which facilitates imposition of essential boundary conditions. In the application of NEM to elliptic PDEs that arise in solid mechanics, a displacement-based Galerkin implementation is used. The trial and test functions in the weak (variational) form are constructed using natural neighbor interpolants. The solution of the discrete system of linear equations $\mathbf{Kd} = \mathbf{f}$ is carried out to obtain the nodal vector $\mathbf{d}$.

Parts of this thesis have been submitted for publication. A significant portion of Chapters 2 and 3 is to appear in Sukumar, Moran, and Belytschko (1998); parts of Chapter 4 are in Sukumar and Moran (1998); and Sukumar (1998) which is based on Chapter 5, is currently in preparation. The outline of this thesis follows.

In Chapter 2, some of the essential elements of a Galerkin method and its approximability, stability, and convergence for elliptic boundary value problems are presented. Prerequisites from functional analysis are first presented, and then in the

interest of a general framework, the abstract variational problem is considered. The Galerkin solution for linear elliptic PDEs is described.

In Chapter 3, a brief description of Voronoi diagrams and Delaunay triangles is first given. Then, an extensive discussion on natural neighbor interpolants that are used in the natural element method is presented. A detailed description of the construction, properties, and computational procedure to evaluate natural neighbor shape functions is outlined.

Chapter 4 focuses on the application of the natural element method in two-dimensional linear elasticity. First, the treatment of material discontinuities is addressed, and then the modeling of non-convex bodies (straight cracks) using NEM is described. Various applications of NEM in two-dimensional solid mechanics, which include problems with homogeneous deformation (patch tests), steep gradients, strain discontinuity (bimaterial interface), as well as those with singularities (crack-tip fields) are presented. The results for the field variables as well as convergence studies are compared to exact (analytical) solutions and to FEM solutions, wherever appropriate.

In Chapter 5, the construction of Farin's (1990) C^1 natural neighbor interpolant is presented, and a computational methodology for its application to PDEs is proposed. The application of the C^1 natural neighbor interpolant to the biharmonic equation with Dirichlet boundary conditions is presented. An eigenanalysis is carried out to ascertain the properties of the discrete approximation spaces and the stability of the C^1 numerical method.

In Chapter 6, we present a displacement-pressure mixed formulation for NEM in linear elasticity. The governing equations (strong form) with validity for both, the compressible and incompressible case are stated. The variational statement for

the mixed formulation and the resulting discrete system of equations are derived. Applications of the mixed natural element method to problems in compressible and near incompressible elasticity are presented.

In Chapter 7, a summary of some of the main results obtained in this work are presented, with some concluding remarks on the potential and promise of the natural element method in computational mechanics.

Chapter 2

Galerkin Method for Linear Elliptic Problems

In this chapter, some of the main ingredients of variational boundary value problems, and the approximability, stability, and convergence of Galerkin approximations for elliptic problems is presented. To this end, we first briefly touch upon some of the essential concepts of linear functional analysis. In order to fix ideas, we consider the abstract variational problem as the basis for the exposition, and as an example, the weak formulation for the Poisson equation is derived. The approximate solution using a Galerkin method is presented, and some remarks on the convergence of Galerkin methods are mentioned. For essential prerequisites on functional analysis and cogent presentations on the mathematical aspects of elliptic boundary value problems, the texts of Strang and Fix (1973), Ciarlet (1978), Braess (1997), and Reddy (1998) are particularly noteworthy.

2.1 Linear Functional Analysis

Concepts from linear functional analysis are central to a qualitative understanding of boundary value problems of mathematical physics. The notion of function spaces

in describing the topology of functions in $\mathbb{R}^d$ is analogous to that of vector spaces in linear algebra. In operator notation, if one considers the PDE $Au = f$, we note that the operator $A : U \to V$ maps functions from one function space U to another function space V. Hence it is apparent that the choice and suitability of function spaces is of significance and demands attention in the analysis of PDEs. Sobolev spaces (Adams, 1975) are the proper setting in order to study partial differential equations. We first briefly discuss Sobolev spaces with emphasis on a particular class of spaces known as Hilbert spaces, and then present linear functionals and bilinear forms which play a vital role in the study of linear boundary value problems. The foundations and theoretical basis are presented for scalar-valued functions; the theory, however, readily extends to vector-valued functions.

2.1.1 Sobolev Spaces

Let Ω be an open bounded domain in $\mathbb{R}^d$ with a piecewise smooth boundary Γ. In order to study linear elliptic PDEs, we consider real Sobolev spaces that are built on the function space $L^2(\Omega)$, where $L^2(\Omega)$ consists of functions that are square-integrable in the sense of Lebesgue:

$$L^2(\Omega) = \left\{ f : \int_\Omega f^2 \, d\Omega < +\infty \right\}. \tag{2.1}$$

The space $L^2(\Omega)$ with the scalar product

$$(u, v)_{L^2(\Omega)} = \int_\Omega uv \, d\Omega, \quad u, \, v \in L^2(\Omega) \tag{2.2}$$

and the associated norm $\|u\|_{L^2(\Omega)} = (u,u)^{1/2}_{L^2(\Omega)}$ becomes a Hilbert space.

As an aid to what follows, we first introduce two definition—multi-index notation and the notion of a *weak derivative*.

Multi-Index Notation. Let $\mathbb{Z}^n_+$ denote the set of all ordered n-tuples of non-negative integers: a member $\alpha \in \mathbb{Z}^n_+$ is denoted by $\alpha = (\alpha_1, \alpha_2, \cdots, \alpha_n)$, where each component α_i is a non-negative integer. The norm of α is denoted by $|\alpha|$ with $|\alpha| = \alpha_1 + \alpha_2 + \cdots + \alpha_n$ and the partial derivative $D^\alpha u$ is given by

$$D^\alpha u = \frac{\partial^{|\alpha|} u}{\partial x_1^{\alpha_1} \partial x_2^{\alpha_2} \cdots \partial x_n^{\alpha_n}}. \tag{2.3}$$

Weak Derivative. We denote $C_0^\infty(\Omega)$ as the space of infinitely differentiable functions which are non-zero only on a compact subset of Ω. If $u \in L^2(\Omega)$ is a locally integrable function, we say that u possesses the (weak) derivative $v = D^\alpha u$ in $L^2(\Omega)$ provided that $v \in L^2(\Omega)$ and

$$\langle v, \phi \rangle = (-1)^{|\alpha|} \langle u, D^\alpha \phi \rangle \quad \forall\ \phi \in C_0^\infty(\Omega) \tag{2.4}$$

in the sense of distributions.

The Sobolev space of order m, denoted by $H^m(\Omega)$, is defined as the space consisting of those functions in $L^2(\Omega)$ that, together with all their *weak partial derivatives* up to order m, belong to $L^2(\Omega)$:

$$H^m(\Omega) = \{u : D^\alpha u \in L^2(\Omega)\ \forall\ |\alpha| \leq m\}. \tag{2.5}$$

We introduce the Sobolev inner product $(\cdot,\cdot)_{H^m(\Omega)}$ to make $H^m(\Omega)$ an inner product space:

$$(u,v)_{H^m(\Omega)} = \sum_{|\alpha|\leq m} (D^\alpha u, D^\alpha v)_{L^2(\Omega)} \text{ for } u,\ v \in H^m(\Omega). \tag{2.6}$$

The inner product space induces the Sobolev norm $\|\cdot\|_{H^m(\Omega)}$ which is defined as

$$\|u\|^2_{H^m(\Omega)} = (u,u)_{H^m(\Omega)} = \sum_{|\alpha|\leq m} (D^\alpha u, D^\alpha u)_{L^2(\Omega)}. \tag{2.7}$$

We note that the Hilbert space $H^0(\Omega) = L^2(\Omega)$. The family of semi-norms $|\cdot|_{H^m(\Omega)}$ on the Hilbert space are defined as

$$|u|^2_{H^m(\Omega)} = \sum_{|\alpha|=m} (D^\alpha u, D^\alpha u)_{L^2(\Omega)}. \tag{2.8}$$

The distinction between the norm and the semi-norm is that the semi-norm does not satisfy the axiom of positive-definiteness; semi-norms are only positive-semidefinite. The relevance of semi-norms stem from the fact that $|\cdot|_{H^m(\Omega)}$ is a norm on $H^m_0(\Omega)$ and is equivalent to the H^m-norm, which is a consequence of the Poincaré-Friedrichs inequality (Ciarlet, 1978).

As a final remark on Sobolev spaces, we mention the Sobolev space $H^m_0(\Omega)$ which is the appropriate space for test functions (and also trial functions for the homogeneous Dirichlet problem) in Galerkin approximations of linear elliptic PDEs of order $2m$. For a rigorous and complete definition of $H^m_0(\Omega)$ that is based on the trace operator, see Ciarlet (1978). For the homogeneous Dirichlet problem, $H^m_0(\Omega)$ is a subspace of $H^m(\Omega)$ functions that, together with their derivatives of order less than m vanish on

the boundary $\Gamma = \partial\Omega$. In the context of this work, the cases $m = 1$ and $m = 2$ are of particular interest. For scalar-valued functions, the Sobolev spaces $H_0^1(\Omega)$ and $H_0^2(\Omega)$ are defined as:

$$H_0^1(\Omega) = \{v : v \in H^1(\Omega),\ v = 0 \text{ on } \Gamma\}, \tag{2.9a}$$

$$H_0^2(\Omega) = \{v : v \in H^2(\Omega),\ v = 0,\ \partial v/\partial n = 0 \text{ on } \Gamma\}, \tag{2.9b}$$

where n is the outward normal direction to Ω.

2.1.2 Linear Functionals

We consider linear functionals $l : V \to \mathbb{R}$ that map real-valued functions from a Hilbert space V to real numbers in $\mathbb{R}$. The functional l is defined by its action on an arbitrary member $v \in V$ by

$$\langle l, v\rangle = (u, v)_{L^2(\Omega)} \tag{2.10}$$

for a given u and arbitrary v. The notation $\langle\cdot,\cdot\rangle$ is used to denote the duality pair. The space of bounded linear functionals on V is denoted by the dual space V', and for $l \in V'$ the norm $\|l\|_{V'}$ is defined as

$$\|l\|_{V'} = \sup_{v \in V\setminus\{0\}} \frac{\langle l, v\rangle}{\|v\|_V}. \tag{2.11}$$

The continuity of l is met if there exists a positive constant M such that

$$|\langle l, v\rangle| \leq M\|v\|_V. \tag{2.12}$$

The above equation is satisfied for $M = \|u\|_V$, a consequence of using the Cauchy-Schwartz inequality in Eq. (2.10), and it is easily shown that $\|l\|_{V'} = \|u\|_V$. The norm $\|l\|_{V'}$ is of relevance in ascertaining if the solution is continuously dependent on the data.

2.1.3 Bilinear Forms

Let us consider the bilinear form $a(u, v) : U \times V \to \mathbb{R}$ that maps pair of functions from Hilbert spaces U and V to real numbers in $\mathbb{R}$. The operator $a(\cdot, \cdot)$ is linear in both slots; hence the term bilinear. We outline some of the most important properties of bilinear forms that are germane to the existence and uniqueness of solutions for linear elliptic PDEs.

Continuity Consider Hilbert spaces U and V. A bilinear form $a(u, v) : U \times V \to \mathbb{R}$ is continuous if

$$|a(u, v)| \leq K\|u\|_U \|v\|_V \quad \forall\ u \in U,\ v \in V \tag{2.13}$$

for a positive constant K.

Ellipticity Let $v \in V$, where V is a Hilbert space. The V-ellipticity (coercivity) condition points to the positive-definiteness of the bilinear form $a(\cdot, \cdot)$:

$$a(v, v) \geq \alpha \|v\|_V^2 \tag{2.14}$$

for a constant $\alpha > 0$. If v is a finite-dimensional approximation and the bilinear form $a(v,v) = \mathbf{v}^T\mathbf{A}\mathbf{v}$, then the ellipticity condition indicates the existence of the inverse matrix $\mathbf{A}^{-1}$ and the fact that $\|\mathbf{A}^{-1}\|$ is bounded away from zero. In linear elasticity, the ellipticity of the continuous bilinear operator is a consequence of the positive-definiteness of the strain (stored) energy.

2.2 Variational Boundary Value Problem

Consider a Hilbert space V, and let $a(u,v) : V \times V \to \mathbb{R}$ be a continuous, V-elliptic bilinear form on V. In addition, let $l : V \to \mathbb{R}$ be a continuous linear functional on V. We consider the abstract variational boundary value problem:

$$a(u,v) = \langle l, v \rangle \quad \forall\, v \in V. \tag{2.15}$$

The well-posedness of the variational problem—existence and uniqueness of u with u being continuously dependent on the data, is a consequence of the Lax-Milgram theorem (Ciarlet, 1978). From a physical viewpoint, any linear problem that arises from a variational principle which involves the minimization (critical point) of a quadratic functional (potential energy functional in linear elasticity) has the above form. The minimizing problem is posed as:

$$\inf_{u \in V} J(u) = \inf_{u \in V} \frac{1}{2} a(u,u) - \langle l, u \rangle. \tag{2.16}$$

The weak form, however, is more general with no dependence on the existence of a variational principle. The required regularity (smoothness) of the solution $u \in H^s(\Omega)$

is also inferred on the basis of the condition that the integrands in the weak formulation are square-integrable. The variational problem posed in Eq. (2.15) can be obtained by an extremal variational principle (compressible elasticity) or by a stationary functional as in a saddle-point principle (incompressible elasticity).

Let us consider $2m$-order elliptic boundary value problems, where $2m$ is the order of the highest derivative of the primary variable in the partial differential equation. We partition the set of boundary conditions into two subsets: essential boundary conditions which are of order $< m$ and natural boundary conditions which are of order $\geq m$. This allows one to formulate the variational problem such that the solution is required only in a subspace of $H^m(\Omega)$ (Strang and Fix, 1973).

In order to illustrate the derivation of the weak formulation, we consider the Poisson equation with Dirichlet boundary conditions:

$$-\nabla^2 u = f \quad \text{in } \Omega, \tag{2.17a}$$

$$u = 0 \quad \text{on } \Gamma, \tag{2.17b}$$

where $\Omega \subset \mathbb{R}^2$ is an open bounded domain and the data f is assumed to be sufficiently smooth. Since $m = 1$ for the Poisson equation and only homogeneous Dirichlet boundary conditions are prescribed, we choose $V = H_0^1(\Omega)$. Now, on multiplying the above equation by an arbitrary function $v \in V$ and integrating over Ω, we obtain

$$-\int_\Omega (\nabla^2 u) v \, d\Omega = \int_\Omega f v \, d\Omega. \tag{2.18}$$

By Green's formulas, we have the identities:

$$\int_\Omega v\nabla^2 u\, d\Omega = -\int_\Omega \boldsymbol{\nabla} u \cdot \boldsymbol{\nabla} v\, d\Omega + \int_\Gamma v\frac{\partial u}{\partial n}\, d\Gamma, \tag{2.19a}$$

$$\int_\Omega (u\nabla^2 v - v\nabla^2 u)\, d\Omega = \int_\Gamma \left(u\frac{\partial v}{\partial n} - v\frac{\partial u}{\partial n}\right) d\Gamma, \tag{2.19b}$$

where n is the outward normal direction to Ω. Since $v = 0$ on Γ by Eq. (2.17b), the boundary integral in Eq. (2.19a) vanishes, and hence Eq. (2.18) can be written as

$$\int_\Omega \boldsymbol{\nabla} u \cdot \boldsymbol{\nabla} v\, d\Omega = \int_\Omega f v\, d\Omega \tag{2.20}$$

which is known as the weak or variational form. Comparing Eq. (2.17) to the abstract variational form in Eq. (2.15), we have $V = H_0^1(\Omega)$ and

$$a(u,v) = \int_\Omega \boldsymbol{\nabla} u \cdot \boldsymbol{\nabla} v\, d\Omega, \quad \langle l, v\rangle = \int_\Omega f v\, d\Omega. \tag{2.21}$$

It is noted that by re-casting Eq. (2.17) in its weak form, the Poisson system in Eq. (2.17) is satisfied in the distributional sense—see Section 2.1.1. The bilinear form in Eq. (2.21) is symmetric, and the space of admissible trial functions has been enlarged from $H^2(\Omega)$ to $H^1(\Omega)$ by transforming the strong form to its associated weak or variational form. Thus, as the name suggests, the weak form in Eq. (2.21) permits weak solutions to the Poisson equation.

2.3 Galerkin Method

In the variational boundary value problem stated in Eq. (2.15), V is an infinite-dimensional subspace of the Hilbert space H. In order to present an approximate solution, we choose a finite-dimensional subspace $V^h \subset V$ which is spanned by the shape functions ϕ_I, ϕ_2, ... , ϕ_M:

$$V^h = \text{span } \{\phi_I\}_{I=1}^{M}, \tag{2.22}$$

where h refers to a measure of the distance between nodes or the element size in case of finite elements. If the number of shape functions gets larger ($M \to \infty$), then $h \to 0$. The variational form for the discrete system can now be written as:

$$a(u^h, v^h) = \langle l, v^h \rangle \quad \forall\ v^h \in V^h. \tag{2.23}$$

The above equation is the statement of the Galerkin method. In a Bubnov-Galerkin or Ritz-Galerkin method, both the trial function u^h and the arbitrary test function v^h are expressed as linear combinations of the same shape functions. In Petrov-Galerkin methods, u^h and v^h are chosen from different finite-dimensional subspaces. We can express u^h and v^h for a Bubnov-Galerkin method as

$$u^h = \sum_{I=1}^{M} \phi_I u_I, \quad v^h = \sum_{I=1}^{M} \phi_I v_I. \tag{2.24}$$

Substituting Eq. (2.24) in Eq. (2.23) and noting that a is bilinear and l is linear, we obtain

$$\sum_{I=1}^{M}\sum_{J=1}^{M} a(\phi_I, \phi_J) u_I v_J = \sum_{J=1}^{M} \langle l, \phi_J \rangle v_J \tag{2.25}$$

which can be written as

$$\sum_{J=1}^{M} v_J \left(\sum_{I=1}^{M} K_{IJ} u_I - f_J \right) = 0, \tag{2.26a}$$

where

$$K_{IJ} = a(\phi_I, \phi_J), \quad f_J = \langle l, \phi_J \rangle. \tag{2.26b}$$

Since the coefficients in Eq. (2.26a) are arbitrary, the term within the parentheses must be identically equal to zero, which results in the following discrete matrix system:

$$\mathbf{K}\mathbf{u} = \mathbf{f}, \tag{2.27}$$

where the symmetry of $\mathbf{K}$ has been used to arrive at the above equation. In solid mechanics, the matrix $\mathbf{K}$ is referred to as the stiffness matrix and $\mathbf{f}$ is the external force vector. For displacement-based finite element methods or for the natural element method, $\mathbf{u}$ is the nodal displacement vector, while for meshless methods such as EFG, $\mathbf{u}$ is the vector of nodal coefficients. In a Bubnov-Galerkin method, the stiffness matrix is symmetric and also positive definite when rigid-body translation and rotation modes are removed. For Petrov-Galerkin methods, a non-symmetric $\mathbf{K}$

matrix is obtained. It is noted that, in general, only few shape functions are non-zero in the summation in Eq. (2.24). For instance, in finite elements, for a point $\mathbf{x}$ in the interior of an element E, only the shape functions associated with the nodes in the connectivity of E are non-zero at $\mathbf{x}$.

2.3.1 Approximability, Stability, and Convergence

Having outlined the Galerkin method for the numerical solution of elliptic PDEs, the crux that remains is in ascertaining the approximability, stability, and convergence properties of the numerical method. The presentation that ensues closely follows that pursued by Arnold (1990).

Let $u \in V = H^m(\Omega)$ and u^h, $v^h \in V^h \subset V$ for a Dirichlet problem. We consider a suitable norm such as the energy norm $\|v\|_V := \big(a(v,v)\big)^{1/2}$. By virtue of continuity and ellipticity of the bilinear form, we have $\alpha\|v\|_V^2 \leq a(v,v) \leq K\|v\|_V^2$, and hence the energy norm is an equivalent norm to the H^m-norm in V. The approximability and convergence of a Galerkin method are measured by the quantities

$$\inf_{v^h \in V^h} \|u - v^h\| \quad \text{and} \quad \|u - u^h\|, \tag{2.28}$$

respectively. In order to quantify stability, the dual norm indicated in Eq. (2.11) is used:

$$\|l\|_{V'} = \sup_{v^h \in V^h \setminus \{0\}} \frac{\langle l, v \rangle}{\|v^h\|_V} \tag{2.29}$$

for $l : V^h \to \mathbb{R}$. Then, the stability constant for the Galerkin method is given by

$$M = \sup_{l:V^h \to \mathbb{R}} \frac{\|u^h\|_V}{\|l\|_{V'}} \tag{2.30}$$

which indicates that the stability constant is the largest value attained by the ratio of the solution to the discrete problem to that of the dual norm generated by the data. The stability constant $M = 1/\alpha$ where α is defined in Eq. (2.14). For the discrete problem, the stability constant is just the norm of the inverse matrix. The fundamental relation between approximability, stability, and convergence is given by Céa's lemma (Ciarlet, 1978):

$$\boxed{\|u - u^h\| \leq C \inf_{v^h \in V^h} \|u - v^h\|.} \tag{2.31}$$

Hence if the subspaces V^h of V are such that, for each $u \in V$

$$\lim_{h \to 0} \inf_{v^h \in V^h} \|u - v^h\| = 0, \tag{2.32}$$

then convergence is attained and u^h converges to u at the same rate as the best approximation. By the property of continuity and ellipticity of the bilinear form $a(\cdot, \cdot)$, an estimate $C = K/\alpha$ is obtained; if the bilinear form is symmetric, an even tighter bound $C = \sqrt{(K/\alpha)}$ is realized (Ciarlet, 1978), where K and α are defined in Eqs. (2.13) and (2.14). As seen above, good approximability in tandem with stability leads to approximate solutions that converge to the exact solution at the same rate as the best approximation. The sufficiency condition in Eq. (2.31) indicates that the error estimate $\|u - u^h\|$ is reduced to finding the distance $d(u, V^h) = \inf_{v^h \in V^h} \|u - v^h\|$

between a function $u \in V$ and a subspace $V^h \subset V$ (Fig. 2.1). Typically, the distance is in itself bounded by a constant times an exponent of the nodal spacing h. If the bilinear form is smooth and satisfies the continuity and ellipticity conditions given in Eqs. (2.13) and (2.14), then for linear elliptic problems of order $2m$, we have the estimate (Strang and Fix, 1973)

$$\|u - u^h\|_s \leq \begin{cases} Ch^{k-s}\|u\|_k & \text{if } s \geq 2m-k, \\ Ch^{2(k-m)}\|u\|_k & \text{if } s \leq 2m-k, \end{cases} \tag{2.33}$$

where C is a constant independent of h. In the above equation, the trial space is assumed to possess $k-1$ completeness ($k = 2$ for an approximation space with linear completeness), and the exponent of h is known as the rate of convergence. For linear elliptic PDEs of order $2m$, mth order derivatives appear in the weak form. Clearly, in this case, optimal convergence in H^s-norms ($s \leq m$) is attained if and only if $k > m$.

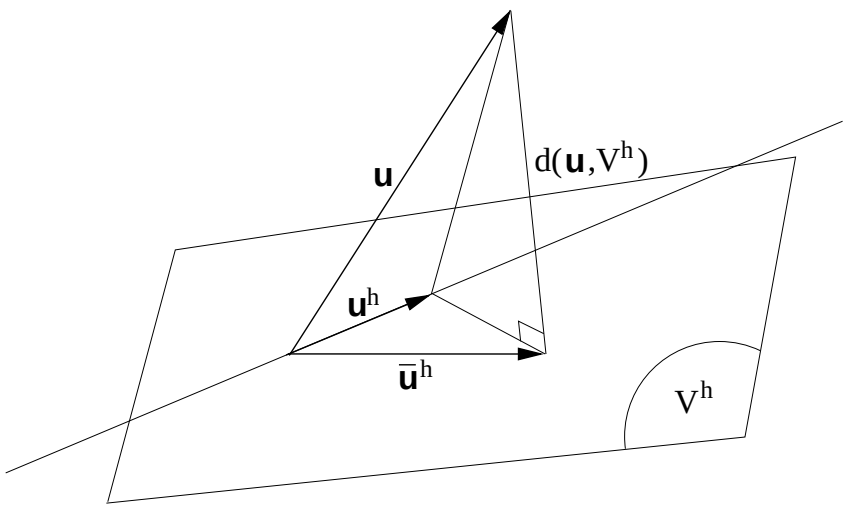

Figure 2.1: Schematic representation of convergence in Galerkin methods.

For displacement-based Galerkin methods in linear elasticity, the bilinear form is symmetric and V-elliptic, and hence stability and convergence are readily established (Ciarlet, 1978). As opposed to displacement methods, in mixed methods based on incompressible (or near incompressible) elasticity, the bilinear form is not coercive, and hence a stability condition termed as inf-sup or LBB (Ladyzhenskaya, 1969; Babuška, 1971; Brezzi, 1974) must be satisfied for convergence.

Chapter 3

Natural Neighbor Interpolation

In this chapter, a detailed description of the construction, properties, and numerical computations of natural neighbor shape functions is presented. Issues pertaining to the imposition of essential boundary conditions and the exact correspondence of NEM with finite elements in one-dimension are also discussed. As a preliminary introduction and a means to set the stage for what follows, we first present a brief description of Voronoi diagrams and Delaunay triangles in the context of natural neighbor interpolation.

3.1 Voronoi Diagram and Delaunay Tessellation

The Voronoi diagram and its dual Delaunay tessellation (covering of a surface with tiles) are one of the most fundamental and useful geometric constructs that define an irregular set of points (nodes). For simplicity, and in keeping with the applications that are pursued in this work, we consider two-dimensional Euclidean space $\mathbb{R}^2$; the theory, however, is applicable in a general d-dimensional framework. Consider a set of distinct nodes $N = \{n_1, n_2, \ldots, n_M\}$ in $\mathbb{R}^2$. The Voronoi diagram (or $1st$-order Voronoi diagram) of the set N is a subdivision of the plane into regions T_I (closed

and convex, or unbounded), where each region T_I is associated with a node n_I, such that any point in T_I is closer to n_I (nearest neighbor) than to any other node $n_J \in N$ $(J \neq I)$—T_I is the locus of points closer to n_I than to any other node. The regions T_I are the Voronoi cells (also known as Thiessen or Voronoi polygons) of n_I. In mathematical terms, the Voronoi polygon T_I is defined as (Green and Sibson, 1978)

$$T_I = \{\mathbf{x} \in \mathbb{R}^2 \,:\, d(\mathbf{x}, \mathbf{x}_I) < d(\mathbf{x}, \mathbf{x}_J) \;\forall\; J \neq I\}, \tag{3.1}$$

where $d(\mathbf{x}_I, \mathbf{x}_J)$, the Euclidean metric, is the distance between $\mathbf{x}_I$ and $\mathbf{x}_J$. The Voronoi cell for node A and the Voronoi diagram for a set N consisting of seven nodes are shown in Figures 3.1a and 3.1b, respectively. In Fig. 3.1a it is seen that each Voronoi cell T_I is the intersection of finitely many open half-spaces, each being delimited by the perpendicular bisector (hyperplane in $\mathbb{R}^d$) of the line joining nodes n_I and n_J $(J \neq I)$. Consequently, for all nodes n_I that are inside the convex hull[1], the Voronoi cells are closed and convex, while the cells associated with nodes on the boundary of the convex hull are unbounded (see Fig. 3.1b). The nearest neighbor problem and many of its variants in computational geometry are prototypical examples that illustrate the use of Voronoi diagrams. However, the implications of Voronoi diagrams are far-reaching, with many applications in the natural sciences, physical sciences, and engineering. A detailed description of the properties and applications of Voronoi diagrams can be found in Boots (1986) and Okabe, Boots, and Sugihara (1992), while Aurenhammer (1996) presents a comprehensive review of Voronoi polygons.

The Delaunay triangulation, which is the straight-line dual of the Voronoi di-

[1]The convex hull CH(N) of the set of nodes N is the smallest convex set containing N.

agram, is constructed by connecting the nodes whose Voronoi cells have common boundaries—see Fig. 3.1c. The duality between the two implies that there is a Delaunay edge between two nodes in the plane if and only if their Voronoi cells share a common edge. Among all triangles, the Delaunay triangles maximize the minimum angle (Lawson, 1977). Another important property of Delaunay triangles is the *empty circumcircle criterion* (Lawson, 1977)—if $\mathrm{DT}(n_J, n_K, n_L)$ is any Delaunay triangle of the nodal set N, then the circumcircle of DT contains no other nodes of N. In the context of natural neighbor interpolation, these circles are known as natural neighbor circumcircles (Watson, 1992). The center of the natural neighbor circumcircle is a vertex of the Voronoi cell. If the nodal set N is such that only three nodes lie on the circumcircle of any Delaunay triangle (non-degenerate case), then precisely three edges meet to form a Voronoi vertex. In Fig. 3.1d, the natural neighbor circumcircles and the associated Delaunay triangulation are shown.

From an algorithmic viewpoint, since the Voronoi diagram and the Delaunay triangulation share a common bond (duality), the combinatorial structure of either structure is completely determined from its dual. The Voronoi diagram in $\mathbb{R}^d$ is also closely related to the convex hull in $\mathbb{R}^{d+1}$ (Brown, 1979), which is also the basis for computing the Voronoi diagram in $\mathbb{R}^d$. The importance of the Delaunay triangulation in the context of the solution of PDEs stems from its use in mesh generation for the finite element method. Incremental insertion (Lawson, 1977) and point insertion (Bowyer, 1981; Watson, 1981) are among the early algorithms developed to compute Delaunay triangulations. Today, some of the prominent Delaunay triangulation algorithms are those based on incremental insertion (Lawson, 1977), divide-and-conquer (Lee and Schachter, 1980), and plane sweep (Fortune, 1987). The optimum time-complexity of

Delaunay triangulation algorithms is $\mathcal{O}(n \log n)$. Shewchuk (1996c) has carried out a comparison of the computational costs and speeds of the above three algorithms. In this work, we use the package *Triangle* (Shewchuk, 1996b); the nodal discretization and Delaunay triangles are displayed using the package *Show Me* (Shewchuk, 1996a). In three-dimensions and higher, the *qhull* package (Barber and Huhdanpaa, 1994; Barber, Dobkin, and Huhdanpaa, 1996) which is based on the quickhull algorithm is considered to be the most versatile. A discussion on randomized algorithms to compute Voronoi diagrams and Delaunayq tessellations can be found in Mulmuley (1994). For details on Delaunay triangulation and mesh generation, see Fortune (1995) and the review article by Bern and Eppstein (1995).

3.2 Construction

Natural neighbor coordinates were introduced by Sibson (1980) as a means for data interpolation and smoothing. The concept of nearest neighbors and neighboring nodes is embedded in the first-order Voronoi diagram (Section 3.1). By a similar extension, one can construct higher order (k-order, $k > 1$) Voronoi diagrams in the plane. Of particular interest in the context of natural neighbor coordinates is the case $k = 2$, which is the second-order Voronoi diagram. The second-order Voronoi diagram of the set of nodes N is a subdivision of the plane into cells T_{IJ} , where each region T_{IJ} is associated with a nodal-neighbor-pair (n_I, n_J) (k-tuple for the k-order Voronoi diagram), such that T_{IJ} is the locus of all points that have n_I as the nearest neighbor, and n_J as the second nearest neighbor. It is emphasized that the cell T_{IJ} is non-empty if and only if n_I and n_J are neighbors. The second-order Voronoi cell T_{IJ} $(I \neq J)$ is

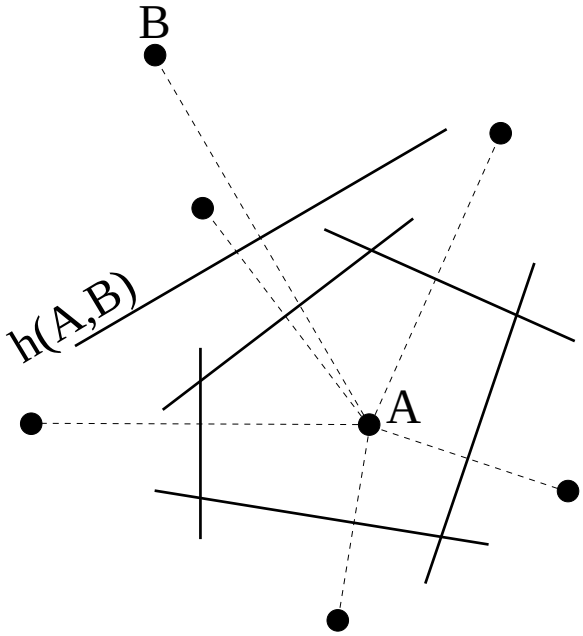

(a)

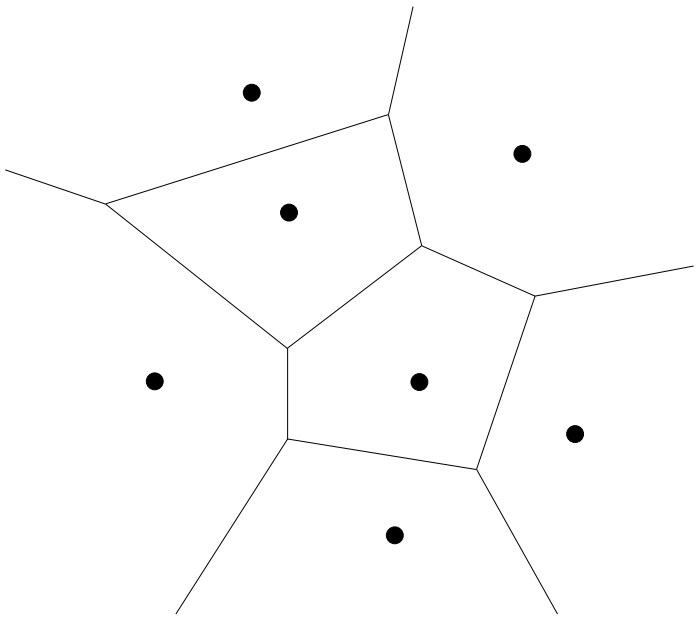

(b)

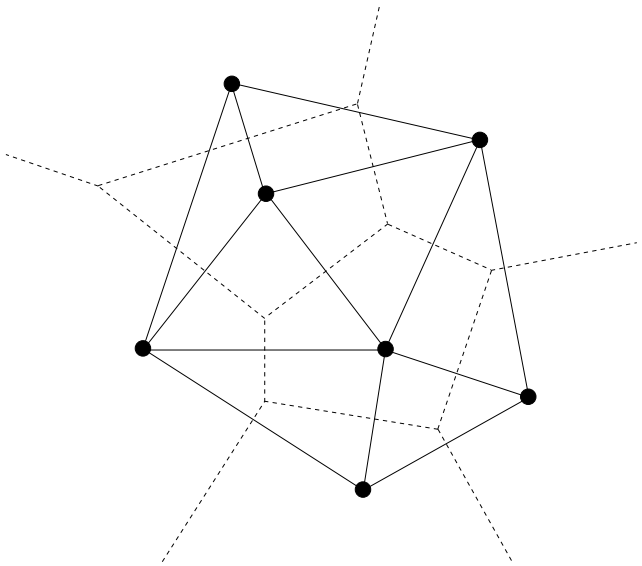

(c)

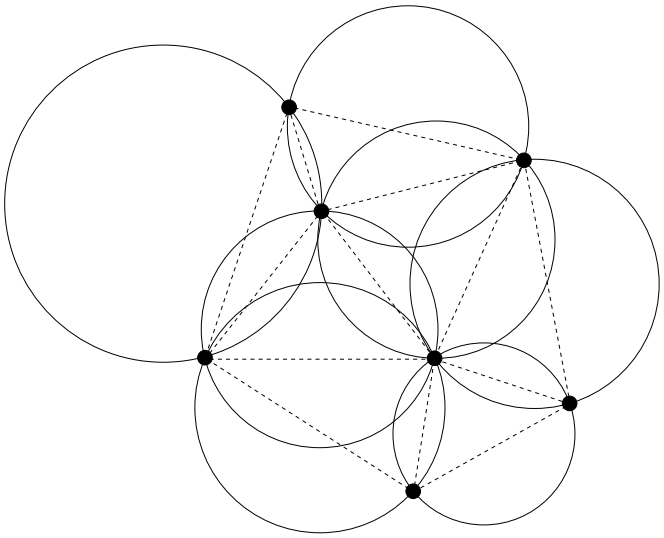

(d)

Figure 3.1: Geometric structures for a set N of seven nodes. (a) Voronoi cell for node A, (b) Voronoi diagram $V(N)$, (c) Delaunay triangulation $\mathrm{DT}(N)$, and (d) Natural neighbor circumcircles.

defined as (Sibson, 1980)

$$T_{IJ} = \{\mathbf{x} \in \mathbb{R}^2 \,:\, d(\mathbf{x}, \mathbf{x}_I) < d(\mathbf{x}, \mathbf{x}_J) < d(\mathbf{x}, \mathbf{x}_K) \;\forall\; K \neq I,\, J\}. \tag{3.2}$$

In order to quantify the neighbor relation for any point $\mathbf{x}$ introduced into the tessellation, Sibson (1980) used the concept of second-order Voronoi cells, and thereby introduced natural neighbors and natural neighbor coordinates. The notion of neighboring nodes is broadened and generalized to yield a new measure of "neighborliness" by the definition of natural neighbors. In Fig. 3.2a, a point $\mathbf{x}$ is introduced into the Voronoi diagram of the set N discussed in Section 3.1. If $\mathbf{x}$ is tessellated along with the set of nodes N, then the natural neighbors of $\mathbf{x}$ are those nodes which form an edge of a triangle with $\mathbf{x}$ in the new triangulation. A straight-forward means to arrive at the same end is to use the empty circumcircle criterion (see Section 3.1). By doing so, we arrive at the result that if $\mathbf{x}$ lies within the circumcircle of triangle $\mathrm{DT}(n_I, n_J, n_K)$, then n_I, n_J, and n_K are its natural neighbors. In Fig. 3.2b, the perpendicular bisectors from point $\mathbf{x}$ to its natural neighbors are constructed and the Voronoi cell $T_{\mathbf{x}}$ (closed polygon $abcd$) is obtained. It is observed that $\mathbf{x}$ has four ($n = 4$) natural neighbors, namely nodes 1, 2, 3, and 4.

Let $\kappa(\mathbf{x})$ be a Lebesgue measure (length, area, or volume in 1D, 2D, or 3D, respectively) of $T_{\mathbf{x}}$, and $\kappa_I(\mathbf{x})$ (I = 1–4) be that of $T_{\mathbf{x}I}$. In two-dimensions, the measures are areas, and hence we denote $A(\mathbf{x}) \equiv \kappa(\mathbf{x})$ and $A_I(\mathbf{x}) \equiv \kappa_I(\mathbf{x})$. The natural neighbor coordinates of $\mathbf{x}$ with respect to a natural neighbor I is defined as the ratio of the area of overlap of the Voronoi cells T_I and $T_{\mathbf{x}}$ to the total area of the

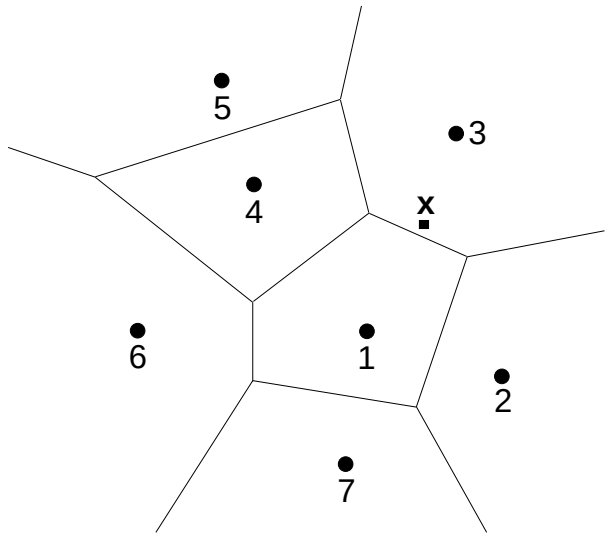

(a)

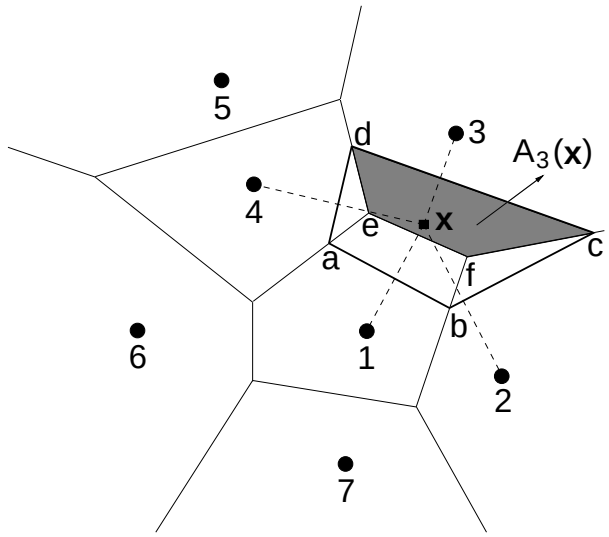

(b)

Figure 3.2: Construction of natural neighbor coordinates. (a) Original Voronoi diagram and $\mathbf{x}$, and (b) $1st$-order and $2nd$-order Voronoi cells about $\mathbf{x}$.

Voronoi cell of $\mathbf{x}$:

$$\phi_I(\mathbf{x}) = \frac{A_I(\mathbf{x})}{A(\mathbf{x})}, \tag{3.3}$$

where I ranges from 1 to n, and $A(\mathbf{x}) = \sum_{J=1}^{n} A_J(\mathbf{x})$. The four regions shown in Fig. 3.2b are the second-order cells, while their union (closed polygon *abcd*) is a first-order Voronoi cell. Referring to Fig. 3.2, the shape function $\phi_3(\mathbf{x})$ is given by

$$\phi_3(\mathbf{x}) = \frac{A_3(\mathbf{x})}{A(\mathbf{x})}. \tag{3.4}$$

The derivatives of the n-n coordinates are obtained by differentiating Eq. (3.3):

$$\phi_{I,j}(\mathbf{x}) = \frac{A_{I,j}(\mathbf{x}) - \phi_I(\mathbf{x})A_{,j}(\mathbf{x})}{A(\mathbf{x})} \quad (j = 1, 2), \tag{3.5}$$

where Eq. (3.3) has been used to arrive at the above expression.

Let $\mathbf{x} \in \Omega \subset \mathbb{R}^2$ be a point in the plane. Consider an interpolation scheme for a vector-valued function $\mathbf{u}(\mathbf{x})$: $\Omega \to \mathbb{R}^2$, in the form:

$$\mathbf{u}^h(\mathbf{x}) = \sum_{I=1}^{n} \phi_I(\mathbf{x})\mathbf{u}_I, \tag{3.6}$$

where $\mathbf{u}_I$ $(I = 1, 2, \ldots, n)$ are the vectors of nodal displacements at the n natural neighbors, and $\phi_I(\mathbf{x})$ are the shape functions associated with each node. In the context of natural neighbor interpolation, the shape functions $\phi_I(\mathbf{x})$ are taken as the n-n coordinates of the point $\mathbf{x}$ in the plane. It is noteworthy to point out here that since the shape functions have compact support (Section 3.3.4), Eq. (3.6) is a

local interpolation scheme. Hereafter, in the context of the natural element method, for the purpose of clarity and in keeping with finite element usage, the expressions "natural neighbor shape function" or simply "shape function" are used synonymously for natural neighbor coordinates.

3.3 Properties

In this section, the properties of natural neighbor shape functions as well as the NEM interpolant (trial function) are presented. A succinct and elegant discussion on the properties of Sibson's interpolant can be found in Farin (1990b).

3.3.1 Interpolation

By definition of the shape function given in Eq. (3.3), the following property is self-evident:

$$0 \leq \phi_I(\mathbf{x}) \leq 1. \tag{3.7}$$

Now, referring to Fig. 3.2b, we note that if $\mathbf{x}$ were to coincide with any node, say node 3 for instance, then it is readily seen that $\phi_3(\mathbf{x}) = 1$ and $\phi_I(\mathbf{x}) = 0$, $I \neq 3$. Therefore, the NEM and FE shape functions share the following property:

$$\phi_I(\mathbf{x}_J) = \delta_{IJ} \tag{3.8}$$

which implies that the NEM interpolant passes through the nodal values. A consequence of this in a Galerkin implementation is that the nodal unknowns $\mathbf{u}_I$ are the

nodal displacements, which is in contrast to most meshless approximations, where $\mathbf{u}^h(\mathbf{x}_I) \neq \mathbf{u}_I$, i.e., the nodal parameters $\mathbf{u}_I$ are not the nodal displacements.

3.3.2 Partition of Unity

By construction (see Eq. (3.3)), we have the following relation:

$$\sum_{I=1}^{n} \phi_I(\mathbf{x}) = 1 \quad \text{in } \Omega, \tag{3.9}$$

where n is the number of natural neighbors for the point $\mathbf{x}$. Hence, by virtue of Eq. (3.7) and the above property, we note that the shape functions form a partition of unity (Melenk and Babuška, 1996). The implication is that this interpolant can exactly reproduce constant functions; in addition, the approximation space can also be enriched by additional functions. In Section 4.2.1, this is discussed at greater length in the context of enriching the NEM interpolant for crack problems.

3.3.3 Linear Completeness

For a second-order PDE such as elastostatics, linear consistency or completeness (Hughes, 1987) is the ability of the interpolant to exactly reproduce constant and linear displacement fields. Sibson (1980) has shown (see also Piper (1993)) that the natural neighbor shape functions satisfy the local coordinate property, namely

$$\mathbf{x} = \sum_{I=1}^{n} \phi_I(\mathbf{x})\mathbf{x}_I, \tag{3.10}$$

which indicates that the shape functions can exactly reproduce the geometrical coordinates. We now show that Eqs. (3.9) and (3.10) together imply that linear completeness is satisfied.

Proof. Consider a linear displacement field in the form:

$$\mathbf{u}(\mathbf{x}) = \boldsymbol{\alpha} + \boldsymbol{\beta}^T \mathbf{x}, \tag{3.11}$$

where $\boldsymbol{\alpha}$ and $\boldsymbol{\beta}$ are constant vectors. The exact nodal displacements are given by

$$\mathbf{u}_I = \boldsymbol{\alpha} + \boldsymbol{\beta}^T \mathbf{x}_I, \tag{3.12}$$

where I is the index for any particular node. Consider the NEM trial function, namely

$$\mathbf{u}^h(\mathbf{x}) = \sum_{I=1}^{n} \phi_I(\mathbf{x}) \mathbf{u}_I, \tag{3.13}$$

where $\mathbf{u}_I$ is the vector of nodal displacements for node I. On using Eq. (3.12) in the above equation, we obtain

$$\mathbf{u}^h(\mathbf{x}) = \boldsymbol{\alpha} \sum_{I=1}^{n} \phi_I(\mathbf{x}) + \boldsymbol{\beta}^T \sum_{I=1}^{n} \phi_I(\mathbf{x}) \mathbf{x}_I, \tag{3.14}$$

which on using Eqs. (3.9) and (3.10) reduces to

$$\mathbf{u}^h(\mathbf{x}) = \boldsymbol{\alpha} + \boldsymbol{\beta}^T \mathbf{x} = \mathbf{u}(\mathbf{x}), \tag{3.15}$$

which completes the proof. □

3.3.4 Supports and Natural Neighbors

Consider node $I \in N$, where N is the set consisting of n natural neighbors for a point $\mathbf{x} \in \Omega \subset \mathbb{R}^2$. The support or domain of influence of the shape function $\phi_I(\mathbf{x})$ associated with node I is defined as the closed sub-domain Ω_{sI} such that $\phi_I(\mathbf{x}) > 0$ in Ω_{sI}, $\phi_I(\mathbf{x}) = 0$ on $\partial\Omega_{sI}$, and $\phi_I(\mathbf{x}) = 0$ in $\mathrm{CH}(N) - \Omega_{sI}$. By the circumcircle criterion, it is evident that for $\phi_I(\mathbf{x})$ to have a non-zero contribution at $\mathbf{x}$, the point $\mathbf{x}$ must lie within the circumcircle of a Delaunay triangle that has node I as one of its vertices. It immediately follows from the above argument that the support of the shape function $\phi_I(\mathbf{x})$ is the intersection of the convex hull $\mathrm{CH}(N)$ with the union of all Delaunay circumcircles that pass through node I (Farin, 1990b). In Fig. 3.3a, a unit square is discretized by 25 (5×5) equi-spaced nodes. The support for node A is illustrated in Fig. 3.3b—node A is located at the center where $\phi_A(\mathbf{x}_A)$ takes on the value of unity. The support is clearly seen to be the union of Delaunay circumcircles about node A. The surface of the shape function $\phi_A(\mathbf{x})$ is analogous to a taut rubber sheet that is stretched so as to meet the nodal data (Watson, 1992).

By comparing the supports of the interpolating functions in NEM to those in some of the widely-used surface approximation schemes, a lot is revealed about the nature of NEM interpolation and its inherent merits. Consider Shepard's interpolant (Shepard, 1968) or moving least squares approximations (Lancaster and Salkauskas, 1981), which are both based on distance-based weights. The weight function is usually isotropic (circular in 2D and spherical in 3D), non-negative within a circle or ball of some fixed radius, and monotonically decreasing with distance from the point $\mathbf{x}$. The rationale in these approaches is that nodes that are closer to $\mathbf{x}$ are given a larger weight at $\mathbf{x}$ than those that are at farther distances.

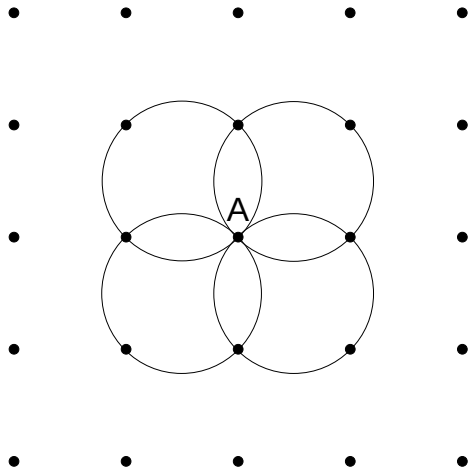

(a)

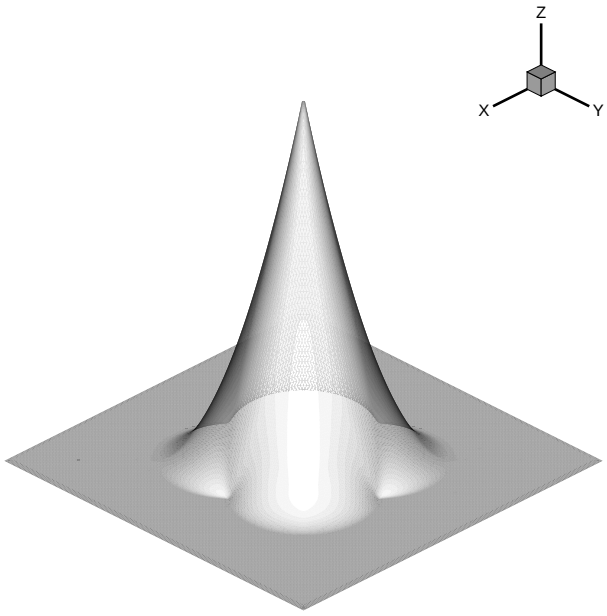

(b)

Figure 3.3: Support for NEM shape function. (a) Nodal grid, and (b) Shape function $\phi_A(\mathbf{x})$ for node A.

Natural neighbor interpolation assumes a totally different viewpoint. The weight at a point $\mathbf{x}$ is not dictated by the same length measure in all dimensions, but by the appropriate Lebesgue measure of the space-dimension. This allows for anisotropic supports, where the support size in direction $\mathbf{r}$ is not given by a L_2-metric but is ascertained based on a geometric construct that defines the region-of-interaction between the nodes. In meshless methods, most of which are based on distance-based weights, the handling of irregular arrangement of nodes is non-trivial since contributions at a point $\mathbf{x}$ tend to be disproportionately biased towards areas of higher nodal density. In n-n interpolation, by virtue of construction, the distribution and density of nodes are taken into account in assigning weights to the nodes at a point $\mathbf{x}$. The above geometric relationship between objects (nodes) is referred to as spatial adjacency (Ahuja, 1982; Gold, 1989). Ahuja (1982) delineates the merits of using Voronoi neighborhoods in the analysis of dot patterns in pattern recognition, while Gold (1989) discusses this property in the context of surface interpolation. An instructive illustration that illuminates the above concept is shown in Fig. 3.4. The number of natural neighbors n is a function of position $\mathbf{x}$ as well as the nodal density. In d-dimensions, the number of natural neighbors is at least $d+1$, with an attainable lower bound (Sibson, 1981). In Fig. 3.5, the variation of n within the convex hull of a uniform grid (5×5) is shown. Clearly, for a regular grid, due to degeneracy, any point has at least four (minimum) natural neighbors. Moreover, there are only two possible values for n, namely, $n = 4$ or 6, with $n = 6$ attained in the lens-shaped regions shown in Fig. 3.5. In Fig. 3.6a, an irregular arrangement of nodes is shown, and the associated variation in n is presented as a contour plot in Fig. 3.6b. In this case, one can see the dependence on nodal arrangement and nodal density.

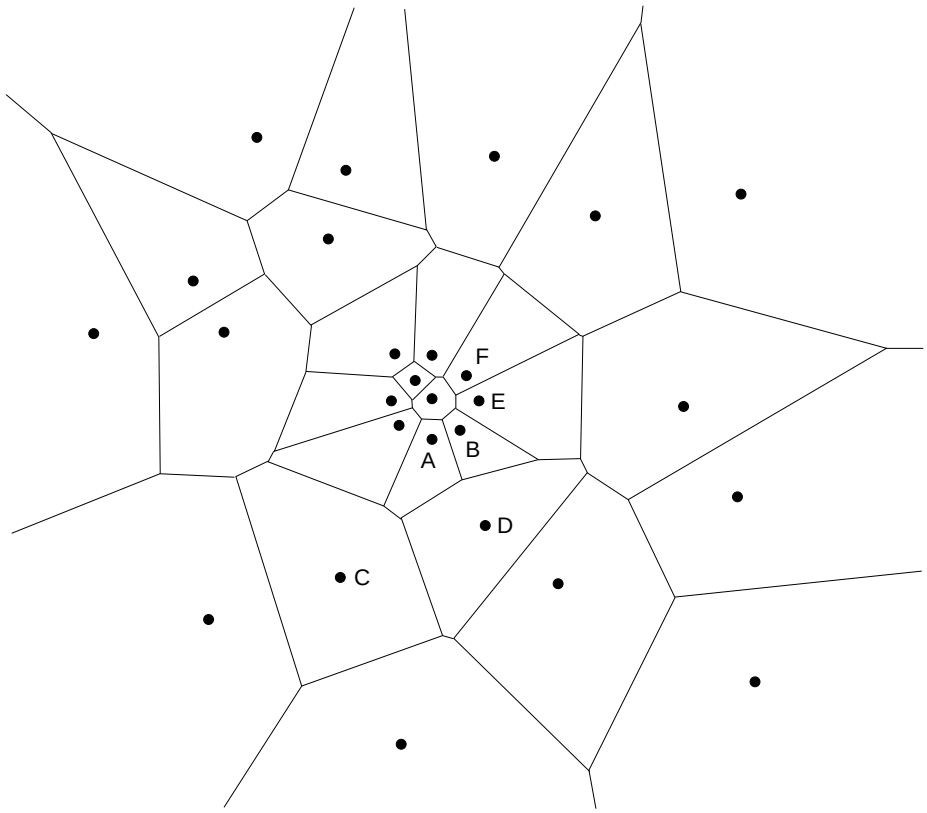

Figure 3.4: Voronoi neighbors. B, C, and D are neighbors of A, but E and F are not, even though $d(A,E) < d(A,D) < d(A,C)$ and $d(A,F) < d(A,D) < d(A,C)$.

3.3.5 Smoothness

The smoothness (or regularity) of the NEM shape functions is discussed. Natural neighbor shape functions are C^∞ everywhere, except at the nodes where they are C^0 (Sibson, 1980; Farin, 1990b; Brown, 1994). Referring to Fig. 3.2, and based on earlier observations and inferences, we see that $\phi_I(\mathbf{x})$ is a continuous function of $\mathbf{x}$. The only points of note are the nodes, but since $\phi_I(\mathbf{x}_I) = 1$ as $\mathbf{x} \to \mathbf{x}_I$ from any direction, the continuity of $\phi_I(\mathbf{x})$ is established. The differentiability of the shape function $\phi_I(\mathbf{x})$ at all points, but for the nodes, is also evident. Since $\phi_I(\mathbf{x})$ has compact support and is

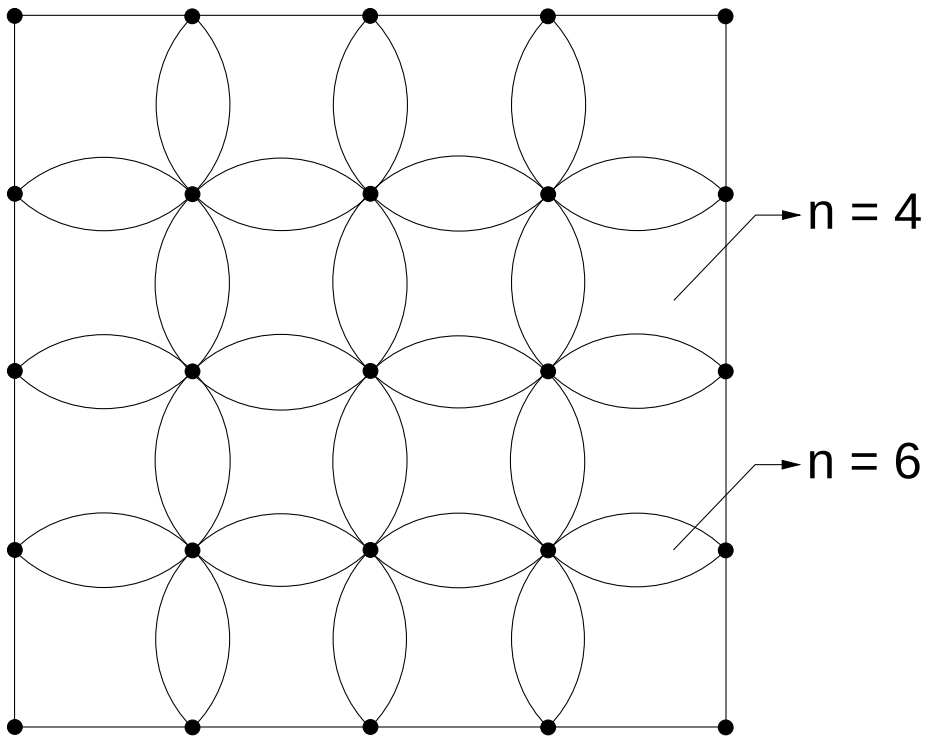

Figure 3.5: Variation of natural neighbors for a regular grid.

smoothly varying at all points except when approaching the nodes, its derivatives are C^∞ in $\Omega\backslash\mathbf{x}_I$. This fact is also seen if one considers the computational procedure for the evaluation of NEM shape functions (Section 3.4). Consider a point $\mathbf{x}$ ($\mathbf{x} \neq \mathbf{x}_J$) which lies on a natural neighbor circumcircle of node I such that $\mathbf{x} \in \partial\Omega_{sI}$. Then, only one circum-triangle contributes to the area calculations in Eq. (3.43). Since $c_j(\mathbf{x}) = \mathbf{v}$ for $j = 1$–3, the area of the sub-triangles and all its derivatives are identically zero. Hence the shape function $\phi_I(\mathbf{x})$ and all its derivatives (first-order and higher) are identically equal to zero at $\mathbf{x}$, and consequently $\phi_I(\mathbf{x}) \in C^\infty$ in $\Omega\backslash\mathbf{x}_I$. On the basis of the locus of the point $\mathbf{x}$ as it traces out a straight line, Farin (1990b) showed that $\phi_I(\mathbf{x})$ is only C^0 at the nodes. This fact is also seen when one considers the support

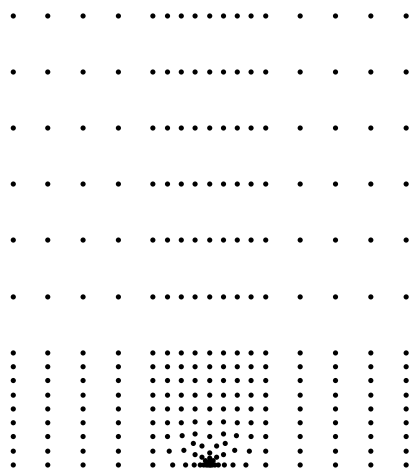

(a)

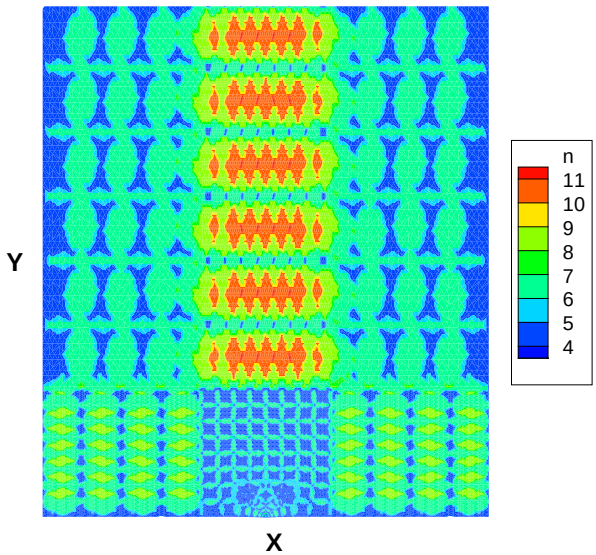

(b)

Figure 3.6: Variation of natural neighbors for an irregular grid. (a) Nodal grid, and (b) Contour plot of natural neighbors.

of the shape functions (Fig. 3.3). The boundary $\partial\Omega_{sI}$ is C^0 with slope discontinuities at the nodes only, which contributes to the jumps in the first derivatives of $\phi_I(\mathbf{x})$ at the nodal locations.

Smooth $\left(C^1(\Omega)\right)$ forms of natural neighbor interpolation have been proposed by many authors (Sibson, 1981; Farin, 1990b; Traversoni, 1993). Sibson (1981) used a weighted least squares fit to modify the original n-n interpolation scheme (Sibson, 1980) to obtain a $C^1(\Omega)$ interpolant everywhere. In one-dimension, it reduces to a Hermite cubic polynomial. Farin (1990b) proposed a $C^1(\Omega)$ natural neighbor interpolant by embedding Sibson's natural neighbor coordinates in the surface representation of a Bernstein-Bézier cubic simplex; in addition, Farin (1990b) recognized Sibson's interpolant to be a building block for higher order surface schemes, and used Hardy's multiquadric (Hardy, 1971) interpolation scheme as a particular example for such an application. Traversoni and Palacios (1991) reformulated Sibson's interpolant in terms of Bernstein polynomials, and using the notion of covering spheres (Traversoni and Palacios, 1991), showed how it can be incorporated into spline theory. These modified forms of Sibson's interpolants which possess $C^1(\Omega)$ continuity are suitable candidates for application in Kirchhoff plate bending theory (see Chapter 5).

3.3.6 Interpolation in One-Dimension

In one-dimension, natural neighbor interpolation as described earlier, is identical to linear finite elements. This fact is proven below.

Proof. Consider a 1D bar of length L which is discretized by M unequally spaced nodes (Fig. 3.7a). It is evident that the Voronoi vertices lie at the mid-point between any two adjacent nodes. In Fig. 3.7a, the dark circles represent the nodes, while the

open circles are the Voronoi vertices. A consequence of the above observation is that all points in the open set $(0, L)$ have two natural neighbors, while the points on the boundary have only one natural neighbor. In order to compute the shape functions, we consider the domain (element in FEM) Ω_I between any two adjacent nodes, say n_I and n_{I+1}. Let us use a reference coordinate $\xi = (x - x_I)/(x_{I+1} - x_I)$, where $\xi \in [0, 1]$, and a local node numbering system: $n_I \to 1$ and $n_{I+1} \to 2$ (Fig. 3.7b). Consider a point $\xi \in \Omega_I$. The second-order Voronoi cells about ξ are shown in Fig. 3.7b. Using Eq. (3.3), the shape functions can be written as

$$\phi_I(\xi) = \frac{L_{\xi I}}{L_{\xi 1} + L_{\xi 2}} \quad (I = 1,\, 2), \tag{3.16}$$

where $L_{\xi 1} = (1 - \xi)/2$ and $L_{\xi 2} = \xi/2$. On using these in the above equation, we obtain the result:

$$\phi_1(\xi) = 1 - \xi, \quad \phi_2(\xi) = \xi, \tag{3.17}$$

which are precisely 1D linear finite element shape functions. □

3.3.7 Interpolation in Two-Dimensions

The equivalence of NEM shape functions to barycentric coordinates and bilinear interpolation, for the special cases of $n = 3$ and $n = 4$ (regular grid), respectively, are shown. For irregular quadrilaterals and $n > 4$, the shape functions are rational quartic functions (Farin, 1990b).

(a)

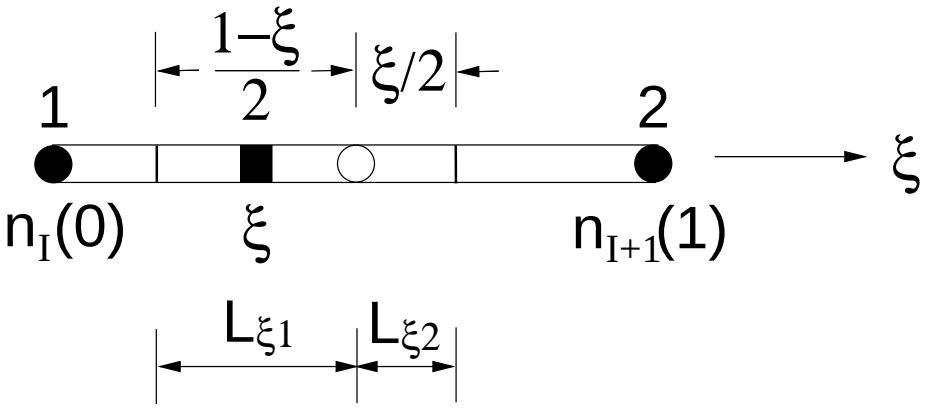

(b)

Figure 3.7: NEM shape functions in one-dimension. (a) Physical space, and (b) Reference space.

Three Natural Neighbors If a point $\mathbf{x}$ has three natural neighbors ($n = 3$), then the NEM shape functions are precisely the barycentric coordinates, or constant strain triangle finite element shape functions.

Proof. By an argument of uniqueness for barycentric as well as NEM shape functions ($n = 3$), this equivalence is immediately seen (Farin, 1990b). Here we use the linear reproducing conditions to prove the correspondence. Let the natural neighbors of point $\mathbf{x} = (x, y)$ be nodes 1, 2, and 3, with coordinates (x_I, y_I), $I = 1$–3 (Fig. 3.8). Using Eqs. (3.9) and (3.10), the following conditions are met by the NEM shape functions:

$$\sum_{I=1}^{3} \phi_I(\mathbf{x}) = 1, \tag{3.18}$$

$$\sum_{I=1}^{3} \phi_I(\mathbf{x}) x_I = x, \tag{3.19}$$

$$\sum_{I=1}^{3} \phi_I(\mathbf{x}) y_I = y, \tag{3.20}$$

which in matrix form can be written as

$$\begin{bmatrix} 1 & 1 & 1 \\ x_1 & x_2 & x_3 \\ y_1 & y_2 & y_3 \end{bmatrix} \begin{Bmatrix} \phi_1(\mathbf{x}) \\ \phi_2(\mathbf{x}) \\ \phi_3(\mathbf{x}) \end{Bmatrix} = \begin{Bmatrix} 1 \\ x \\ y \end{Bmatrix}. \tag{3.21}$$

The solution of the above system of linear equations is:

$$\phi_1(\mathbf{x}) = \frac{D_1(\mathbf{x})}{D(\mathbf{x})}, \quad \phi_2(\mathbf{x}) = \frac{D_2(\mathbf{x})}{D(\mathbf{x})}, \quad \phi_3(\mathbf{x}) = \frac{D_3(\mathbf{x})}{D(\mathbf{x})}, \tag{3.22}$$

where

$$D(\mathbf{x}) = \begin{vmatrix} 1 & 1 & 1 \\ x_1 & x_2 & x_3 \\ y_1 & y_2 & y_3 \end{vmatrix} = \begin{vmatrix} 1 & 0 & 0 \\ x_1 & x_2 - x_1 & x_3 - x_1 \\ y_1 & y_2 - y_1 & y_3 - y_1 \end{vmatrix} = 2A(\mathbf{x}), \tag{3.23}$$

and $D_1(\mathbf{x}) = 2A_1(\mathbf{x})$, $D_2(\mathbf{x}) = 2A_2(\mathbf{x})$, and $D_3(\mathbf{x}) = 2A_3(\mathbf{x})$ (Fig. 3.8). In Eq. (3.23), $A(\mathbf{x})$ is the area of $\triangle_{123}$. Hence we can write the shape functions as

$$\phi_1(\mathbf{x}) = \frac{A_1(\mathbf{x})}{A(\mathbf{x})}, \quad \phi_2(\mathbf{x}) = \frac{A_2(\mathbf{x})}{A(\mathbf{x})}, \quad \phi_3(\mathbf{x}) = \frac{A_3(\mathbf{x})}{A(\mathbf{x})}, \tag{3.24}$$

which are precisely the barycentric coordinates for the point $\mathbf{x}$. □

Four Natural Neighbors (Regular Grid) For a regular rectangular nodal grid, if a point $\mathbf{x}$ has four natural neighbors ($n = 4$), then bilinear interpolation on the rectangle is obtained. A geometric proof is provided by Farin (1990b). Here we use the definition of natural neighbor shape functions and explicitly carry out the computations to show the equivalence. It is to be noted that the above claim does not hold for the general case of four natural neighbors that are located at the vertices of a quadrilateral.

Proof. Consider a point $\mathbf{x}$ with four natural neighbors located at the vertices of a unit square: $(x_1, y_1) = (0,0)$, $(x_2, y_2) = (1,0)$, $(x_3, y_3) = (1,1)$, and $(x_4, y_4) = (0,1)$ (Fig. 3.9). The first-order (dark line) and second-order Voronoi cells about $\mathbf{x}$ are shown in Fig. 3.9. By definition of the NEM shape functions, we can write

$$\phi_I(\mathbf{x}) = \frac{A_I(\mathbf{x})}{A(\mathbf{x})} \quad (I = 1\text{–}4), \tag{3.25}$$

where $A_1(\mathbf{x})$, $A_2(\mathbf{x})$, $A_3(\mathbf{x})$, and $A_4(\mathbf{x})$ are the areas of $\triangle_{eda}$, $\triangle_{eab}$, $\triangle_{ebc}$, and $\triangle_{ecd}$, respectively. In the above equation, $A(\mathbf{x})$ is the area of the first-order Voronoi polygon $abcd$ and e is the center of the unit square with coordinates $(1/2, 1/2)$.

We proceed by computing the area of the second-order Voronoi cells. To this end, by recalling the construction of $2nd$-order Voronoi cells, it is clearly seen that vertex a is the center of the circle that circumscribes the triangle $\triangle_{12\mathbf{x}}$, and proceeding likewise, b is the circumcenter of triangle $\triangle_{23\mathbf{x}}$, c that of $\triangle_{34\mathbf{x}}$, and d that of $\triangle_{41\mathbf{x}}$—see Section 3.4 also. Using Eq. (3.37), these coordinates are computed to be

$$a_1 = \frac{1}{2}, \qquad a_2 = \frac{-x + x^2 + y^2}{2y}, \tag{3.26a}$$

$$b_1 = \frac{1 + y - x^2 - y^2}{2(1-x)}, \qquad b_2 = \frac{1}{2}, \tag{3.26b}$$

$$c_1 = \frac{1}{2}, \qquad c_2 = \frac{1 + x - x^2 - y^2}{2(1-y)}, \tag{3.26c}$$

$$d_1 = \frac{-y + x^2 + y^2}{2x}, \qquad d_2 = \frac{1}{2}. \tag{3.26d}$$

Using the formula for the area of a triangle given in Eq. (3.35), we obtain

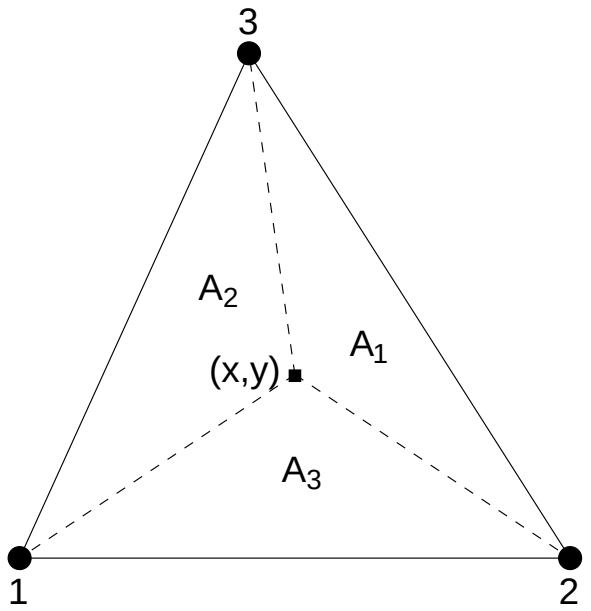

Figure 3.8: Barycentric coordinates ($n = 3$).

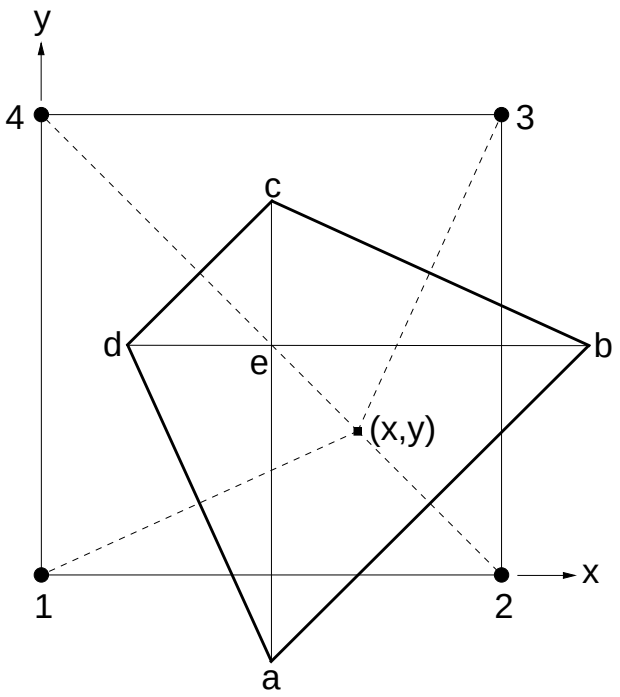

Figure 3.9: Bilinear interpolation on a regular grid ($n = 4$).

$$A_1(\mathbf{x}) = \frac{(x^2+y^2-x-y)^2}{8xy}, \tag{3.27a}$$

$$A_2(\mathbf{x}) = \frac{(x^2+y^2-x-y)^2}{8y(1-x)}, \tag{3.27b}$$

$$A_3(\mathbf{x}) = \frac{(x^2+y^2-x-y)^2}{8(1-x)(1-y)}, \tag{3.27c}$$

$$A_4(\mathbf{x}) = \frac{(x^2+y^2-x-y)^2}{8x(1-y)}. \tag{3.27d}$$

Since $A(\mathbf{x}) = \sum_{I=1}^{4} A_I(\mathbf{x})$, we have

$$A(\mathbf{x}) = \frac{(x^2+y^2-x-y)^2}{8xy(1-x)(1-y)}, \tag{3.28}$$

and hence on using Eqs. (3.27) and (3.28) in Eq. (3.25), the NEM shape functions can be written as

$$\phi_1(\mathbf{x}) = (1-x)(1-y), \tag{3.29a}$$

$$\phi_2(\mathbf{x}) = x(1-y), \tag{3.29b}$$

$$\phi_3(\mathbf{x}) = xy, \tag{3.29c}$$

$$\phi_4(\mathbf{x}) = y(1-x), \tag{3.29d}$$

which are precisely bilinear FE shape functions. The above derivation is easily generalized to the rectangle (linear transformation of a square), and hence bilinear interpolation on the rectangle is realized by the NEM interpolant. □

3.3.8 Interpolation in Multi-Dimensions

On the basis of earlier discussions and results, it is observed that natural neighbor interpolation in higher-dimensions is a particular generalization of univariate interpolation in one-dimension (Farin, 1990b). This appears to be a natural means of extending an interpolation scheme since the interpolant is constructed on the basis of an appropriate Lebesgue measure (volume of polytopes) in the space-dimension of interest. This is in stark contrast to finite element interpolation in higher dimensions which is constructed on the basis of the product of 1D Lagrange interpolation rules. From a mathematical and geometric viewpoint, the natural-neighbor approach is appealing in more ways than one: a sound mathematical- and geometrical-basis for construction, neighbor-relationships that reflect the spatial adjacency between nodes, and a computationally feasible and attractive choice. In the remainder of this thesis, we show by examples, how these properties of n-n interpolation are also of merit as a paradigm for the numerical solution of PDEs.

3.3.9 Linear Precision on the Boundary $\partial\Omega$

Issues pertaining to the imposition of essential boundary conditions in NEM for convex and non-convex bodies are addressed here. For a convex domain Ω, the discrete representation of $\partial\Omega$ is the boundary of the convex hull CH(N) for a set of distinct nodes N, while for a non-convex domain, the discrete representation of the continuous boundary $\partial\Omega$ is through a Planar Straight Line Graph (PSLG)[2].

[2] A PSLG is a collection of nodes and edges, whose presence is preserved in the partitioning of the domain

Convex Domains The discrete model consists of a set of nodes N that describes a convex domain Ω, with $\partial\Omega$ represented by the boundary of the convex hull $\mathrm{CH}(N)$. On the boundary of the convex hull, the trial functions $\mathbf{u}^h(\mathbf{x})$ are strictly linear between two nodes that belong to an edge of a Delaunay triangle. The proof follows:

Proof. Consider a typical Delaunay triangle which has one edge (two nodes) along the boundary of the convex hull, and the trial functions $\mathbf{u}^h(\xi)$ are to be evaluated at a point ξ along the edge 1–2 (Fig. 3.10a). For simplicity and for ease of illustration, we assume that ξ has only three natural neighbors, namely nodes 1, 2, and 3. We use a local coordinate system ξ along the edge 1–2 such that $\xi = 0$ at node 1 and $\xi = 1$ at node 2. The $1st$-order and $2nd$-order Voronoi cells about ξ are shown in Fig. 3.10b. By definition, the shape functions can be written as

$$\phi_I(\xi) = \frac{A_I(\xi)}{A(\xi)} \quad (I = 1,\, 2,\, 3), \tag{3.30}$$

where $A(\xi) = \sum_{J=1}^{3} A_J(\xi)$. Since the Voronoi cell for each node on the boundary of the convex hull is unbounded, we can express A_1, A_2, and A_3 as

$$A_1(\xi) = \lim_{L\to\infty} L\xi_1 + \delta_1, \quad A_2(\xi) = \lim_{L\to\infty} L\xi_2 + \delta_2, \quad A_3(\xi) = \delta_3, \tag{3.31}$$

where $\xi_1 = (1-\xi)/2$, $\xi_2 = \xi/2$ and δ_1, δ_2, and δ_3 are finite. For instance, δ_3 is given by the area of $\triangle_{abc}$ in Fig. 3.10b. On using Eq. (3.30), we can write

$$\phi_1(\xi) = \lim_{L\to\infty} \frac{L(1-\xi)+2\delta_1}{L+2\delta_1+2\delta_2+2\delta_3}, \tag{3.32a}$$

$$\phi_2(\xi) = \lim_{L\to\infty} \frac{L\xi+2\delta_2}{L+2\delta_1+2\delta_2+2\delta_3}, \tag{3.32b}$$

$$\phi_3(\xi) = \lim_{L\to\infty} \frac{2\delta_3}{L+2\delta_1+2\delta_2}. \tag{3.32c}$$

Taking the limit as $L \to \infty$ in the above equations, we obtain

$$\phi_1(\xi) = 1-\xi, \quad \phi_2(\xi) = \xi, \quad \phi_3(\xi) = 0, \tag{3.33}$$

and hence along the edge 1–2, the shape function contributions from only nodes 1 and 2 are non-zero. The above result is in general true, even if more than three natural neighbors are considered. This is so, since the $2nd$-order Voronoi cell about ξ for all interior nodes are closed polygons and hence the overlapping areas are finite, similar to $A_3(\xi)$ in Fig. 3.10b. Using the above equation, the trial functions at the point ξ can be written as

$$\mathbf{u}^h(\xi) = (1-\xi)\mathbf{u}_1 + \xi\mathbf{u}_2 \tag{3.34}$$

which are linear functions, and hence the proof. □

Non-Convex Domains Consider a set of nodes N that describes a non-convex domain Ω. Consider a Γ_1 ($\Gamma_1 \subset \Gamma = \partial\Omega$) which renders the domain to be non-

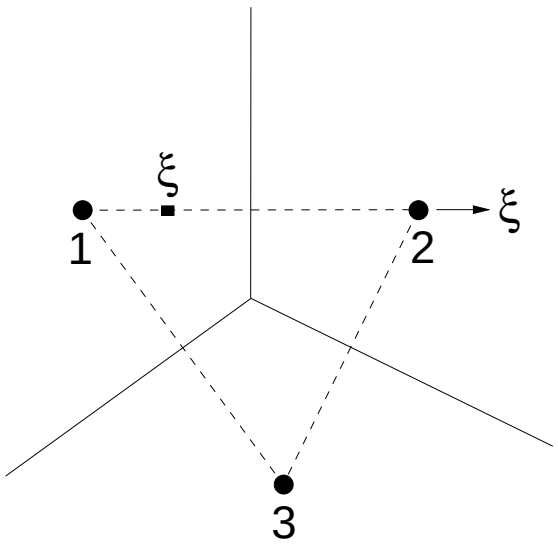

(a)

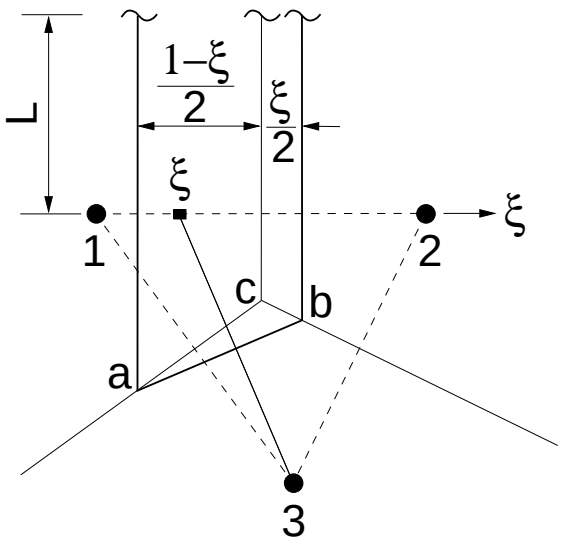

(b)

Figure 3.10: Linear behavior of $\mathbf{u}^h(\xi)$ along the boundary of a convex domain. (a) Original Voronoi cells ($n = 3$) and ξ, and (b) $1st$-order and $2nd$-order Voronoi cells about ξ.

convex. For purpose of illustration, we choose a non-convex domain bounded by two concentric circles. The discrete model (one-quarter) along with the Voronoi diagram is shown in Fig. 3.11. It is evident that the Voronoi cells for the nodes along Γ_i ($i = 2$–4) are unbounded, while the Voronoi cells for the nodes along Γ_1 are bounded and therefore have finite areas (Fig. 3.11b). The proof outlined for the case of convex domains holds for $\tilde{\Gamma} = \Gamma_2 \cup \Gamma_3 \cup \Gamma_4$ but fails for Γ_1. Therefore, the approximation is not strictly linear between adjacent nodes on the boundary Γ_1. For a point $\mathbf{x}$ located on Γ_1, there exists non-zero contributions from some interior nodes. However, numerical simulations indicate that with adequate discretization of the boundary Γ_1, the shape function contribution of interior nodes are two orders or less in magnitude in comparison to the boundary node values. Consider the nodal grid shown in Fig. 3.11 which consists of 49 nodes with seven nodes along Γ_1. For a point located on Γ_1, the shape function contributions of interior nodes are about 2% of those due to the boundary nodes on Γ_1. Further discretization of the boundary Γ_1 would lead to better accuracy in the imposition of the essential boundary conditions. In general, for non-convex domains, the approximation to linearity of the trial function along Γ_1 depends on the nodal discretization as well as the local radius of curvature of Γ_1.

A consequence of the above discussion is that essential boundary conditions in the NEM can be directly imposed on the nodes, in accordance with the finite element method—this is due to the interpolating property of the NEM shape functions and the linearity of the trial functions along the edge of a boundary Delaunay triangle. It is to be noted that the above inference is rigorously true for convex domains; however, for non-convex domains, numerical simulations need to be carried out on a per problem basis to determine the appropriate nodal discretization of Γ_1 which is

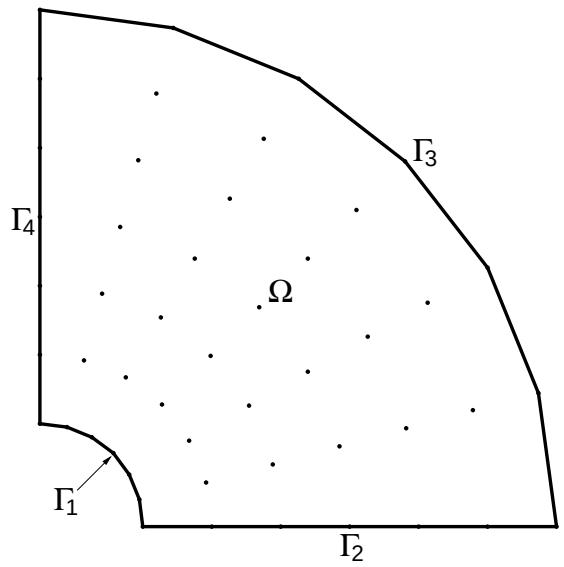

(a)

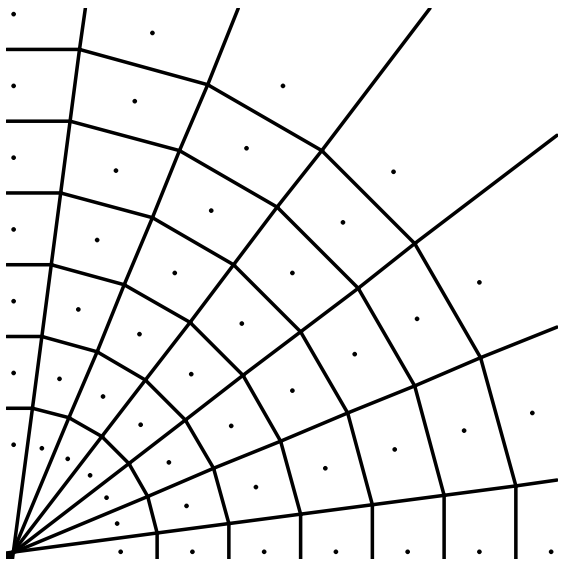

(b)

Figure 3.11: Linear behavior of $\mathbf{u}^h(\mathbf{x})$ along the boundary of a non-convex domain. (a) Nodal discretization, and (b) Voronoi diagram.

required to yield accurate results.

3.4 Numerical Computational Procedure for NEM Shape Functions

In this work, Watson's algorithm (Watson, 1994) is used to compute the natural neighbor shape functions. The algorithmic details and computational procedure is described in Watson (1994) as well as Braun, Sambridge, and McQueen (1995). First, we provide well-known geometric formulas for the area, circumcenter, and circumradius of a triangle, and then go on to present the computational implementation of the shape function algorithm.

3.4.1 Area of a Triangle

Consider a triangle $t(A, B, C)$ with vertices $A(\mathbf{a})$, $B(\mathbf{b})$, and $C(\mathbf{c})$, where $\mathbf{a} = (a_1, a_2)$, $\mathbf{b} = (b_1, b_2)$, and $\mathbf{c} = (c_1, c_2)$. The signed area of $\triangle_{ABC}$ is given by

$$A = \frac{(a_1 - c_1)(b_2 - c_2) - (b_1 - c_1)(a_2 - c_2)}{2}. \tag{3.35}$$

If $\mathbf{a} \equiv \mathbf{a}(\mathbf{x}) = \big(a_1(\mathbf{x}), a_2(\mathbf{x})\big)$, $\mathbf{b} \equiv \mathbf{b}(\mathbf{x}) = \big(b_1(\mathbf{x}), b_2(\mathbf{x})\big)$, and c_1 and c_2 are independent of $\mathbf{x}$, then the derivatives of A can be written as

$$\begin{aligned} A_{,i}(\mathbf{x}) = & \frac{\big(a_1(\mathbf{x}) - c_1\big)b_{2,i}(\mathbf{x}) + \big(b_2(\mathbf{x}) - c_2\big)a_{1,i}(\mathbf{x})}{2} \\ & - \frac{\big(b_1(\mathbf{x}) - c_1\big)a_{2,i}(\mathbf{x}) + \big(a_2(\mathbf{x}) - c_2\big)b_{1,i}(\mathbf{x})}{2}, \end{aligned} \tag{3.36}$$

where $i = 1, 2$, and a comma denotes differentiation with respect to the appropriate spatial coordinate.

3.4.2 Circumcenter and Circumradius of a Triangle

Consider a triangle $t(A, B, C)$ with vertices $A(\mathbf{a})$, $B(\mathbf{b})$, and $C(\mathbf{c})$, where $\mathbf{a} = (a_1, a_2)$, $\mathbf{b} = (b_1, b_2)$, and $\mathbf{c} = (c_1, c_2)$ (Fig. 3.12). The circumcircle of $\triangle_{ABC}$ is the circle that passes through the three vertices of the triangle. Its center is the circumcenter $v(v_1, v_2)$ and radius R is the circumradius. The coordinates of the circumcenter are the perpendicular bisectors of the edges of the triangle. The coordinates of the circumcenter are found by either: (a) considering the equation of a plane through three points in an augmented space $\mathbb{R}^3$, where each point $(x_i, y_i, x_i^2 + y_i^2)$ is the map of $\mathbf{x}$ onto $(\mathbf{x}, ||\mathbf{x}||^2)$, or (b) solving for the intersection point of the perpendicular bisector of any two edges of the triangle. We use the latter approach to obtain the coordinates of the circumcenter. By considering the edges AC and BC in Fig. 3.12, a system of two linear equations is obtained. On carrying out the solution and after some algebraic manipulations, we obtain the following expressions for the circumcenter of $\triangle_{ABC}$:

$$v_1 = \frac{(a_1^2 - c_1^2 + a_2^2 - c_2^2)(b_2 - c_2) - (b_1^2 - c_1^2 + b_2^2 - c_2^2)(a_2 - c_2)}{D}, \tag{3.37a}$$

$$v_2 = \frac{(b_1^2 - c_1^2 + b_2^2 - c_2^2)(a_1 - c_1) - (a_1^2 - c_1^2 + a_2^2 - c_2^2)(b_1 - c_1)}{D}, \tag{3.37b}$$

where D which is four times the area of $\triangle_{ABC}$ $\big($refer to Eq. (3.35)$\big)$, is given by

$$D = 2\big[(a_1 - c_1)(b_2 - c_2) - (b_1 - c_1)(a_2 - c_2)\big]. \tag{3.37c}$$

From the viewpoint of computational efficiency (reduced multiplication operations), the squared difference of two terms in the above equations is represented as the product of their sums and differences in the numerical implementation. For instance, $a_1^2 - c_1^2$ in Eq. (3.37a) is computed as $(a_1 - c_1)(a_1 + c_1)$, etc.

If the vertex $C(\mathbf{c})$ coincides with the point $\mathbf{x}$, where $\mathbf{x} = (x_1, x_2)$, then $c_1 = x_1$ and $c_2 = x_2$. Assume the coordinates a_1, a_2, b_1, and b_2 are independent of x_1 and x_2. The derivatives of the coordinates of the circumcenter can then be written in the following simplified form:

$$v_{1,1}(\mathbf{x}) = \frac{\big(x_1 - v_1(\mathbf{x})\big)\, D_{,1}(\mathbf{x})}{D(\mathbf{x})}, \tag{3.38a}$$

$$v_{1,2}(\mathbf{x}) = \frac{\big(\alpha + x_2 D_{,1}(\mathbf{x}) - v_1(\mathbf{x}) D_{,2}(\mathbf{x})\big)}{D(\mathbf{x})}, \tag{3.38b}$$

$$v_{2,1}(\mathbf{x}) = \frac{\big(-\alpha + x_1 D_{,2}(\mathbf{x}) - v_2(\mathbf{x}) D_{,1}(\mathbf{x})\big)}{D(\mathbf{x})}, \tag{3.38c}$$

$$v_{2,2}(\mathbf{x}) = \frac{\big(x_2 - v_2(\mathbf{x})\big)\, D_{,2}(\mathbf{x})}{D(\mathbf{x})}, \tag{3.38d}$$

where $v_1(\mathbf{x})$, $v_2(\mathbf{x})$, and $D(\mathbf{x})$ are given in Eq. (3.37) and

$$\alpha = (b_1 + a_1)(b_1 - a_1) + (b_2 + a_2)(b_2 - a_2), \tag{3.39a}$$

$$D_{,1}(\mathbf{x}) = 2(a_2 - b_2), \tag{3.39b}$$

and

$$D_{,2}(\mathbf{x}) = 2(b_1 - a_1). \tag{3.39c}$$

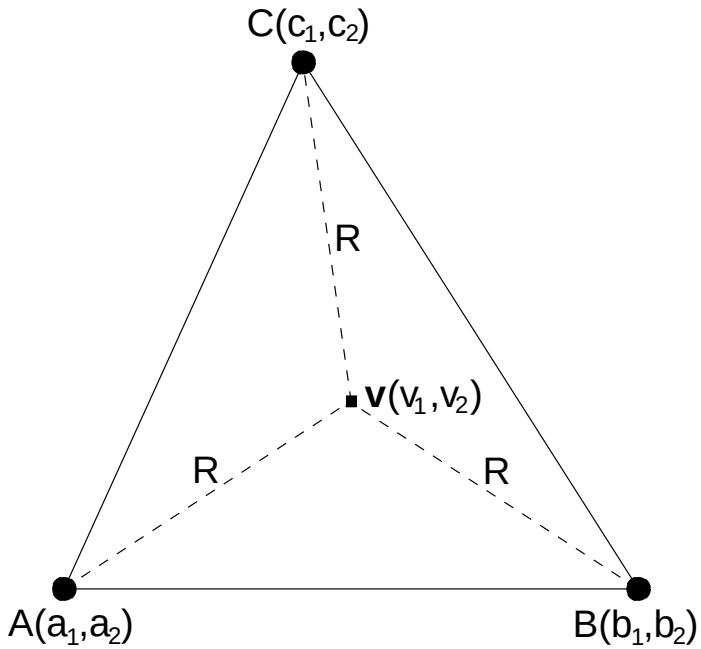

Figure 3.12: Circumcenter and circumradius of a triangle.

By definition, the circumradius is the distance from the circumcenter to a vertex of $\triangle_{ABC}$. Hence the square of the circumradius can be written as

$$R^2(\mathbf{x}) = \big(a_1 - v_1(\mathbf{x})\big)^2 + \big(a_2 - v_2(\mathbf{x})\big)^2. \tag{3.40}$$

3.4.3 Shape Function Computations

The algorithm proposed by Watson (Watson, 1994) is used to compute the shape functions. In order to present the algorithm and its numerical implementation, we consider Fig. 3.2b, where the construction of natural neighbor shape functions is illustrated. In Fig. 3.13, the original nodal set, the Voronoi diagram (dashed lines), and the natural neighbor circumcircles are shown. The point $\mathbf{x}$ is introduced into the

set, and the natural neighbors of $\mathbf{x}$ as well as the values of the natural neighbor shape functions and their derivatives at $\mathbf{x}$ are to be computed.

The computational methodology for the shape function evaluation is based on the fact that the second-order Voronoi cells about $\mathbf{x}$ (Fig. 3.2b) can be computed as a summation of signed area of triangles. In the implementation of the NEM, a preprocessing step is the computation of the circumcenter and square of the circumradius of the natural neighbor (Delaunay) circumcircles. It is assumed that the nodal connectivity for each Delaunay triangle is stored in counter-clockwise orientation, and consequently the appropriate sign is automatically chosen when the area of a triangle is computed. The formulas for the area, circumcenter, and circumradius of a triangle are presented in Sections 3.4.1 and 3.4.2. In the assembly-step, prior to the shape function computation, the number of natural neighbors n and their global nodal numbers along with the number of triangles t_n associated with the natural neighbors as well as their global triangle numbers, are computed. A simple means to determine if a node is a natural neighbor of a point $\mathbf{x}$ is to use the empty circumcircle criterion indicated in Section 3.1—if the square of the Euclidean distance from $\mathbf{x}$ to the center of a natural neighbor circumcircle (associated with nodes n_I, n_J, and n_K) is less than the square of the radius of the circumcircle, then nodes n_I, n_J, and n_K are natural neighbors of the point $\mathbf{x}$:

$$\|\mathbf{v} - \mathbf{x}\|^2 < R^2 \,, \tag{3.41}$$

where $\mathbf{v} = (v_1, v_2)$ is the center of the natural neighbor circumcircle and R, which is given in Eq. (3.40), is its radius. Braun and Sambridge (1995) used Lawson's

algorithm (Lawson, 1977) as part of the neighbor-search, which is a computationally sound choice if interpolation of a very large nodal set is considered. This is so, since otherwise the condition given in Eq. (3.41) needs to be checked for all the Delaunay triangles. In this work, since relatively few nodes ($M < 3000$) are considered in the nodal discretization of a domain, the above condition is checked for all the Delaunay triangles.

Let the 3-tuple $(\mathbf{p}, \mathbf{q}, \mathbf{r})$ represent a triangle with vertices $\mathbf{p} = (p_1, p_2)$, $\mathbf{q} = (q_1, q_2)$, and $\mathbf{r} = (r_1, r_2)$. Now, for each Delaunay triangle t with circumcenter $\mathbf{v} = (v_1, v_2)$ that is selected on the basis of Eq. (3.41), we form a new set of three triangles $\{t_1, t_2, t_3\}$, where each has $\mathbf{x}$ and two of the vertices of the Delaunay triangle t as its vertices. Consider a local numbering system ($i = 1,\ 2,\ 3$) for the vertices $\mathbf{a}_i$ of the new triangles t_i, and associate each local node i with its opposite edge (j–k). We can write the circumcenter of the new triangles so constructed and their derivatives in the following compact form:

$$\mathbf{c}_i(\mathbf{x}) = \Theta(\mathbf{a}_j, \mathbf{a}_k, \mathbf{x}), \tag{3.42a}$$

$$\mathbf{c}_{i,m}(\mathbf{x}) = \Theta_{,m}(\mathbf{a}_j, \mathbf{a}_k, \mathbf{x}), \tag{3.42b}$$

where $m = 1,\ 2$ and i, j, and k assume cyclic counter-clockwise permutations of 123. In the above equations, Θ and $\Theta_{,m}$ are functional representations for the circumcenter of a triangle and its derivatives which are given in Eqs. (3.37) and (3.38), respectively. To elaborate, $\mathbf{c}_1$ refers to the circumcenter of the triangle with vertices $(2, 3, \mathbf{x})$, $\mathbf{c}_2$ that for the triangle with vertices $(3, 1, \mathbf{x})$, and $\mathbf{c}_3$ is the circumcenter of the triangle with vertices $(1, 2, \mathbf{x})$.

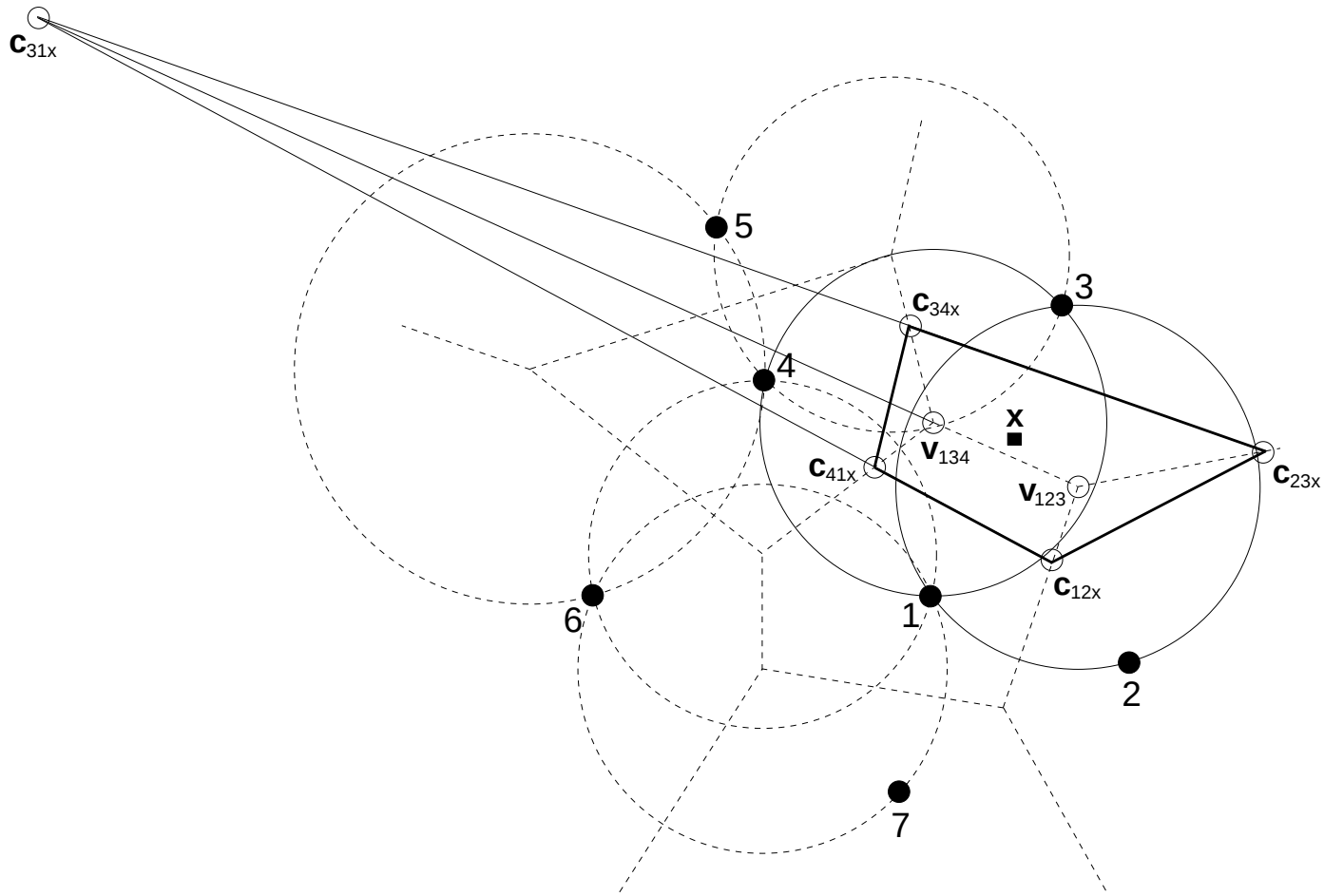

Figure 3.13: Computation of natural neighbor shape functions.

The next step involves the construction of sub-triangles using combinations from the collection $\{\mathbf{c}_1(\mathbf{x}), \mathbf{c}_2(\mathbf{x}), \mathbf{c}_3(\mathbf{x}), \mathbf{v}\}$, such that $\mathbf{v}$ appears in all the sub-triangles. Here too cyclic permutation of 123 is maintained. Clearly, three such sub-triangles can be constructed, namely $\big(\mathbf{c}_1(\mathbf{x}), \mathbf{c}_2(\mathbf{x}), \mathbf{v}\big)$ [node 3], $\big(\mathbf{c}_2(\mathbf{x}), \mathbf{c}_3(\mathbf{x}), \mathbf{v}\big)$ [node 1], and $\big(\mathbf{c}_3(\mathbf{x}), \mathbf{c}_1(\mathbf{x}), \mathbf{v}\big)$ [node 2], where the nodal association is indicated within the square bracket. Now, the area of these sub-triangles and their derivatives can be written as

$$\alpha_{it}(\mathbf{x}) = \Psi\big(\mathbf{c}_j(\mathbf{x}), \mathbf{c}_k(\mathbf{x}), \mathbf{v}\big), \tag{3.43a}$$

$$\alpha_{it,m}(\mathbf{x}) = \Psi_{,m}\big(\mathbf{c}_j(\mathbf{x}), \mathbf{c}_k(\mathbf{x}), \mathbf{v}\big), \tag{3.43b}$$

where $m = 1, 2$ and i, j, and k assume cyclic counter-clockwise permutations of 123. In the above equations, Ψ and $\Psi_{,m}$ are functional representations for the area of a triangle and its derivatives which are given in Eqs. (3.35) and (3.36), respectively. By the local $\rightarrow$ global nodal associativity, the area contribution to each global node and its update is made through the following conceptual symbolic assignments:

$$\beta_I(\mathbf{x}) \leftarrow \beta_I(\mathbf{x}) + \alpha_{it}(\mathbf{x}), \tag{3.44a}$$

$$\beta_{I,m}(\mathbf{x}) \leftarrow \beta_{I,m}(\mathbf{x}) + \alpha_{it,m}(\mathbf{x}), \tag{3.44b}$$

where $\beta_I(\mathbf{x})$ and $\beta_{I,m}(\mathbf{x})$ are set to zero for all natural neighbors prior to the shape function computations. The above procedure is carried out for all the Delaunay circum-triangles t ($t = 1, 2 \ \ldots, t_n$). Hence the area of the second-order Voronoi cell

and its derivatives are now given by

$$A_I(\mathbf{x}) = \beta_I(\mathbf{x}), \tag{3.45a}$$

$$A_{I,m}(\mathbf{x}) = \beta_{I,m}(\mathbf{x}), \tag{3.45b}$$

for $m = 1, 2$ and $I = 1, 2, \ldots, n$. Let

$$A(\mathbf{x}) = \sum_{I=1}^{n} A_I(\mathbf{x}), \tag{3.46a}$$

$$A_{,m}(\mathbf{x}) = \sum_{I=1}^{n} A_{I,m}(\mathbf{x}). \tag{3.46b}$$

We reproduce Eqs. (3.3) and (3.5) below for the natural neighbor shape functions and their derivatives:

$$\phi_I(\mathbf{x}) = \frac{A_I(\mathbf{x})}{A(\mathbf{x})}, \tag{3.47a}$$

$$\phi_{I,m}(\mathbf{x}) = \frac{A_{I,m}(\mathbf{x}) - \phi_I(\mathbf{x})A_{,m}(\mathbf{x})}{A(\mathbf{x})}. \tag{3.47b}$$

Substituting for $A_I(\mathbf{x})$, $A_{I,m}(\mathbf{x})$, $A(\mathbf{x})$, and $A_{,m}(\mathbf{x})$ from Eqs. (3.45a), (3.45b), (3.46a), and (3.46b), respectively, in the above equations, the shape function $\phi_I(\mathbf{x})$ and its derivatives $\phi_{I,m}(\mathbf{x})$ are computed for all the natural neighbors. A pseudo-code for the shape function computations is presented in Table 3.1.

We use Fig. 3.13 to illustrate the application of the shape function computations. In order to keep the notations to a minimum, we let the position vector of the circumcenter of a triangle also serve as a label for the point. It is seen in Fig. 3.13 that the point $\mathbf{x}$ lies within only two circles (dark lines), namely $\mathbf{v}_{123}$ and $\mathbf{v}_{134}$ which

1. Determine natural neighbors I ($I = 1 \rightarrow n$) and Delaunay circum-triangles t ($t = 1 \rightarrow t_n$) for $\mathbf{x}$—see Eq. (3.41);
2. Initialize $\phi_I = d\phi_{I1} = d\phi_{I2} = 0 \ \forall \ I$; $A = dA_1 = dA_2 = 0$;
3. for $t = 1 \rightarrow t_n$ {
   - set $\mathbf{v}$ = circumcenter of $\triangle_t$—see Eq. (3.37);
   - for $i = 1 \rightarrow 3$ {
     - set j and k using cyclic order;
     - compute $\mathbf{c}_i$ and $\mathbf{c}_{i,m}$ based on Eq. (3.42) and store;

     }
   - for $i = 1 \rightarrow 3$ {
     - set g = global node number of local node i;
     - set I = position of g in the natural neighbor nodal array ($1 \leq I \leq n$);
     - compute α_{it} and $\alpha_{it,m}$ based on Eq. (3.43);
     - set $\alpha = \alpha_{it}$, $d\alpha_1 = \alpha_{it,1}$, $d\alpha_2 = \alpha_{it,2}$;
     - update $\phi_I \leftarrow \phi_I + \alpha$, $d\phi_{I1} \leftarrow d\phi_{I1} + d\alpha_1$, $d\phi_{I2} \leftarrow d\phi_{I2} + d\alpha_2$;
     - update $A \leftarrow A + \alpha$, $dA_1 \leftarrow dA_1 + d\alpha_1$, $dA_2 \leftarrow dA_2 + d\alpha_2$;

     }

   }
4. for $I = 1 \rightarrow n$ {
   - set $\phi_I \leftarrow \dfrac{\phi_I}{A}$, $d\phi_{I1} \leftarrow \dfrac{d\phi_{I1} - \phi_I dA_1}{A}$, $d\phi_{I2} \leftarrow \dfrac{d\phi_{I2} - \phi_I dA_2}{A}$;

   }

Table 3.1: Pseudo-code for natural neighbor shape function computations at $\mathbf{x}$.

are the position vectors for the the circumcenter (open circle) of the natural neighbor circumcircles. Hence the natural neighbors of $\mathbf{x}$ are nodes 1, 2, 3, and 4, with the associated circumcircles $\mathbf{v}_{123}$ and $\mathbf{v}_{134}$ that correspond to $\triangle_{123}$ and $\triangle_{134}$, respectively. Let us first consider $\triangle_{123}$ and carry out the steps indicated in the shape function computations. We form new triangles, namely the triplets $(2, 3, \mathbf{x})$, $(3, 1, \mathbf{x})$ and $(1, 2, \mathbf{x})$ with circumcenters (open circles) $\mathbf{c}_{23\mathbf{x}}$, $\mathbf{c}_{31\mathbf{x}}$, and $\mathbf{c}_{12\mathbf{x}}$, respectively. Now, from the set $\{\mathbf{c}_{23\mathbf{x}}, \mathbf{c}_{31\mathbf{x}}, \mathbf{c}_{12\mathbf{x}}, \mathbf{v}_{123}\}$, we can construct three sub-triangles $(\mathbf{c}_{23\mathbf{x}}, \mathbf{c}_{31\mathbf{x}}, \mathbf{v}_{123})$, $(\mathbf{c}_{31\mathbf{x}}, \mathbf{c}_{12\mathbf{x}}, \mathbf{v}_{123})$, and $(\mathbf{c}_{12\mathbf{x}}, \mathbf{c}_{23\mathbf{x}}, \mathbf{v}_{123})$. The area of the above three sub-triangles is indicated by α_{it} (i = 1–3) in Eq. (3.43). By following a similar procedure for $\triangle_{134}$, we obtain the following three sub-triangles: $(\mathbf{c}_{34\mathbf{x}}, \mathbf{c}_{41\mathbf{x}}, \mathbf{v}_{134})$, $(\mathbf{c}_{41\mathbf{x}}, \mathbf{c}_{13\mathbf{x}}, \mathbf{v}_{134})$, and $(\mathbf{c}_{31\mathbf{x}}, \mathbf{c}_{34\mathbf{x}}, \mathbf{v}_{134})$. We note that the triplets $(\mathbf{c}_{41\mathbf{x}}, \mathbf{c}_{31\mathbf{x}}, \mathbf{v}_{134})$ and $(\mathbf{c}_{13\mathbf{x}}, \mathbf{c}_{34\mathbf{x}}, \mathbf{v}_{134})$ are oriented in the counter-clockwise direction, and hence contribute as negative areas. In addition, by noting the local $\rightarrow$ global nodal associations, we obtain the following results:

$$A_1(\mathbf{x}) = \Psi(\mathbf{c}_{31\mathbf{x}}, \mathbf{c}_{12\mathbf{x}}, \mathbf{v}_{123}) + \Psi(\mathbf{c}_{41\mathbf{x}}, \mathbf{c}_{31\mathbf{x}}, \mathbf{v}_{134}) \equiv \text{Area}\,(\square_{12\mathbf{x}-123-134-41\mathbf{x}}), \tag{3.48a}$$

$$A_2(\mathbf{x}) = \Psi(\mathbf{c}_{12\mathbf{x}}, \mathbf{c}_{23\mathbf{x}}, \mathbf{v}_{123}) \equiv \text{Area}\,(\triangle_{12\mathbf{x}-23\mathbf{x}-123}), \tag{3.48b}$$

$$A_3(\mathbf{x}) = \Psi(\mathbf{c}_{23\mathbf{x}}, \mathbf{c}_{31\mathbf{x}}, \mathbf{v}_{123}) + \Psi(\mathbf{c}_{13\mathbf{x}}, \mathbf{c}_{34\mathbf{x}}, \mathbf{v}_{134}) \equiv \text{Area}\,(\square_{134-123-23\mathbf{x}-34\mathbf{x}}), \tag{3.48c}$$

$$A_4(\mathbf{x}) = \Psi(\mathbf{c}_{34\mathbf{x}}, \mathbf{c}_{41\mathbf{x}}, \mathbf{v}_{134}) \equiv \text{Area}\,(\triangle_{34\mathbf{x}-41\mathbf{x}-134}), \tag{3.48d}$$

$$A(\mathbf{x}) = \sum_{I=1}^{4} A_I(\mathbf{x}), \tag{3.48e}$$

$$\phi_I(\mathbf{x}) = \frac{A_I(\mathbf{x})}{A(\mathbf{x})} \quad (I = 1,\ 2,\ 3,\ 4). \tag{3.48f}$$

It is immediately seen that the areas computed for each node in Fig. 3.13 are precisely

those seen in Figures 3.2b and 3.13. As indicated in the above equation, the shape functions for each node are just the areas normalized with respect to the total area.

Watson's algorithm (Watson, 1994) for the computation of NEM shape functions is foolproof for any point that does not lie along an edge of a Delaunay triangle, since the circumcenters of all triangles that need to be constructed are unique. It does, however, fail if a point $\mathbf{x}$ lies along the edge of a Delaunay triangle. This is so, since if the point $\mathbf{x}$ lies along an edge, say A–B of a triangle (A, B, C), then the new triangle $(A, B, \mathbf{x})$ formed in the algorithm has a non-unique circumcenter ($R(\mathbf{x}) = \pm\infty$). In the numerical integration of the weak form, since all points are interior to the triangle, this situation never arises.

There are alternative means to carry out the area computations. A straightforward approach is to compute the area of the polygons ($2nd$-order Voronoi cells) directly. Since the vertices of the polygon are the circumcenter of triangles formed from the natural neighbor nodal set and the point $\mathbf{x}$, one can use the algorithm mentioned in O'Rourke (1994) to compute the area of the polygon. An additional step involved in this is that the vertices of the polygon need to be sorted in counter-clockwise orientation. Lasserre's algorithm (Lasserre, 1983) for volume of convex polytopes in R^d is based on solving a constrained (bounded hyperplanes) linear programming problem to compute the volume of the polytopes. Braun and Sambridge (1995) used this algorithm to compute the natural neighbor shape function in their PDE application. This approach is robust, and is applicable at any point in the domain for shape function computations.

3.4.4 Computational Costs

The computational costs incurred in the implementation and execution of any numerical method is a critical component in the evaluation of its feasibility, usability, and potential for mid- to large-scale applications. Finite elements, in addition to their nice local (polynomial) properties, are a computationally attractive choice because of the very fast execution times that are attainable. The key differences that demarcate NEM from FEM is in the construction and numerical computation of the shape functions, and in the methodology used to assemble the stiffness matrix $\mathbf{K}$. All other steps are common to both, and hence we focus out attention on just the above two differences. In the finite element method, all shape function computations involve basic linear algebraic calculations. In NEM, the key time-consuming steps are:

1. Dirichlet tessellation (Voronoi diagram) of the nodes. As indicated in Section 3.1, the optimum time-complexity of triangulation algorithms in 2D is $\mathcal{O}(n \log n)$. The Delaunay triangulation of up to a million nodes can be carried out in less than one minute, and hence in two-dimensions, this step is not burdensome.

2. The search for natural neighbors for a sampling point $\mathbf{x}$. If the total number of triangles is only in the few thousands, searching through all the triangles, which is a $\mathcal{O}(n^2)$ algorithm, is not prohibitively expensive and is a feasible approach. If the number of triangles is of $\mathcal{O}(10^5)$ or greater, the walking-triangle algorithm due to Lawson (Lawson, 1977), which is a $\mathcal{O}(n)$ algorithm, is a suitable choice.

3. The numerical computations of the NEM shape functions is outlined in Section 3.4. All the steps involved in the algorithm are purely algebraic in nature,

with no matrix or vector computations.

4. The assembly of the stiffness matrix $\mathbf{K}$ in NEM is carried out on a nodal-basis. In finite elements, an element stiffness matrix structure which is common to all elements is used in the assembly of the global stiffness matrix $\mathbf{K}$. In NEM, since the number of neighbors for a point $\mathbf{x}$ is fairly small ($n_{max} = 11$ for the irregular grid in Fig. 3.6), the nodal-based assembly is not overly time-intensive.

On the basis of the numerical results that are presented in Section 4.4, the shape function timings on a HP9000/s700 workstation are about a factor of 1–2 slower than that for constant strain finite elements. In two-dimensions, since the solution phase dominates for a problem with significant number of degrees of freedom (10^4 or higher), the overall timing comparison of NEM to FEM is even smaller.

3.5 NEM, FEM, and Meshless Methods

We compare and contrast the natural element method to the finite element method and meshless methods. The local interpolant in FEM is constructed on the basis of an element structure, and in most meshless methods the local approximation is based on weight functions of compact support. The NEM interpolant uses a normalized Lebesgue measure that takes into account the distribution of nodes and their relation to each other in space—it has a very distinct meshless character for one can associate an anisotropic weight function of compact support with its construction. Interpolation to nodal data is realized in FEM and NEM which facilitates ease of imposing essential boundary conditions; in Galerkin methods that use meshless approximations, typically Lagrange multipliers, modified variational principles, or

coupling to finite elements is adopted to enforce essential boundary conditions. In one-dimension, the natural element method is identical to linear finite elements, but no such precise association with finite elements exists for other meshless methods. All these Galerkin methods possess the property of linear completeness which is a sufficient condition for convergence in the application to second-order elliptic PDEs. The distinction lies only in the manner in which the linear completeness conditions are enforced or obtained. In meshless methods, the approximation spaces beget the continuity of the weight function for smooth problems and hence higher-order continuous (C^k, $k > 0$) trial functions are readily constructed; traditional FEM are C^0, and NEM is smooth everywhere except at the nodes where it is C^0. The local approximation spaces in finite elements are uniformly independent (Strang and Fix, 1973). On the other hand, irregular nodal arrangements in meshless approximations such as EFG do result in marked deterioration in the properties of the approximation space. This is so since isotropic weight functions are noticeably biased towards regions of higher nodal density, at the expense of equi-directionality which is contended to be an essential ingredient for good approximability. The density and spatial location of nodes are taken into account in the construction of the natural neighbor interpolant. This allows for a natural means to construct stable approximation spaces that are based on irregular nodal arrangements. In this work, the Delaunay triangles which are the dual of the Voronoi diagram, are used in the numerical computation of the NEM interpolant. However, unlike the finite element method where angle restrictions are imposed on the Delaunay triangles for the convergence of the method (Babuška and Aziz, 1976), no such constraints are imposed on the shape, size, and angles of the Delaunay triangles in NEM. Hence we see that NEM does bear similarities to both

FEM and meshless methods. If FEM and meshless methods such as EFG are deemed to lie at the opposite ends of a spectrum, one would be inclined and justified to place NEM in the middle.

Chapter 4

Natural Element Method for Two-Dimensional Elasticity

In this Chapter, we discuss the application of the natural element method to boundary value problems in two-dimensional linear elasticity. To this end, we first present the treatment of material discontinuities using NEM, and then describe the methodology to model non-convex bodies, such as two-dimensional bodies with cracks. Using the variational framework and Galerkin procedure outlined in Chapter 2, the weak form for two-dimensional linear elasticity and the discrete system of equations for the natural element method are developed. Finally, numerical results for various boundary value problems in two-dimensional elastostatics are presented.

4.1 Treatment of Material Discontinuities

The treatment of material discontinuities in a two-dimensional setting using NEM is presented. Some typical examples of material discontinuities are encountered in composite materials, phase-transformations, and inclusions in a matrix with different material properties. A nice exposition on the underlying variational formulation and

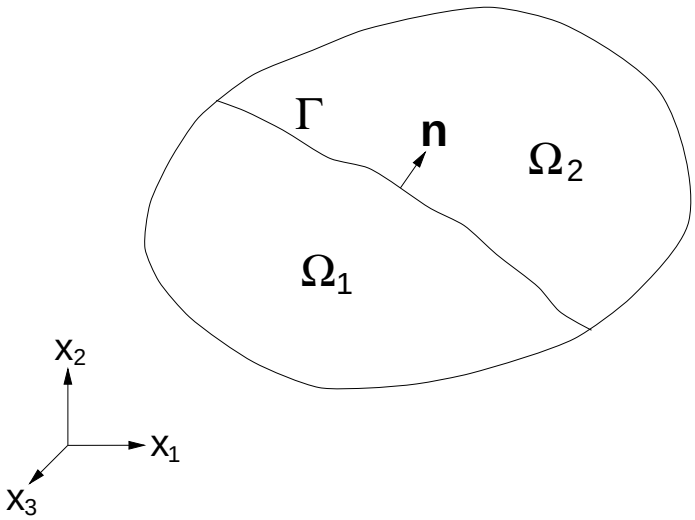

Figure 4.1: Bimaterial configuration ($\Omega = \Omega_1 \cup \Omega_2$).

finite element computations for this problem can be found in Mackinnon and Carey (1987).

Consider a two-dimensional body Ω, such that $\Omega = \Omega_1 \cup \Omega_2$, where Ω_1 and Ω_2 have different material properties. The interface between the two regions is Γ (Fig. 4.1). Since kinematically admissible displacement fields must be C^0, it is evident that displacement continuity must be met along the interface: $\mathbf{u}^1 = \mathbf{u}^2$ on Γ. An additional condition arises out of the variational principle—apart from the Euler-Lagrange equations, the natural interface condition is to be satisfied (in a weak sense), namely $\mathbf{t}^1 = \mathbf{t}^2$ along Γ. The above two conditions are automatically satisfied by the finite element interpolant if element boundaries are coincident with the discontinuity interface Γ. This is so, since the displacements are C^0, which allows for displacement gradients to be discontinuous in the normal direction ($\mathbf{n}$) to Γ.

The modeling of material discontinuities in the context of NEM follows. If the interface Γ is straight, then the description on convex domains in Section 3.3.9 holds,

and the displacement field $\mathbf{u}$ along Γ is strictly linear between adjacent nodes. Therefore, for this case, the interface displacement and traction continuity conditions are met. Of course, here, unlike FEM, one must explicitly disallow points in Ω_1 to be influenced by nodes in Ω_2 and vice-versa. A line-of-sight or visibility criterion (Belytschko et al., 1996), similar to that used by Cordes and Moran (1996) is invoked to meet the above requirement. Now, let us consider the case where either Ω_1 or Ω_2 is a non-convex domain. A plate consisting of a quarter-circle is considered. The circular domain Ω_1 is convex, while Ω_2 is non-convex. The circular arc is the material interface Γ that demarcates the two regions. The displacements along Γ are linear when approaching the interface from Ω_1, but are not so when approaching from Ω_2. In Section 3.3.9, the linearity of the displacement field along Γ for the domain Ω_2 is discussed. As indicated in Section 3.3.9, with sufficient nodal discretization of the interface Γ, the linearity of the displacement field can be met to within a desired tolerance ϵ. Since the trial functions are no longer C^0, the numerical implementation assumes the form of a non-conforming method. In Section 4.4.6, the problem of an inclusion in an infinite matrix is solved using NEM. For the grid shown in Fig. 4.19 with 13 nodes along Γ, the displacement discontinuity across Γ is less than 1% of the displacement values on either side.

4.2 Modeling of Non-Convex Bodies

The modeling of non-convex bodies, such as two-dimensional straight or curved cracks using the natural element method is addressed. Cracks are straight or curved lines of discontinuity in a two-dimensional body. From a modeling perspective, the numerical

formulation must permit a displacement discontinuity to exist across the crack line. In finite elements, this is facilitated by having coincident nodes with independent degrees of freedom along the line of discontinuity.

Consider a non-convex domain with a straight edge-crack, which is modeled using two distinct crack faces LC and MC (Fig. 4.2). The finite separation between the crack faces is illustrated for ease of exposition. Akin to the finite element method, one can also use coincident nodes with independent degrees of freedom along the crack line. In Fig. 4.2a, the nodes and the crack surfaces are shown while in Fig. 4.2b, the Delaunay triangles and the natural neighbor circumcircles for two triangles are presented. The triangulation of non-convex planar domains can be carried out using either conforming or constrained triangulation (Lo, 1989; Borgers, 1990). In a conforming triangulation, the empty circumcircle property is preserved, and the triangulation is the strict dual of the Voronoi diagram, while in a constrained triangulation, the duality property does not hold. In Fig. 4.2b, the triangulation shown is a conforming one, which ensures the duality with the Voronoi diagram. In order to include the crack surfaces in the numerical modeling, the crack faces LC and MC are treated as boundaries for the upper and lower regions, respectively. In effect, for the domain above the crack line, the Voronoi cells for the nodes along LC are unbounded, while for the domain below the crack line, the Voronoi cells for the nodes along the boundary MC are unbounded. If we construct the circumcircles for $\triangle_{ABC}$ and $\triangle_{CDE}$ as shown in Fig. 4.2b, the above description of crack modeling implies that nodes C, D, and E are natural neighbors of point $\mathbf{x}$, while nodes A and B are not. The above approach preserves the continuity of the trial function, and hence does not introduce any non-conformities in its implementation. In the modeling of crack problems where

symmetry (two-fold or four-fold) can be invoked such that the domain of interest is convex, no modifications in NEM are required.

4.2.1 Enriching the Interpolant for Crack Problems

The shape functions $\phi_I(\mathbf{x})$ form a partition of unity. As indicated in Section 3.3.2, this facilitates the enrichment of the NEM trial function for crack problems, along similar lines as suggested by Melenk and Babuška (1996). In finite elements, the quarter-point element results in $\sqrt{r}$ behavior in the displacement field along rays emanating from the crack-tip. Since the exact displacement field solution for crack problems is $\mathcal{O}(\sqrt{r})$, this enhancement permits accurate modeling of the radial dependence of the crack-tip field in two-dimensions. In the context of NEM, one can extrinsically enhance the trial function by adding terms that have local $\sqrt{r}$ behavior. Let $\Omega_0 \subset \Omega$ be a sub-domain in a region around the crack-tip where the crack-tip singularity dominates. Then the enriched trial function for two-dimensional crack problems assumes the form:

$$u_i^h(\mathbf{x}) = \sum_{I=1}^{n} \phi_I(\mathbf{x}) u_{Ii} + \sqrt{r} \sum_{\substack{J=1 \\ \mathbf{x}_J \in \Omega_0}}^{m} \phi_J(\mathbf{x}) a_{Ji} \quad (i = 1, 2), \tag{4.1}$$

where a_{Ji} are additional nodal coefficients that are associated with the m nodes in Ω_0. The above form indicates that by incorporating the enrichment over the support of the nodes in Ω_0, the crack-tip displacement field is accurately modeled. Enriching FEM along similar lines could provide enriched trial function spaces of wider-scope and possibly better merit than the quarter-point element. In this thesis, the enriched interpolant is not used for the crack problem presented in Section 4.4.7; the NEM trial function given in Eq. (3.6) is used.

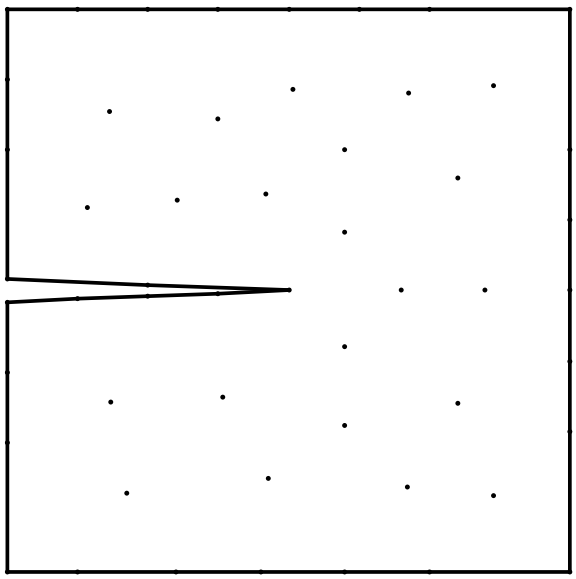

(a)

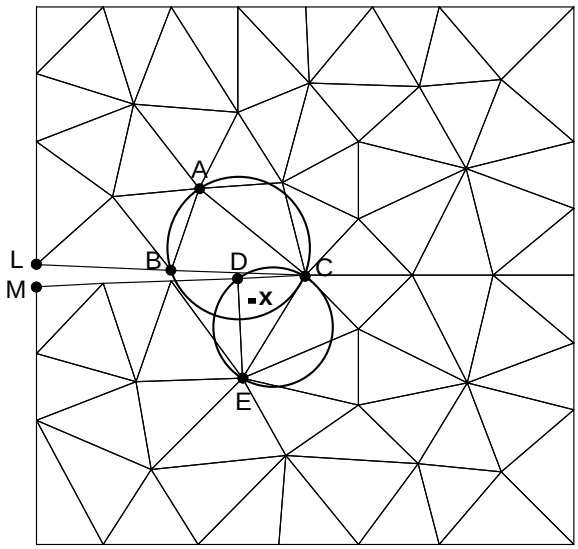

(b)

Figure 4.2: Crack modeling. (a) Nodes, and (b) Conforming triangulation.

4.3 Governing Equations and Weak Form

4.3.1 Strong Form

Consider a body which is described by an open bounded domain $\Omega \subset \mathbb{R}^2$, with boundary Γ. The set Γ is partitioned into two sets Γ_u (essential boundary) and Γ_t (natural boundary), with $\Gamma = \Gamma_u \cup \Gamma_t$ and $\Gamma_u \cup \Gamma_t = \emptyset$. The boundary value problem of elastostatics models the displacement $\mathbf{u}(\mathbf{x})$ of a body Ω which is fixed along Γ_u and subjected to surface forces (tractions) along Γ_t (Fig. 4.3). We now consider the

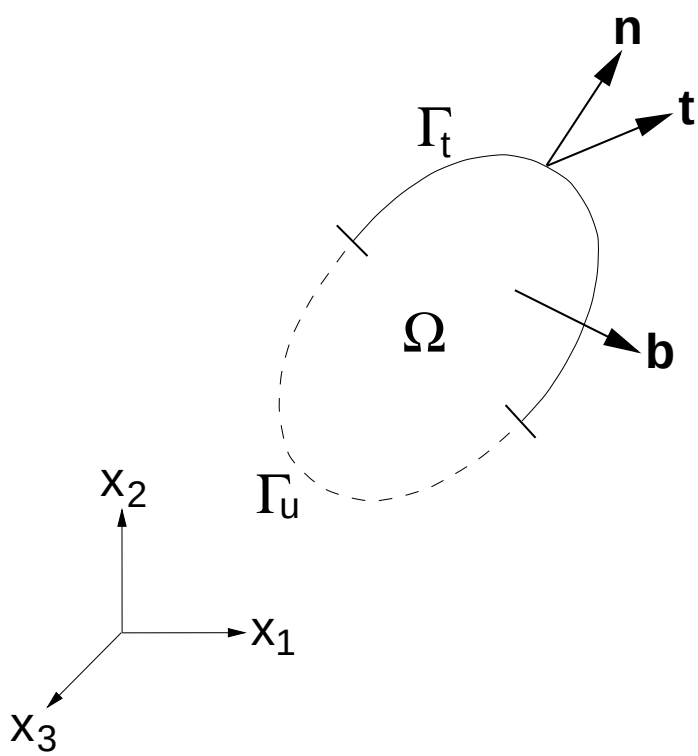

Figure 4.3: Elastostatic boundary value problem.

boundary value problem for small displacement elastostatics. The field equations of

elastostatics are:

$$\sigma_{ji,j} + b_i = 0 \quad \text{in} \quad \Omega, \tag{4.2a}$$

$$\sigma_{ij} = \sigma_{ji}, \tag{4.2b}$$

$$\sigma_{ij} = C_{ijkl}(\varepsilon_{kl} - \varepsilon^*_{kl}), \tag{4.2c}$$

$$\varepsilon_{ij} = \frac{1}{2}(u_{i,j} + u_{j,i}), \tag{4.2d}$$

where $\mathbf{C}$ is the material moduli tensor which for a homogeneous isotropic material with material parameters λ and μ (Lamé constants) is given by

$$C_{ijkl} = \lambda\delta_{ij}\delta_{kl} + \mu(\delta_{ik}\delta_{jl} + \delta_{il}\delta_{jk}). \tag{4.2e}$$

The Einstein summation convention on repeated indices is implied in Eq. (4.2), and the indices i, j, k, and l take on values 1, 2, and 3. In Eq. (4.2), σ_{ij} is the Cauchy stress for a kinematically admissible displacement field u_i, ε_{ij} is the small strain tensor, b_i is the body force per unit volume, and ε^*_{kl} is an imposed eigenstrain tensor. Equation (4.2a) is the equilibrium equation of elastostatics (conservation of linear momentum); the symmetry of the Cauchy stress in Eq. (4.2b) is a consequence of the conservation of angular momentum; Eq. (4.2c) is the linear elastic constitutive relation; and Eq. (4.2d) is the kinematic relation between the small strain tensor and the displacement vector. The eigenstrain tensor given in Eq. (4.2c) is included in the formulation to permit the treatment of a transformation strain problem that appears in Section 4.4.6.

Displacement (essential) boundary conditions are imposed on Γ_u and traction

(natural) boundary condition on Γ_t. The essential and natural boundary conditions are:

$$u_i = \bar{u}_i \quad \text{on} \quad \Gamma_u, \tag{4.3a}$$

$$t_i = \sigma_{ji} n_j = \bar{t}_i \quad \text{on} \quad \Gamma_t, \tag{4.3b}$$

where n_i is the unit outward normal to Ω, and $\bar{u}_i$ and $\bar{t}_i$ are prescribed displacements and tractions, respectively.

4.3.2 Weak Form

Let $\mathbf{u}$ be the displacement solution for an elastostatic boundary value problem, with $\boldsymbol{\sigma}(\mathbf{u})$ the corresponding Cauchy stress tensor. In the absence of inertial forces, the Cauchy stress σ_{ij} satisfies the equilibrium equation of elastostatics:

$$\sigma_{ji,j} + b_i = 0 \quad \text{in} \quad \Omega. \tag{4.4}$$

The equilibrium equation is a set of two coupled second-order ($m = 1$) elliptic partial differential equations. On the basis of the exposition in Section 2.2, we choose the displacement trial solution $\mathbf{u} \in \mathbf{V} = \left(H^1(\Omega)\right)^2$, and let $\mathbf{v} \in \mathbf{V}_0 = \left(H^1_0(\Omega)\right)^2$ be any set of kinematically admissible test functions (virtual displacements). The Sobolev spaces $H^1(\Omega)$ and $H^1_0(\Omega)$ are defined in Section 2.1.1. On multiplying Eq. (4.4) by v_i and integrating over Ω, we obtain

$$\int_\Omega \sigma_{ji,j} v_i \, d\Omega + \int_\Omega b_i v_i \, d\Omega = 0. \tag{4.5}$$

Re-writing the first integral in terms of the gradient of the product $\sigma_{ji}v_i$, we have

$$\int_\Omega (\sigma_{ji}v_i)_{,j}\, d\Omega - \int_\Omega \sigma_{ji}v_{i,j}\, d\Omega + \int_\Omega b_i v_i\, d\Omega = 0. \tag{4.6}$$

On using Green's formula from Eq. (2.19a) in Eq. (4.6), we obtain

$$\int_\Gamma \sigma_{ji}n_j v_i\, d\Gamma - \int_\Omega \sigma_{ji}v_{i,j}\, d\Omega + \int_\Omega b_i v_i\, d\Omega = 0. \tag{4.7}$$

By invoking Cauchy's formula given in Eq. (4.3b), the above equation takes the form

$$\int_\Gamma \bar{t}_i v_i\, d\Gamma - \int_\Omega \sigma_{ji}v_{i,j}\, d\Omega + \int_\Omega b_i v_i\, d\Omega = 0. \tag{4.8}$$

Since $\boldsymbol{\sigma}$ is a symmetric second-order tensor ($\sigma_{ij} = \sigma_{ji}$), we have the relation:

$$\sigma_{ji}v_{i,j} = \frac{\sigma_{ij}}{2}(v_{i,j} + v_{j,i}) = \sigma_{ij}(\mathbf{u})\varepsilon_{ij}(\mathbf{v}), \tag{4.9}$$

where the explicit dependence on the trial and test functions is indicated. On substituting the above identity in Eq. (4.8) and re-arranging the terms, we obtain

$$\int_\Omega \sigma_{ij}(\mathbf{u})\varepsilon_{ij}(\mathbf{v})\, d\Omega = \int_\Omega b_i v_i\, d\Omega + \int_\Gamma \bar{t}_i v_i\, d\Gamma. \tag{4.10}$$

Since the test functions v_i vanish on the essential boundary Γ_u, we obtain the result:

$$\boxed{\begin{array}{c}\text{Find } \mathbf{u} \in \mathbf{V} \text{ such that} \\ \displaystyle\int_\Omega \boldsymbol{\sigma}(\mathbf{u}) : \boldsymbol{\varepsilon}(\mathbf{v})\, d\Omega = \int_\Omega \mathbf{b}\cdot\mathbf{v}\, d\Omega + \int_{\Gamma_t} \bar{\mathbf{t}}\cdot\mathbf{v}\, d\Gamma \quad \forall\ \mathbf{v} \in \mathbf{V}_0.\end{array}} \tag{4.11}$$

Equation (4.11) is the weak or variational form of the equilibrium equation of linear elastostatics. In solid mechanics, the weak form is also referred to as the principle of virtual work. By using the constitutive relation given in Eqs. (4.2c) and (4.2e), we can write Eq. (4.11) in the variational framework indicated in Eq. (2.15) (see Chapter 2):

$$\text{Find } \mathbf{u} \in \mathbf{V} \text{ such that}$$

$$a(\mathbf{u}, \mathbf{v}) = \langle l, \mathbf{v} \rangle \quad \forall\ \mathbf{v} \in \mathbf{V}_0, \tag{4.12a}$$

where

$$a(\mathbf{u}, \mathbf{v}) = 2\mu\big(\boldsymbol{\varepsilon}(\mathbf{u}), \boldsymbol{\varepsilon}(\mathbf{v})\big) + \lambda(\text{div } \mathbf{u}, \text{div } \mathbf{v}), \tag{4.12b}$$

$$\langle l, \mathbf{v} \rangle = (\mathbf{b}, \mathbf{v}) + (\bar{\mathbf{t}}, \mathbf{v}). \tag{4.12c}$$

In the above equations, the $L^2(\Omega)$ inner product for vectors and second-order tensors is defined as:

$$(\mathbf{u}, \mathbf{v}) = \int_\Omega \mathbf{u} \cdot \mathbf{v}\, d\Omega, \quad (\mathbf{A}, \mathbf{B}) = \int_\Omega \mathbf{A} : \mathbf{B}\, d\Omega, \tag{4.13}$$

where $\mathbf{u}$ and $\mathbf{v}$ are vectors, and $\mathbf{A} : \mathbf{B} = A_{ij}B_{ij}$ is the scalar product (double contraction) for symmetric second-order tensors $\mathbf{A}$ and $\mathbf{B}$ (Malvern, 1969).

4.3.3 Discrete System and NEM Implementation

Consider the Bubnov-Galerkin implementation for the natural element method in two-dimensional linear elasticity. In the natural element method, finite-dimensional

subspaces $\mathbf{V}^h \subset \mathbf{V}$ and $\mathbf{V}_0^h \subset \mathbf{V}_0$ are used as the approximating trial and test spaces. The weak form for the discrete problem can be stated as:

$$\text{Find } \mathbf{u}^h \in \mathbf{V}^h \subset \mathbf{V} \quad \text{such that}$$
$$\int_{\Omega^h} \boldsymbol{\sigma}(\mathbf{u}^h) : \boldsymbol{\varepsilon}(\mathbf{v}^h) = \int_{\Omega^h} \mathbf{b} \cdot \mathbf{v}\, d\Omega + \int_{\Gamma^h} \bar{\mathbf{t}} \cdot \mathbf{v}\, d\Gamma \quad \forall\, \mathbf{v}^h \in \mathbf{V}_0^h \subset \mathbf{V}_0. \tag{4.14}$$

In a Bubnov-Galerkin procedure, the trial functions $\mathbf{u}^h$ as well as the test functions $\mathbf{v}^h$ are represented as linear combinations of the same shape functions. The trial and test functions are

$$\mathbf{u}^h(\mathbf{x}) = \sum_{I=1}^{n} \phi_I(\mathbf{x})\mathbf{u}_I, \quad \mathbf{v}^h(\mathbf{x}) = \sum_{I=1}^{n} \phi_I(\mathbf{x})\mathbf{v}_I. \tag{4.15}$$

On substituting the trial and test functions from Eq. (4.15) in Eq. (4.14), and using the arbitrariness of nodal variations, the following discrete system of linear equations is obtained:

$$\boldsymbol{K}\mathbf{d} = \mathbf{f}, \tag{4.16}$$

where

$$\mathbf{K}_{IJ} = \int_{\Omega^h} \mathbf{B}_I^T \mathbf{C} \mathbf{B}_J\, d\Omega, \tag{4.17a}$$
$$\mathbf{f}_I = \int_{\Gamma_t^h} \phi_I \bar{\mathbf{t}}\, d\Gamma + \int_{\Omega^h} \phi_I \mathbf{b}\, d\Omega + \int_{\Omega^h} \boldsymbol{B}_I^T \mathbf{C} \boldsymbol{\varepsilon}^*\, d\Omega. \tag{4.17b}$$

In the above equations, $\mathbf{B}_I$ is the matrix of shape function derivatives which is given

by

$$\boldsymbol{B}_I = \begin{bmatrix} \phi_{I,x} & 0 \\ 0 & \phi_{I,y} \\ \phi_{I,y} & \phi_{I,x} \end{bmatrix}. \tag{4.18}$$

The constitutive matrix $\boldsymbol{C}$ for an isotropic linear elastic material is:

$$\boldsymbol{C} = \frac{E}{(1-2\nu)(1+\nu)} \begin{bmatrix} 1-\nu & \nu & 0 \\ \nu & 1-\nu & 0 \\ 0 & 0 & \dfrac{1-2\nu}{2} \end{bmatrix} \qquad \text{(plane strain)}, \tag{4.19a}$$

$$\boldsymbol{C} = \frac{E}{(1-\nu^2)} \begin{bmatrix} 1 & \nu & 0 \\ \nu & 1 & 0 \\ 0 & 0 & \dfrac{1-\nu}{2} \end{bmatrix} \qquad \text{(plane stress)}. \tag{4.19b}$$

In the context of the natural element method, the stiffness matrix $\mathbf{K}$ and external force vector $\mathbf{f}$ given in Eq. (4.17) are assembled on a nodal basis. This choice is necessitated due to the absence of an inherent element structure in NEM, as opposed to the finite element method where shape functions are constructed on the basis of elements. In addition, the stiffness matrix in NEM is symmetric and sparse, but not necessarily banded. The Delaunay triangles are used as the background integration cells for the numerical integration computations. It is to be noted that the Delaunay triangulation is just one among many choices to partition the domain for the purpose of numerical integration of the weak form; quadrilaterals or octree-based cell structures are also suitable choices for the numerical integration computations. An

alternative approach proposed by Traversoni (1994) involves carrying out the numerical integration over the area of intersection of circumcircles. The idea is appealing since tensor product terms such as $\phi_{I,i}\phi_{J,j}$ are non-zero over the area of intersection of circumcircles about nodes n_I and n_J. In spite of its merits, the mappings and transformations involved appear to be non-trivial, with no cubature scheme currently known for such domains. Hence this approach is not pursued in this work, and the Delaunay triangles themselves are used in the numerical integration of the weak form.

4.4 Numerical Results and Discussions

The application of NEM to problems in small displacement two-dimensional elastostatics, in the absence of body forces, is presented. Unless stated otherwise, the material properties chosen in the analyses are: $E = 3 \times 10^7$ psi and $\nu = 0.25$. Numerical integration is carried out using symmetric quadrature rules for a triangle (Lyness and Jespersen, 1975; Dunavant, 1985). Three point quadrature rule is used in the numerical integration of the weak form; the error norm computations are carried out using 25 point quadrature rule in each triangle.

4.4.1 Eigenanalysis

In order to study the properties of the approximation spaces of NEM, we consider the linear independence of the shape functions (Strang and Fix, 1973). To this end, we consider the following discrete eigenvalue problem:

$$\mathbf{M}\hat{\mathbf{d}} = \lambda^h \hat{\mathbf{d}}, \tag{4.20}$$

where $\hat{\mathbf{d}}$ and λ^h are the eigenvectors and eigenvalues of $\mathbf{M}$, and $\mathbf{M}$ is the mass matrix (Gram matrix in linear algebra) which is given by

$$\mathbf{M}_{IJ} = \int_\Omega \phi_I \phi_J \, d\Omega. \tag{4.21}$$

The condition number $\kappa(\mathbf{M})$ of the matrix $\mathbf{M}$ is defined as the ratio of the maximum eigenvalue $\lambda_{\max}(\mathbf{M})$ to that of the minimum eigenvalue $\lambda_{\max}(\mathbf{M})$. The condition number is used as a measure of the linear independence of the shape functions. If the shape functions were orthonormal, $\mathbf{M}_{IJ}$ would be the identity matrix and $\kappa = 1$. The EISPACK (Smith, Boyle, Garbow, Ikebe, Klema, and Moler, 1974) eigensolver package is used to solve the eigenvalue problem. In Table 4.1, the condition number is computed for the nodal grid shown in Fig. 4.4a and uniform refinements of the same grid; in addition, results are also computed for the nodal grid shown in Fig. 4.4c and for the irregular focused grid in Fig. 4.21b that is used for the edge crack problem in Section 4.4.7. The condition numbers obtained for NEM are of the same order as constant strain finite elements for both the uniform and non-uniform nodal discretization which indicates that the matrix is well-conditioned and the approximation spaces are linearly independent.

4.4.2 Patch Tests

The patch test (Bazeley, Cheung, Irons, and Zienkiewicz, 1965; Irons and Razzaque, 1972) is the ubiquitous test for the convergence of non-conforming finite element methods. Even though there remains significant disagreement as to whether it is a necessary condition for convergence, its merit and use as a benchmark for the eval-

Table 4.1: Linear independence of C^0 shape functions.

Grids	Nodes	κ^h_{NEM} Quadrature 3	κ^h_{NEM} Quadrature 25	κ^h_{FEM}
Uniform	25	3.99	3.83	7.00
	289	3.99	3.83	7.00
	4225	3.99	3.83	7.00
Non-uniform	70	50.86	35.65	43.17
	278	2148.97	2146.45	3422.31

uation and validation of non-conforming elements is unquestionable. For a historical perspective and review of the patch test, see Felippa, Haugen, and Militello (1995). In the context of meshless methods, the relevance of the patch test from the viewpoint of convergence is still an open issue, which needs to be addressed and understood in a better light.

Displacement In the displacement patch test, a linear displacement field is imposed on the boundary Γ_u ($\Gamma_u = \partial\Omega$) of a domain Ω. If the patch test is passed, the linear displacement field is approximated exactly, and the numerical solution at the interior nodes should be in exact (within machine precision) agreement with the linear

solution. This validates, apart from the consistency condition, the accuracy of the numerical integration of the weak form in the Galerkin implementation. In Fig. 4.4, three different nodal discretizations for a unit square are shown. In Fig. 4.4a, a uniform grid with 25 nodes is considered; an irregular grid (8 nodes) is shown in Fig. 4.4c; and in Fig. 4.4e, a random set of 70 nodes is chosen. It is noted that for the uniform nodal grid shown in Fig. 4.4a, the Delaunay triangles are non-unique, even though the Voronoi diagram for the set of nodes is unique. A valid Delaunay triangulation for the regular nodal discretization is shown in Fig. 4.4b. For the displacement patch test, a linear displacement field $u_i = x_i$ is imposed on the boundary nodes of the unit square. We remark here that if all diagonals of the Delaunay triangles for the grid shown in Fig. 4.4a are aligned in the same direction, the $L^2(\Omega)$ and $H^1(\Omega)$ error norm results for three point quadrature in each triangle are 10^{-16} and 10^{-15}, respectively. This is a fortuitous result that is attributable to symmetry in the location of the quadrature points and cancellations in the numerical integration. This result does not merit presentation, since it is an anomaly. We do point it out here to emphasize the fact that a systematic study with large number of numerical tests should be carried out in order to draw a sound inference or (numerically) prove a claim for that matter.

The NEM displacement patch test results for the relative $L^2(\Omega)$ error norm and relative $H^1(\Omega)$ error norm are presented in Table 4.2. The $L^2(\Omega)$ and $H^1(\Omega)$ error

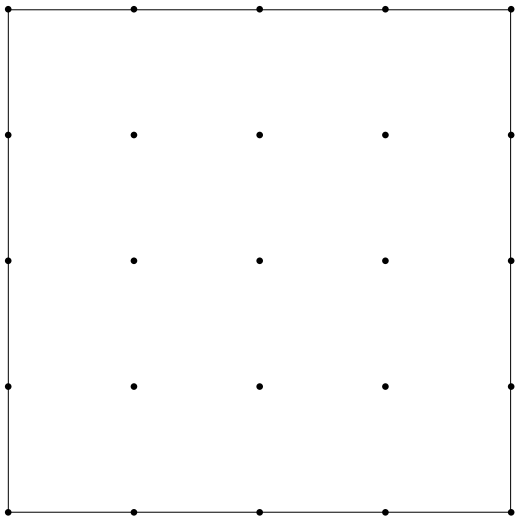

(a)

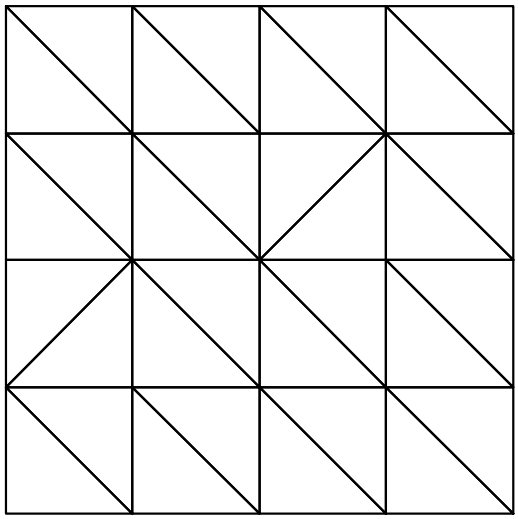

(b)

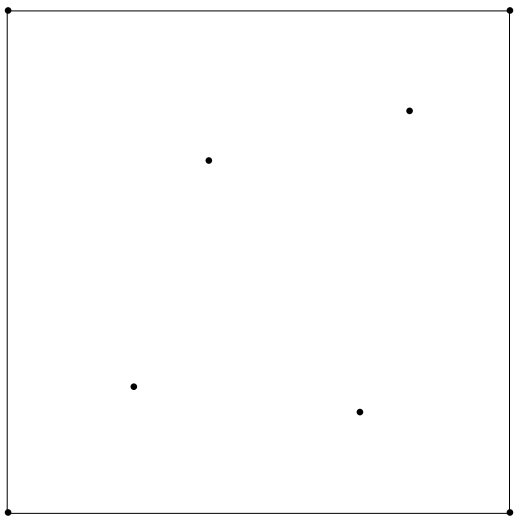

(c)

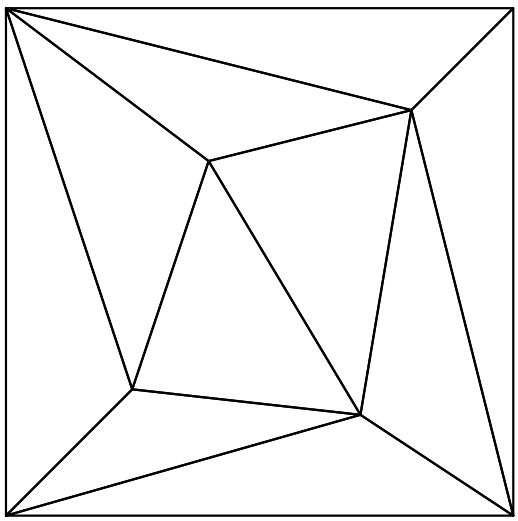

(d)

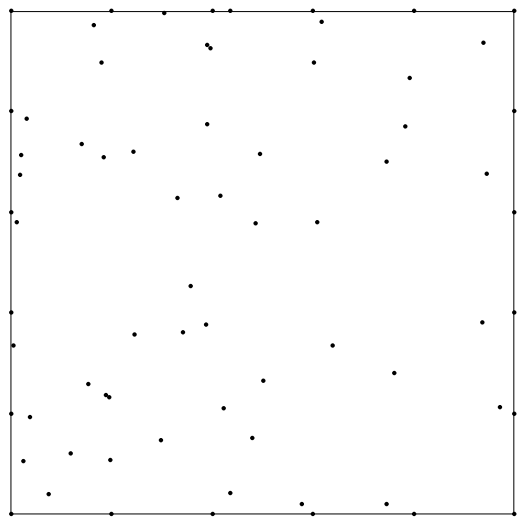

(e)

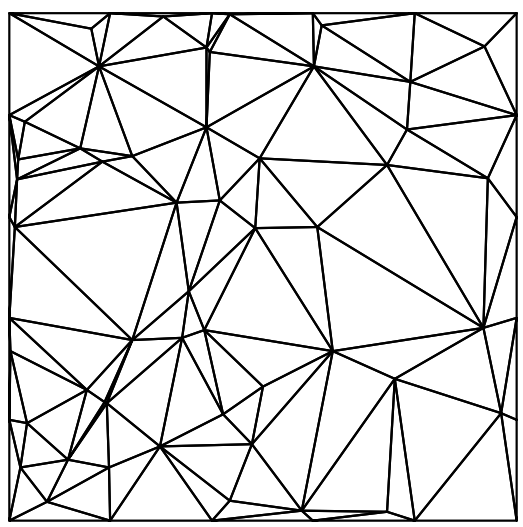

(f)

Figure 4.4: Displacement patch test. (a) and (b) Uniform grid (25 nodes), (c) and (d) Irregular grid (8 nodes), and (e) and (f) Random set (70 nodes).

norms are defined as follows:

$$\|\mathbf{u}-\mathbf{u}^h\|_{L^2(\Omega)} = \left(\int_\Omega (u_i - u_i^h)(u_i - u_i^h)\, d\Omega\right)^{1/2}, \tag{4.22a}$$

$$\|\mathbf{u}-\mathbf{u}^h\|_{H^1(\Omega)} = \left(\int_\Omega \left[(u_i - u_i^h)(u_i - u_i^h) + (u_{i,j} - u_{i,j}^h)(u_{i,j} - u_{i,j}^h)\right] d\Omega\right)^{1/2}, \tag{4.22b}$$

where $\mathbf{u}$ and $\mathbf{u}^h$ are the exact and numerical (NEM) displacement solutions, respectively. In Table 4.2, the results are shown for both, 3 point, as well 25 point quadrature within each Delaunay triangle. For the error norm computations, 25 point quadrature rule is used within each triangle. The error norm results indicate that the displacements and strains in the patch test are accurate to within 10^{-4} and 10^{-3}, respectively. Thus, since machine precision (double precision arithmetic) on a HP9000/s700 workstation is 10^{-16}, the patch test is not met with respect to this measure. Since the NEM interpolant can exactly reproduce a linear displacement field (Section 3.3.3), the numerical integration of the weak form is the source for the above discrepancy. Inexact numerical integration of the weak form (potential energy functional) is one of the variational crimes (Strang and Fix, 1973). In NEM, two factors lead to the numerical integration errors, namely, the non-polynomial form of the shape functions and the use of Delaunay triangles for numerical integration which are not coincident with the supports of the shape functions (Section 3.3.4). As indicated in Section 4.3.3, the natural domain for the numerical integration is the area of intersection (Ω_c) of natural neighbor circumcircles. There exist cubature rules with polynomial precision for two-dimensional domains such as, square, circle, triangle, and the plane (Stroud, 1971; Cools and Rabinowitz, 1997). In addition, adaptive numerical integration procedures for other planar domains that are affine transformation of the above primitives are

also available (Cools, Laurie, and Pluym, 1997). However, no general polynomial precision scheme for the domain Ω_c is known. It is envisaged that an easy-to-implement and robust numerical cubature scheme over Ω_c that is specifically tailored to the NEM interpolant could lead to significant improvements in the numerical integration. The above shortcoming of NEM with respect to the patch test is also seen in meshless methods. For instance, in EFG, typical relative $L^2(\Omega)$ error norms in displacements are obtained to within 10^{-6} accuracy with high Gauss-Legendre product rules over quadrilaterals for numerical integration. This again, is due to inexact numerical integration of the weak form.

Table 4.2: Relative error norms for the displacement patch test.

Grids	Quadrature	$\frac{\lVert \mathbf{u} - \mathbf{u}^h \rVert_{L^2(\Omega)}}{\lVert \mathbf{u} \rVert_{L^2(\Omega)}}$	$\frac{\lVert \mathbf{u} - \mathbf{u}^h \rVert_{H^1(\Omega)}}{\lVert \mathbf{u} \rVert_{H^1(\Omega)}}$
a	3	7.5×10^{-4}	4.0×10^{-3}
	25	8.4×10^{-5}	4.5×10^{-4}
c	3	9.3×10^{-3}	4.1×10^{-2}
	25	1.1×10^{-3}	4.3×10^{-3}
e	3	4.4×10^{-3}	9.2×10^{-2}
	25	4.8×10^{-4}	7.9×10^{-3}

Equilibrium The ability to represent a uniaxial plane stress field is verified by the equilibrium patch test. Consider a unit square plate under a uniaxial stress $\sigma = 1$ psi (plane stress conditions) in the x_2-direction (Fig. 4.5). The essential boundary conditions are indicated in Fig. 4.5. The exact displacement solution is:

$$u_1 = \frac{\nu}{E}(1 - x_1), \tag{4.23a}$$

$$u_2 = \frac{x_2}{E}. \tag{4.23b}$$

The three different nodal grids shown in Fig. 4.4 are considered for the equilibrium patch test, and the relative error norm results are presented in Table 4.3. In Table 4.3, the energy norm $\|\mathbf{u} - \mathbf{u}^h\|_{E(\Omega)}$ is defined as:

$$\|\mathbf{u} - \mathbf{u}^h\|_{E(\Omega)} = \left(\frac{1}{2}\int_\Omega (\boldsymbol{\varepsilon} - \boldsymbol{\varepsilon}^h)^T \mathbf{C}(\boldsymbol{\varepsilon} - \boldsymbol{\varepsilon}^h)\, d\Omega\right)^{1/2}. \tag{4.24}$$

In Table 4.3, it is seen that the relative error norms in displacement and in energy are 10^{-4} and 10^{-3}, respectively. These are comparable to the patch test results obtained in Section 4.4.2, and again, the disagreement with the exact solution is due to numerical integration errors.

4.4.3 Infinite Plate with a Circular Hole

An infinite plate with a traction free circular hole under unidirectional tension along x_1 is considered (Fig. 4.6). The exact solution to this problem is given in Timoshenko and Goodier (1970) as well as Szabó and Babuška (1991). The domain $ABCDE$ shown in Fig. 4.6 is modeled with the exact tractions imposed along BC and CD.

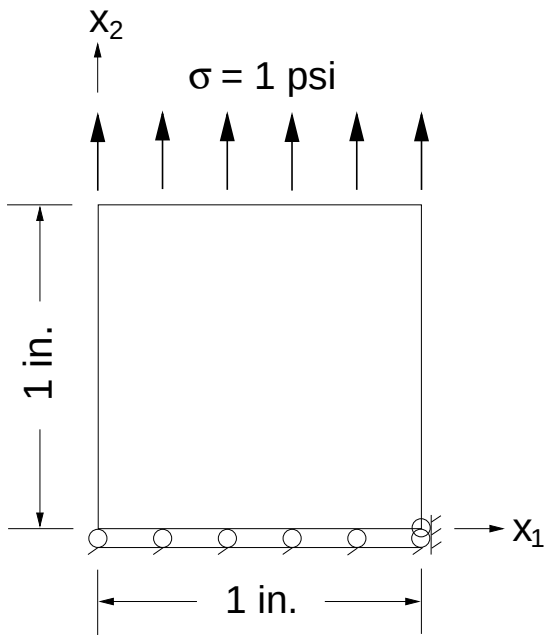

Figure 4.5: Equilibrium (uniaxial tension) patch test.

Table 4.3: Relative error norms for the equilibrium patch test.

Grids	Quadrature	$\frac{\lVert \mathbf{u} - \mathbf{u}^h \rVert_{L^2(\Omega)}}{\lVert \mathbf{u} \rVert_{L^2(\Omega)}}$	$\frac{\lVert \mathbf{u} - \mathbf{u}^h \rVert_{E(\Omega)}}{\lVert \mathbf{u} \rVert_{E(\Omega)}}$
a	3	1.8×10^{-3}	4.5×10^{-3}
	25	1.7×10^{-4}	4.4×10^{-4}
c	3	8.2×10^{-3}	3.2×10^{-2}
	25	1.4×10^{-3}	4.0×10^{-3}
e	3	6.1×10^{-3}	9.5×10^{-2}
	25	8.8×10^{-4}	6.9×10^{-3}

Due to symmetry, the essential boundary conditions are: $u_2 = 0$ along AB, and $u_1 = 0$ along DE. In polar coordinates (r, θ), the exact stress distribution for $\sigma_0 = 1$ psi is

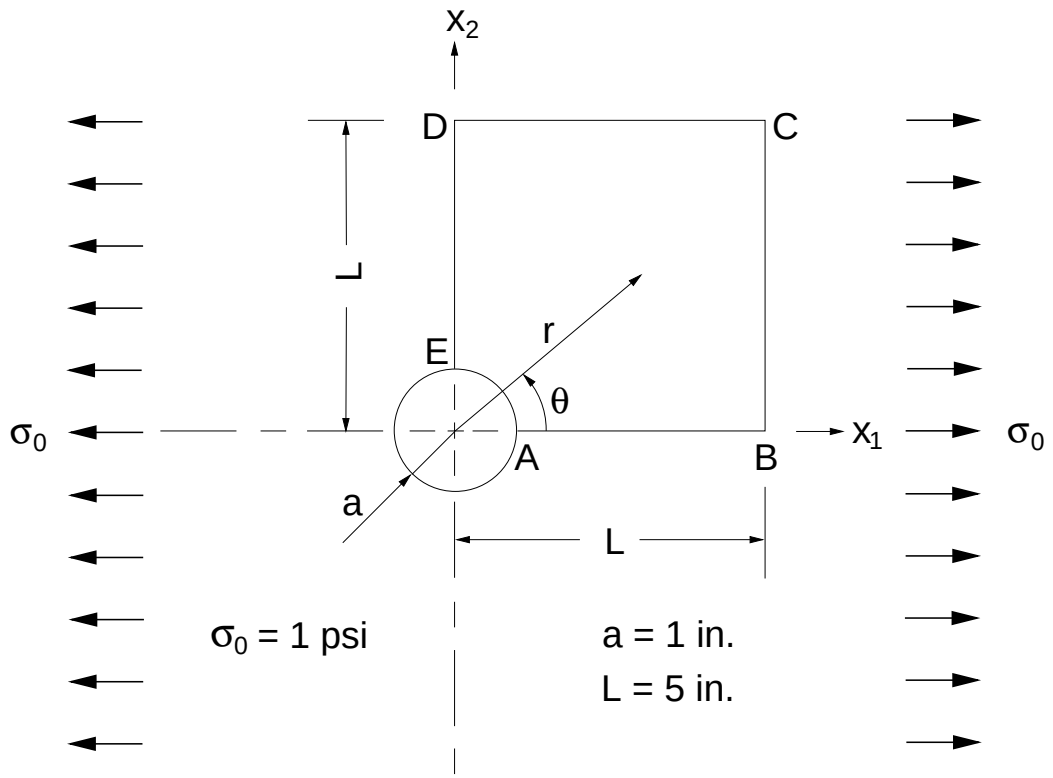

Figure 4.6: Plate with a circular hole under tension.

given by

$$\sigma_{11}(r,\theta) = 1 - \frac{a^2}{r^2}\left(\frac{3}{2}\cos 2\theta + \cos 4\theta)\right) + \frac{3}{2}\frac{a^4}{r^4}\cos 4\theta, \tag{4.25a}$$

$$\sigma_{22}(r,\theta) = -\frac{a^2}{r^2}\left(\frac{1}{2}\cos 2\theta - \cos 4\theta)\right) - \frac{3}{2}\frac{a^4}{r^4}\cos 4\theta, \tag{4.25b}$$

$$\sigma_{12}(r,\theta) = -\frac{a^2}{r^2}\left(\frac{1}{2}\sin 2\theta + \sin 4\theta)\right) + \frac{3}{2}\frac{a^4}{r^4}\sin 4\theta, \tag{4.25c}$$

where a is the radius of the circular hole. The displacement components (rigid-body displacement and rotation set to zero) are:

$$u_1(r,\theta) = \frac{a}{8\mu}\left[\frac{r}{a}(\kappa+1)\cos\theta + 2\frac{a}{r}((1+\kappa)\cos\theta + \cos 3\theta) - 2\frac{a^3}{r^3}\cos 3\theta\right], \tag{4.26a}$$

$$u_2(r,\theta) = \frac{a}{8\mu}\left[\frac{r}{a}(\kappa-3)\sin\theta + 2\frac{a}{r}((1-\kappa)\sin\theta + \sin 3\theta) - 2\frac{a^3}{r^3}\sin 3\theta\right], \tag{4.26b}$$

where μ is the shear modulus and κ (Kolosov constant) is defined as

$$\kappa = \begin{cases} 3-4\nu & \text{(plane strain)}, \\ \dfrac{3-\nu}{1+\nu} & \text{(plane stress)}. \end{cases} \tag{4.27}$$

In the numerical computations, $a = 1$ in., $L = 5$ in., and plane strain conditions are assumed. The nodal discretizations used in the computations are shown in Fig. 4.7. In Fig. 4.9, the rates of convergence (R) in displacement and energy for NEM and constant strain finite elements are presented. The theoretical convergence rates for the displacements and strains using finite elements (non-singular problems) are $R = 2$ and $R = 1$, respectively (see Eq. (2.33)). It is observed from Fig. 4.9 that the rates of convergence of NEM and FE are about the same, with NEM showing better absolute accuracy in displacements and strains. In Fig. 4.9a, the stress concentration factor ($\sigma_{11}^{exact}/\sigma_0 = 3$) at point E is indicated within parentheses. It is seen that NEM is able to accurately capture the stress concentration at point E. In Fig. 4.8, the numerical and exact normal stress σ_{11} are plotted along the edge ED (see Fig. 4.6). The grid shown in Fig. 4.7c is used, and 240 equi-spaced output points between $r = 1$ in. and $r = 5$ in. are chosen in the computations. Agreement between the NEM and the

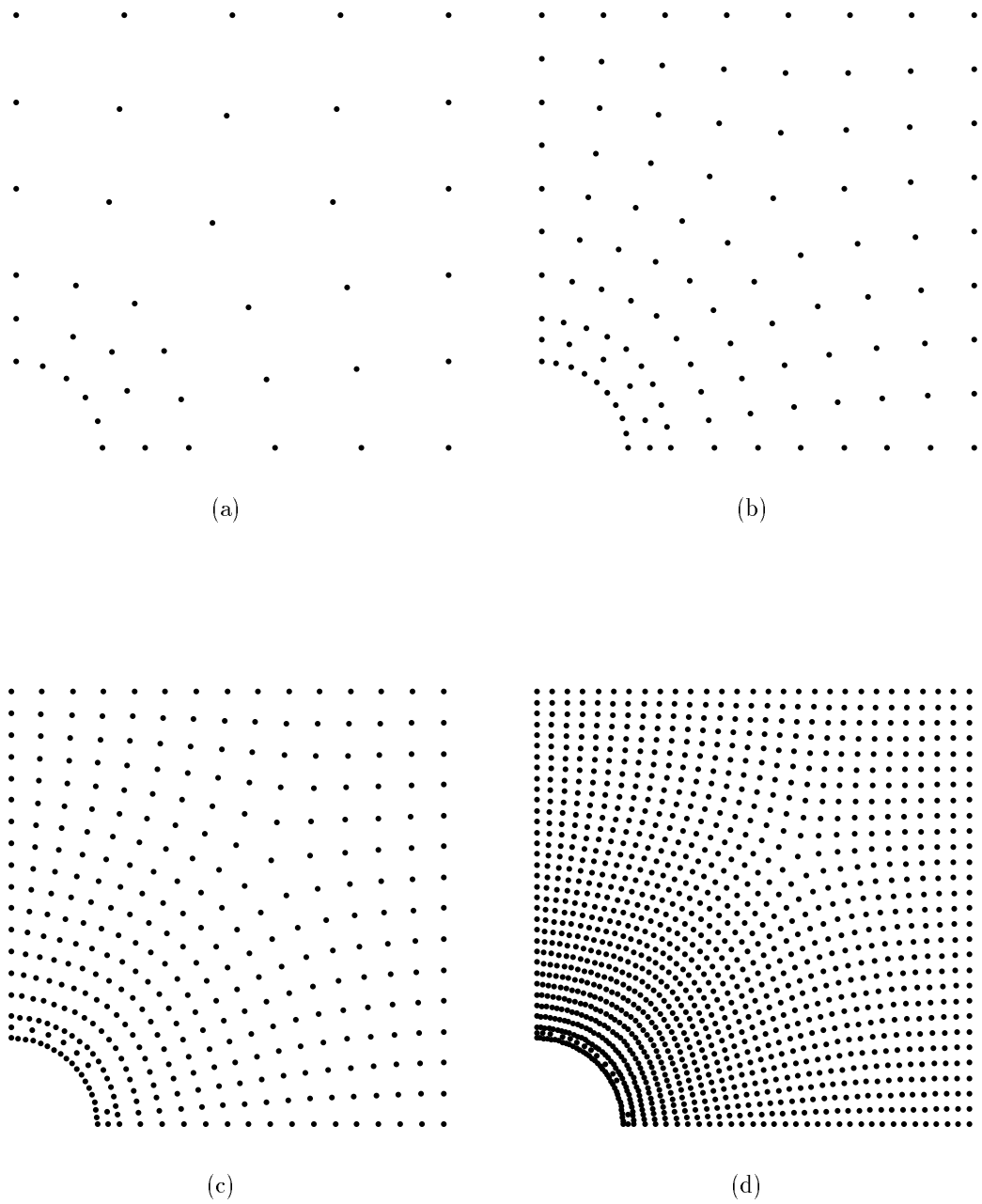

Figure 4.7: Nodal discretization for the plate with a hole problem. (a) 41 nodes, (b) 108 nodes, (c) 361 nodes, and (d) 1345 nodes.

exact stress solution is excellent. The displacement along the edge is linear between two adjacent nodes, and hence one observes the jumps in the stress σ_{11} at the nodes.

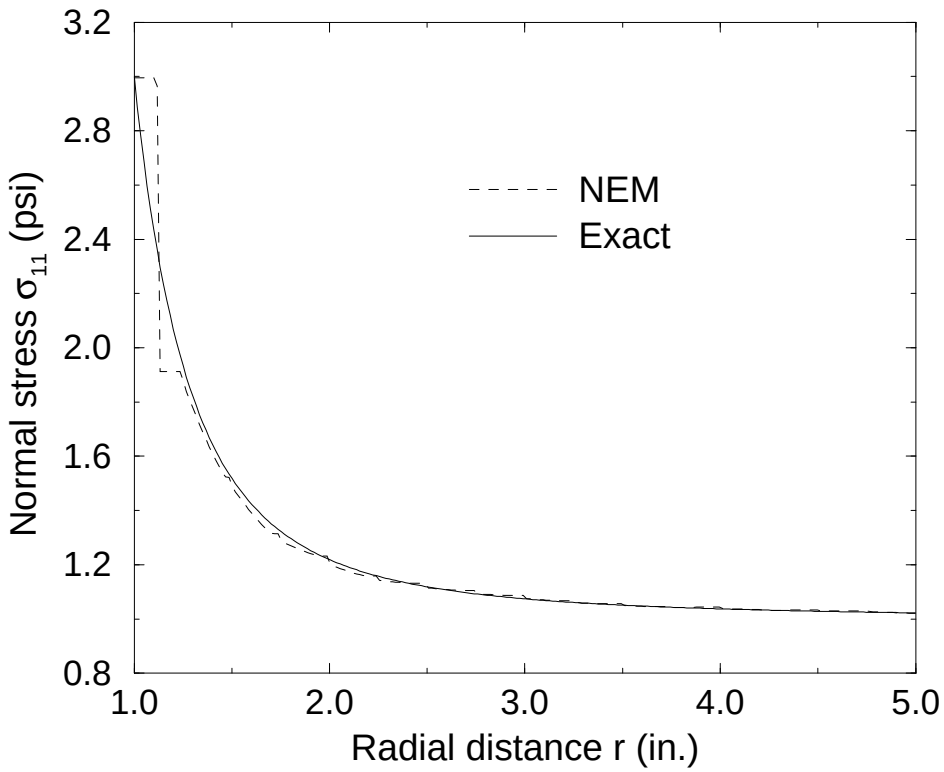

Figure 4.8: Comparison of σ_{11} for NEM and the exact solution along a radial line ($\theta = 90°$).

4.4.4 Cantilever Beam

In Fig. 4.10, a cantilever beam subjected to a parabolic end load is illustrated. The beam has length L, height D, and unit thickness. The displacement vector solution

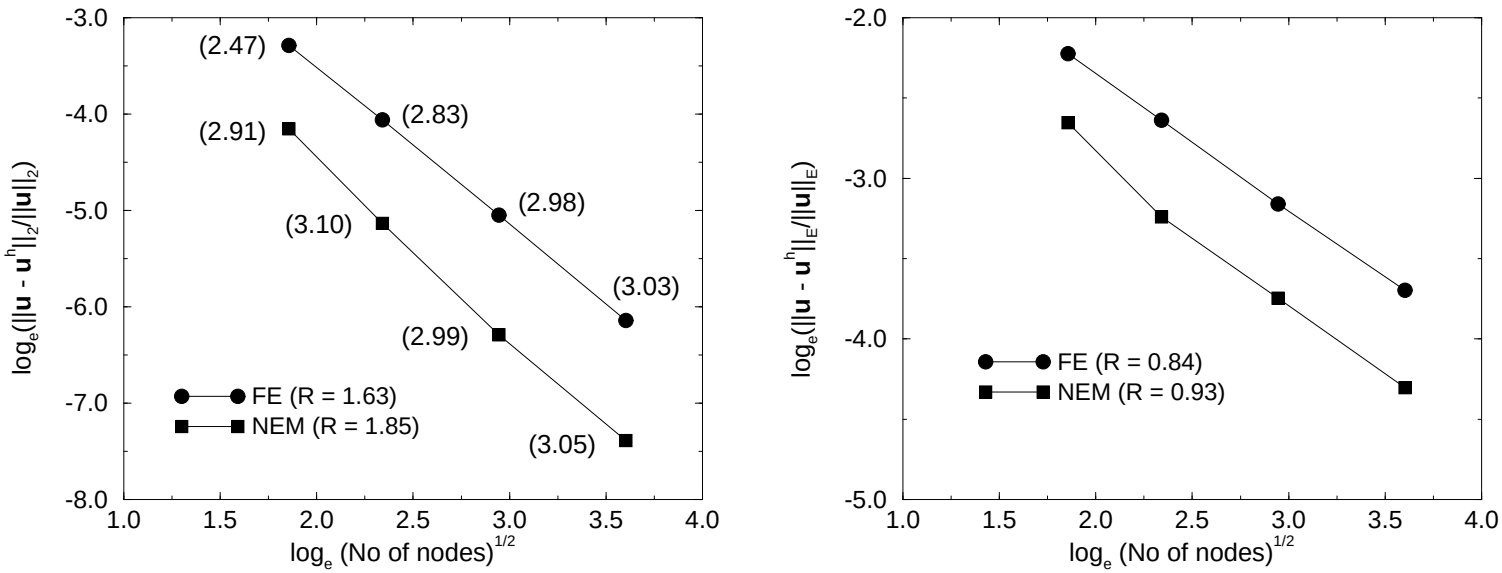

(a) (b)

Figure 4.9: Rate of convergence for the plate with a hole problem. (a) Displacement, and (b) Energy.

is given by (Timoshenko and Goodier, 1970)

$$u_1(x_1, x_2) = \frac{-Px_2}{6\bar{E}I}\left[(6L - 3x_1)x_1 + (2 + \bar{\nu})x_2^2 - \frac{3D^2}{2}(1 + \bar{\nu})\right], \tag{4.28a}$$

$$u_2(x_1, x_2) = \frac{P}{6\bar{E}I}\left[3\bar{\nu}x_2^2(L - x_1) + (3L - x_1)x_1^2\right], \tag{4.28b}$$

where

$$\bar{E} = \begin{cases} E & \text{(plane stress)}, \\ \dfrac{E}{1-\nu^2} & \text{(plane strain)}, \end{cases} \tag{4.29a}$$

$$\bar{\nu} = \begin{cases} \nu & \text{(plane stress)}, \\ \dfrac{\nu}{1-\nu} & \text{(plane strain)}. \end{cases} \tag{4.29b}$$

The stresses are given by

$$\sigma_{11}(x_1, x_2) = \frac{-P(L - x_1)x_2}{I}, \tag{4.30a}$$

$$\sigma_{22}(x_1, x_2) = 0, \tag{4.30b}$$

$$\sigma_{12}(x_1, x_2) = \frac{P}{2I}\left(\frac{D^2}{4} - x_2^2\right), \tag{4.30c}$$

where I is the moment of inertia, which for a beam with rectangular cross-section and unit thickness is:

$$I = \frac{D^3}{12}. \tag{4.30d}$$

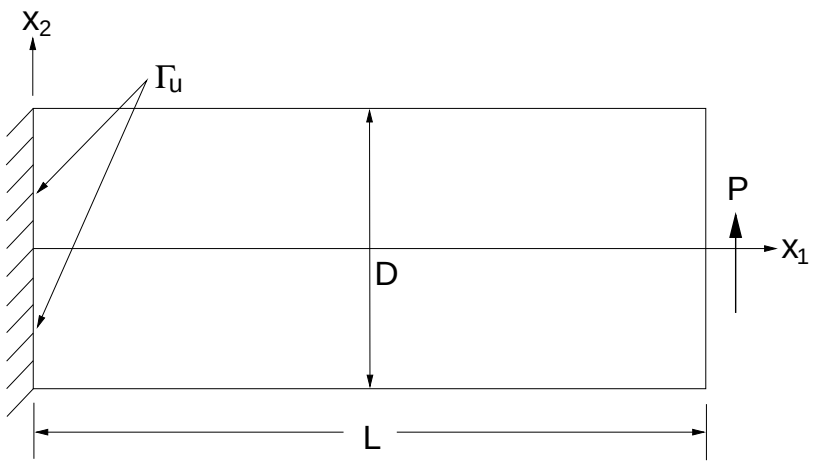

Figure 4.10: Cantilever beam model.

In the numerical model, the analytical displacement solution from Eq. (4.28) is prescribed on the boundary Γ_u: $x_1 = 0$, $-D/2 \leq x_2 \leq D/2$ (Fig. 4.10). On the remaining boundaries, exact tractions are specified. The following parameters are used in the numerical computations: $P = -1000$ lb, $D = 1$ in., $L = 4$ in., and plane stress conditions are assumed.

Convergence studies are carried out using four different nodal discretizations, namely 85 nodes, 297 nodes, 1105 nodes, and 1701 nodes. Equal nodal spacing in the x_1- and x_2-direction is used in each of the above grids. In Fig. 4.11, a sample nodal discretization (85 nodes) is shown. The $L^2(\Omega)$ and energy error norms are calculated on the basis of Eqs. (4.22a) and (4.24), respectively. In Fig. 4.12, the relative displacement and energy error norms are plotted against the nodal spacing h on a log-log plot. The rate of convergence is indicated by the value of R. The convergence rate for NEM is close to the theoretical rate for finite elements, namely $R = 2$ and $R = 1$ for displacements and strains, respectively. The absolute accuracy of NEM is observed to be better than that of the finite element solution.

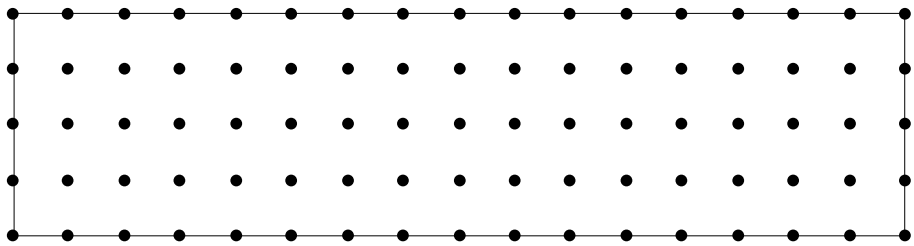

Figure 4.11: Nodal discretization for cantilever beam model (85 nodes).

The NEM and analytical stress fields are compared near the mid-line ($x = 2.03$ in.) of the beam. Since the shape function algorithm chosen here fails for points along $x = 2$ in. (Delaunay edges), such a choice is necessitated. In Fig. 4.13, the normal and shear stresses at $x = 2.03$ in. are plotted as a function of y. The nodal grid consisting of 1105 nodes is used, and the stress outputs are carried out at 200 equi-distant points between $y = -0.5$ in. and $y = 0.5$ in. The NEM and the analytical solution are in good agreement. The maximum error in the normal stress σ_{11} is less than 1%, and the shear stress profile also matches the analytical solution well.

4.4.5 Hollow Cylinder under Internal Pressure

Consider a hollow cylinder of internal and external radius of a and b, respectively. A A uniform pressure p_i is applied to the inner surface ($r = a$), while the outer surface ($r = b$) is traction-free. A schematic of the model problem is shown in Fig. 4.14. Due to axi-symmetry, the stresses are independent of θ, and hence only have a radial dependence. The exact solution for the stress components in polar coordinates (r, θ)

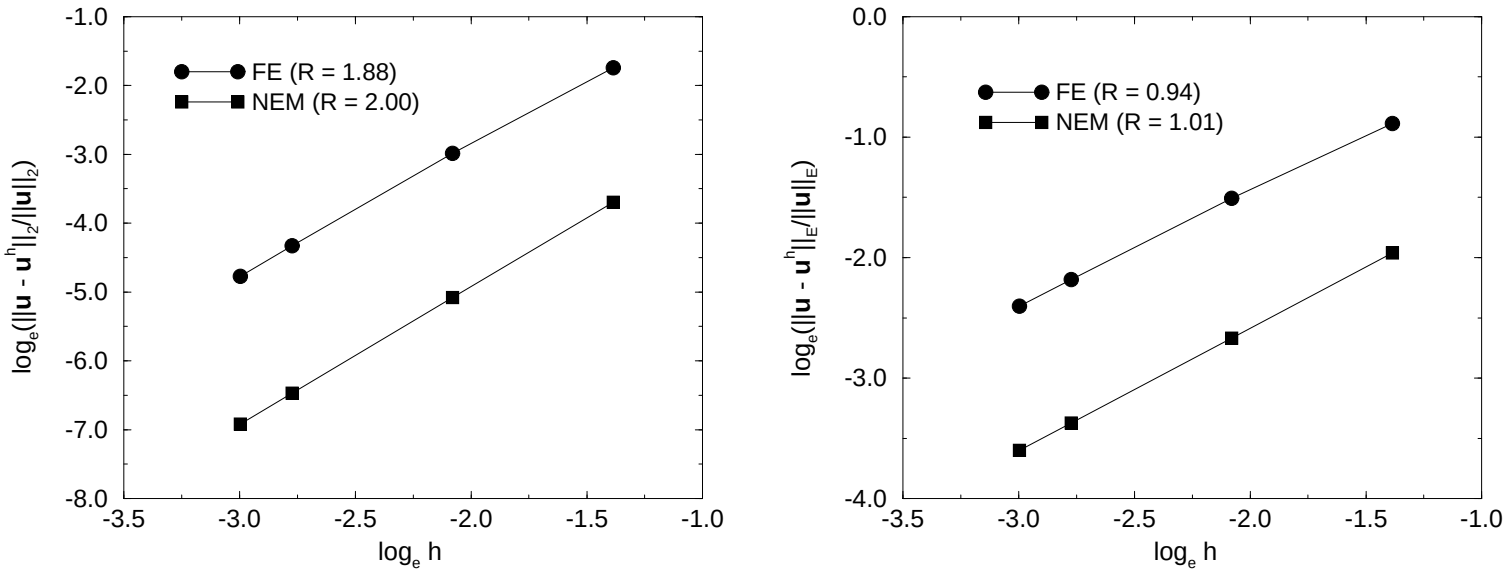

(a) (b)

Figure 4.12: Rate of convergence for the cantilever beam problem. (a) Displacement, and (b) Energy.

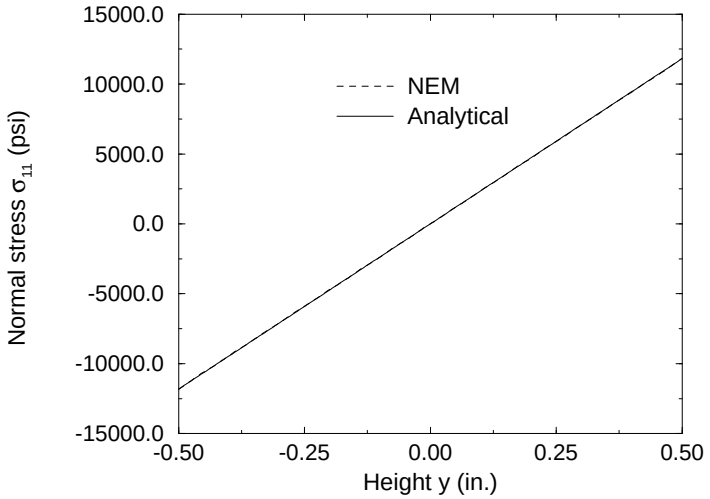

(a)

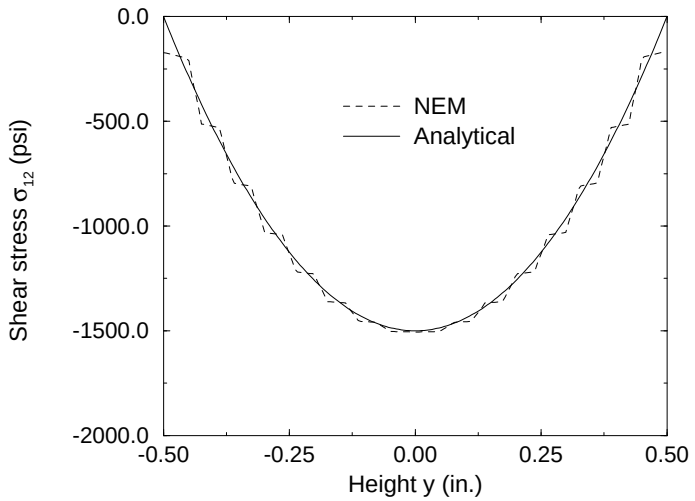

(b)

Figure 4.13: Comparison of NEM and analytical stresses for the cantilever beam model. (a) Normal stress σ_{11}, and (b) Shear stress σ_{12}.

is (Timoshenko and Goodier, 1970):

$$\sigma_r(r) = \frac{a^2 p_i}{b^2 - a^2}\left(1 - \frac{b^2}{r^2}\right), \tag{4.31a}$$

$$\sigma_\theta(r) = \frac{a^2 p_i}{b^2 - a^2}\left(1 + \frac{b^2}{r^2}\right), \tag{4.31b}$$

$$\sigma_{r\theta} = 0. \tag{4.31c}$$

Under plane stress conditions, the components of the small strain tensor are

$$\varepsilon_r(r) = \frac{a^2 p_i}{E(b^2 - a^2)}\left\{1 - \nu - \frac{b^2}{r^2}(1+\nu)\right\}, \tag{4.32a}$$

$$\varepsilon_\theta(r) = \frac{a^2 p_i}{E(b^2 - a^2)}\left\{1 - \nu + \frac{b^2}{r^2}(1+\nu)\right\}, \tag{4.32b}$$

$$\varepsilon_{r\theta} = 0, \tag{4.32c}$$

while the radial and tangential displacements are given by

$$u_r(r) = \frac{a^2 p_i r}{E(b^2 - a^2)}\left\{1 - \nu + \frac{b^2}{r^2}(1+\nu)\right\}, \tag{4.33a}$$

$$u_\theta = 0. \tag{4.33b}$$

In the numerical computations, the following parameters are chosen: $a = 1$ in., $b = 5$ in., $p_i = 3 \times 10^4$ psi, and plane stress conditions are assumed. Due to symmetry, only one-quarter of the specimen is modeled. In the analyses, six different nodal discretizations are considered, namely, 169 nodes, 361 nodes, 625 nodes, 1369 nodes, 1849 nodes, and 2401 nodes. In Fig. 4.15, the nodal grids for 169 and 625 nodes are illustrated. A convergence study is carried out using the above six nodal

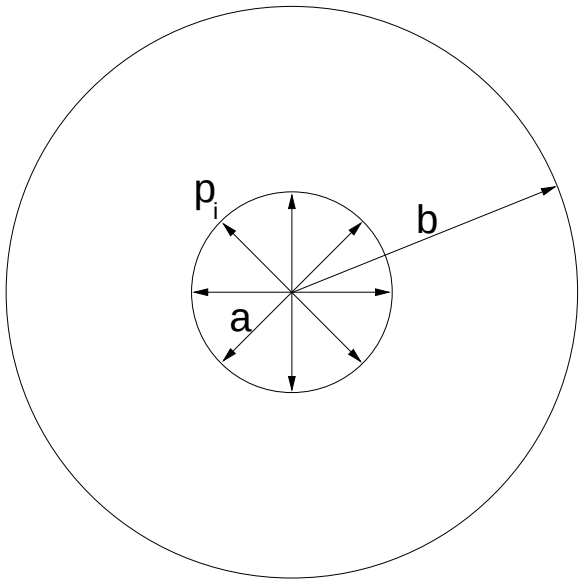

Figure 4.14: Hollow cylinder under internal pressure p_i.

discretizations. The exact $L^2(\Omega)$ and energy norms are given by

$$\|\mathbf{u}\|_{L^2(\Omega)} = \alpha\sqrt{\frac{\pi}{2}}\sqrt{\frac{(1-\nu)^2(b^4-a^4)}{4} + (1-\nu^2)b^2(b^2-a^2) + b^4(1+\nu)^2\log\frac{b}{a}}, \quad (4.34a)$$

$$\|\mathbf{u}\|_{E(\Omega)} = \alpha\sqrt{\frac{\pi E}{4}}\sqrt{(1-\nu)(b^2-a^2) + b^4(1+\nu)\left(\frac{1}{a^2}-\frac{1}{b^2}\right)}, \quad (4.34b)$$

where

$$\alpha = \frac{a^2 p_i}{E(b^2-a^2)}. \quad (4.34c)$$

For the specimen dimensions, internal pressure p_i, and material properties that are considered here, $\|\mathbf{u}\|_{L^2(\Omega)} = 2.462 \times 10^{-3}$ in^2 and $\|\mathbf{u}\|_{E(\Omega)} = 5.605\ \sqrt{\text{psi-in}^2}$. In Fig. 4.16, the convergence rate (R) in displacement and energy are presented for NEM and constant strain finite elements. The trends are similar to that observed in

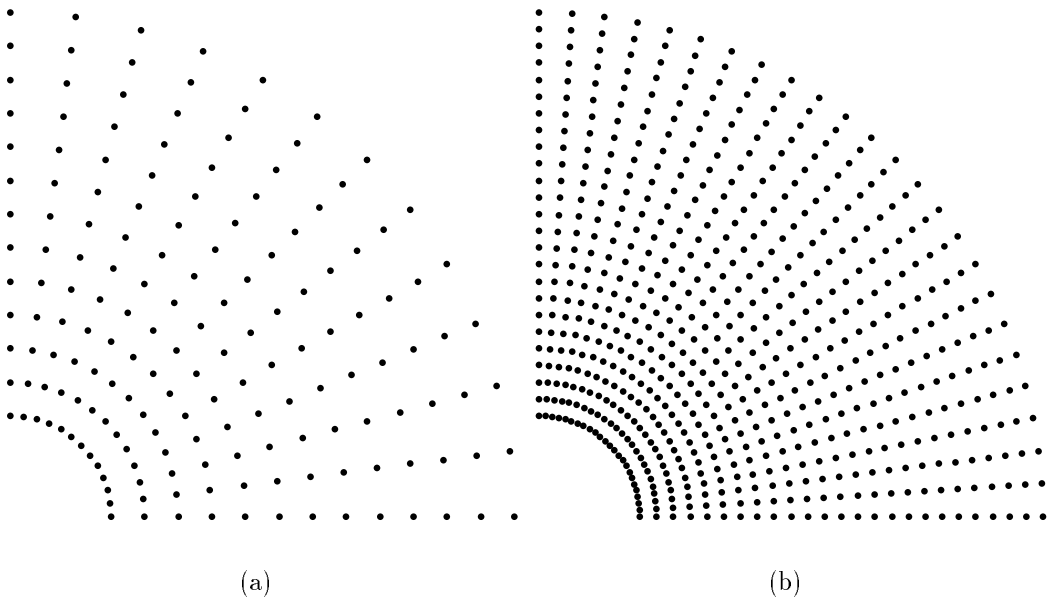

Figure 4.15: Sample nodal discretizations for the hollow cylinder under internal pressure problem. (a) 169 nodes, and (b) 625 nodes.

the earlier examples, with similar rates for NEM and FE, with NEM showing better absolute accuracy in displacements and strains.

A comparison of the NEM and exact stress fields is carried out using the grid consisting of 1369 nodes. The numerical solution recovered the rotational symmetry of the solution, and hence for the purpose of comparison, we plot the stresses along a radial line ($\theta = 30°$). In Fig. 4.17, the NEM and exact solutions for the radial stress and the hoop stress are presented. In the computations, 180 equi-distant output points between $r = 1$ in. and $r = 5$ in. are considered. The NEM and exact stress fields are in good agreement. Since the NEM displacement field is C^0 at the nodes, the numerical stresses are oscillatory. However, the oscillations are bounded, and they fluctuate about the exact solution, which is analogous to the finite element method,

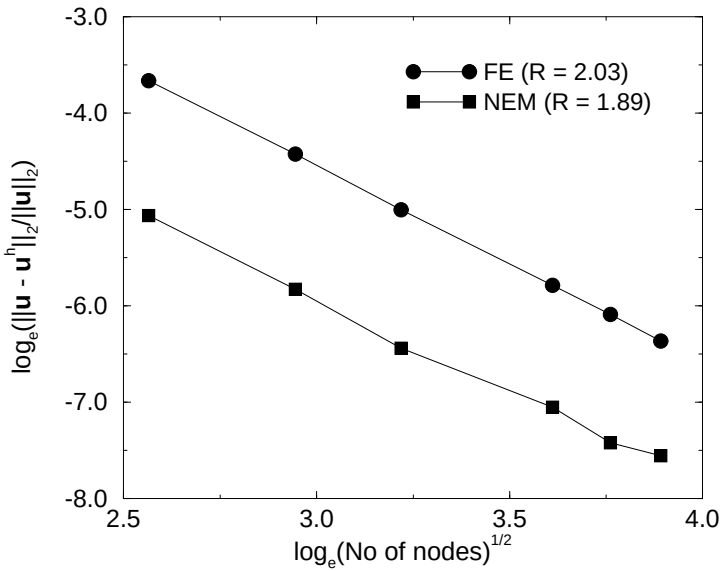

(a)

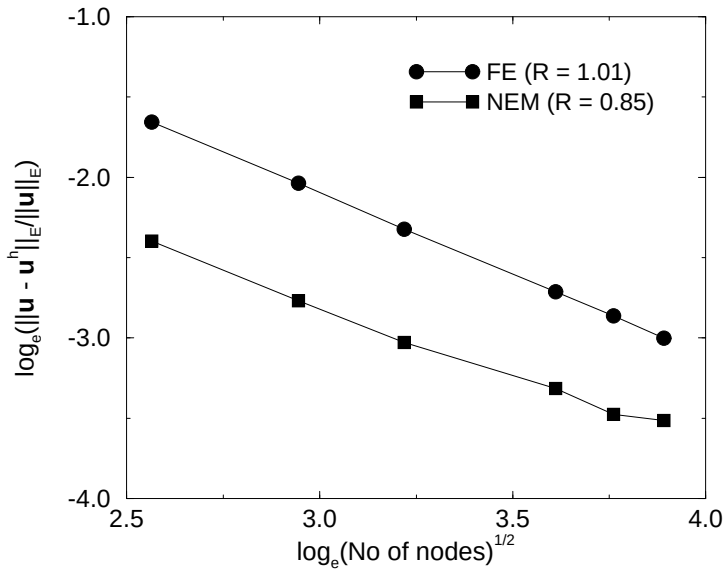

(b)

Figure 4.16: Rate of convergence for the hollow cylinder under internal pressure problem. (a) Displacement, and (b) Energy.

where the stresses are discontinuous across element boundaries.

4.4.6 Infinite Plate with an Inclusion

We consider the problem of an inclusion (α-phase) with a constant eigenstrain $\boldsymbol{\varepsilon}^*_\alpha$ in an infinite matrix (β-phase). In Fig. 4.18, a graphical representation of the problem is illustrated. The exact displacement vector solution in polar coordinates is given by (Mura, 1987)

$$u_r(r) = \begin{cases} C_1 r & r \leq R, \\ C_1 \dfrac{R^2}{r} & r \geq R, \end{cases} \tag{4.35a}$$

$$u_\theta = 0, \tag{4.35b}$$

where

$$C_1 = \frac{(\mu^\alpha + \lambda^\alpha)\bar{\varepsilon}^*_\alpha}{\mu^\alpha + \lambda^\alpha + \mu^\beta}. \tag{4.36}$$

In the above equation, μ and λ are the Lamé constants of the respective phases, while the eigenstrain $\bar{\varepsilon}^*_\alpha$ is a constant dilatational strain. The material properties used in the numerical computation are (Cordes and Moran, 1996): $\lambda^\alpha = 497.16$, $\mu^\alpha = 390.63$ in the α-phase, while the constants in the β-phase are $\lambda^\beta = 656.79$, $\mu^\beta = 338.35$. These correspond to $E^\alpha = 1000$, $\nu^\alpha = 0.28$, $E^\beta = 900$, and $\nu^\beta = 0.33$. A constant dilatational eigenstrain $\bar{\varepsilon}^*_\alpha = 0.01$ is assumed in the analysis, and the associated eigenstrain tensor is $\boldsymbol{\varepsilon}^*_\alpha = \bar{\varepsilon}^*_\alpha(\mathbf{e}_1\mathbf{e}_1 + \mathbf{e}_2\mathbf{e}_2)$.

The numerical model (quarter symmetry) is shown in Fig. 4.19, where the nodal

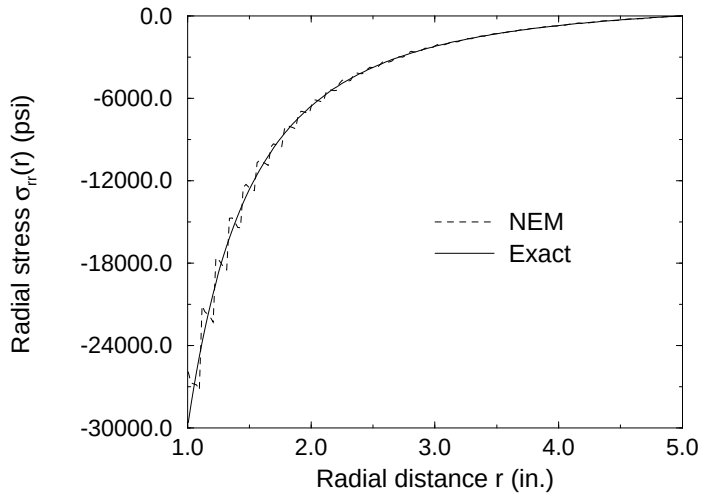

(a)

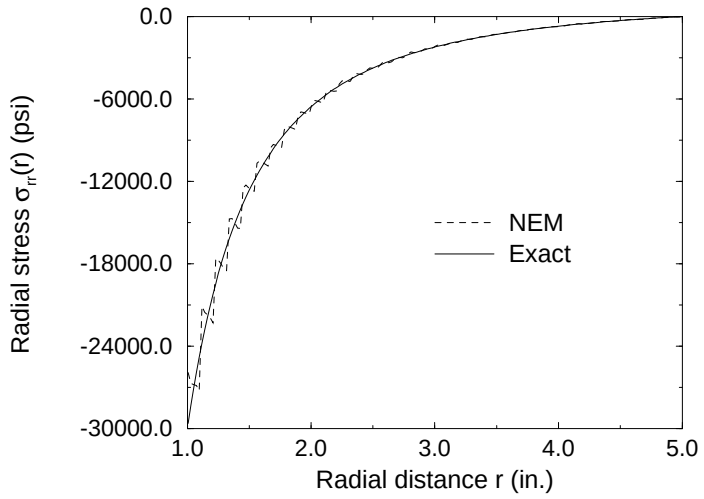

(b)

Figure 4.17: Comparison of the radial and hoop stresses for the hollow cylinder under internal pressure problem. (a) Radial stress $\sigma_{rr}(r)$, and (b) Hoop stress $\sigma_{\theta\theta}(r)$.

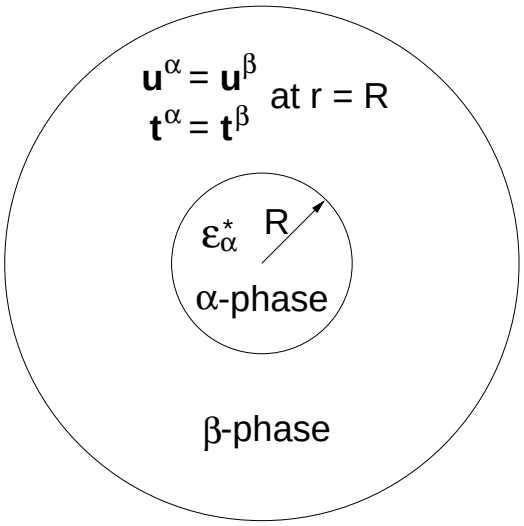

Figure 4.18: Inclusion embedded in an infinite matrix.

discretization consists of 647 nodes, with 114 nodes in the inclusion, 520 nodes in the matrix, and 13 nodes along the interface $r = R$. The outer radius $R_0 = 200$ is sufficiently large in comparison to the radius of the inclusion $R = 5$, so as to adequately represent the infinite matrix. Essential boundary conditions are imposed along the lines of symmetry, while the outer radius $R_0 = 200$ is traction-free. Plane strain conditions are assumed in the numerical computations. The NEM solution recovered the cylindrical symmetry in the solution, and hence results are presented as a function of only the radial distance. The maximum error in the numerically computed tangential displacement u_θ and shear stress $\sigma_{r\theta}$ are $\mathcal{O}(10^{-5})$ and $\mathcal{O}(10^{-4})$, respectively. In Fig. 4.20, a comparison of the NEM and exact solution is presented. The results shown in Fig. 4.20 are computed along a radial line ($r = 0$ to $r = 100$) at $\theta = 30°$. Along the radial line, 30 equi-spaced output points are chosen within the inclusion, and 150 equi-spaced points in the matrix. Excellent agreement between the NEM and the analytical solution is observed. The slight discrepancy in $u_r(r)$

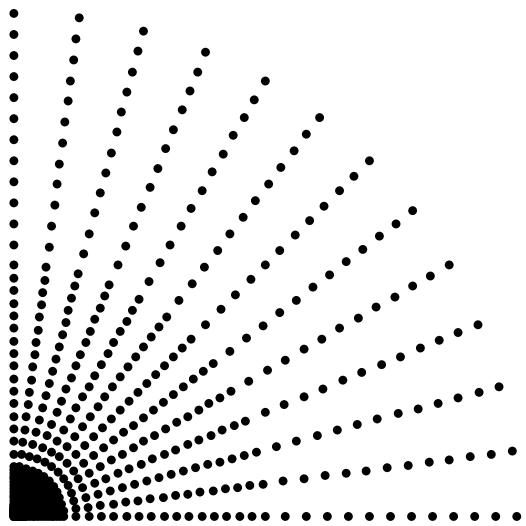

(a)

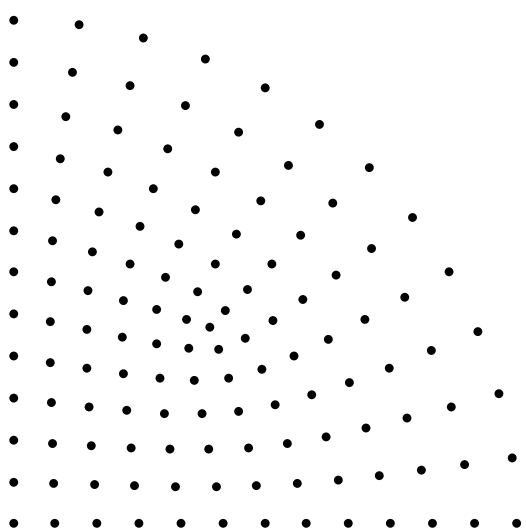

(b)

Figure 4.19: Nodal discretization for inclusion in an infinite matrix problem. (a) Quarter model, (b) Inclusion (α phase).

at $r > 25$ is due to the finite-dimension of the matrix as opposed to the theoretical solution which is based on an infinite matrix. The strains as well as the stresses are in good agreement with the exact solution. The oscillations in the radial and hoop strains are negligible; they are, however, a bit more pronounced in the stress solutions.

4.4.7 Edge-Cracked Plate under Tension

An edge-cracked plate under pure mode I loading is considered. Due to symmetry, only the upper-half is modeled. In Fig. 4.21a, the specimen dimensions and loading are indicated; the crack length a is half of the plate width w. Since the domain is convex, no modifications are required in the implementation of NEM. The mode I stress intensity factors (SIFs) are computed using the domain integral (Moran and Shih, 1987) form of the contour J-integral.

Three different nodal discretizations are considered: a regular grid consisting of 99 nodes shown in Fig. 4.21a and irregular grids of 278 and 2678 nodes with focused array of nodes in the vicinity of the crack-tip (Figs. 4.21b and 4.21c). In Fig. 4.21b, the minimum nodal spacing is $0.006a$, and for the nodal discretization shown in Fig. 4.21c, the minimum nodal spacing is $0.0014a$. In Table 4.4, the normalized mode I stress intensity factors for the three grids are presented. The reference solution for this edge-crack problem is: $K_I^{ref}/\sigma\sqrt{\pi a} = 2.8264$ (Tada, Paris, and Irwin, 1977). From Table 4.4, it is seen that the SIFs computed using NEM are more accurate than the corresponding values evaluated by constant strain finite elements. Domain independence is also clearly observed for the NEM results. The SIFs obtained using NEM for the refined grid (Fig. 4.21c) are within 0.3% of the reference solution results. The

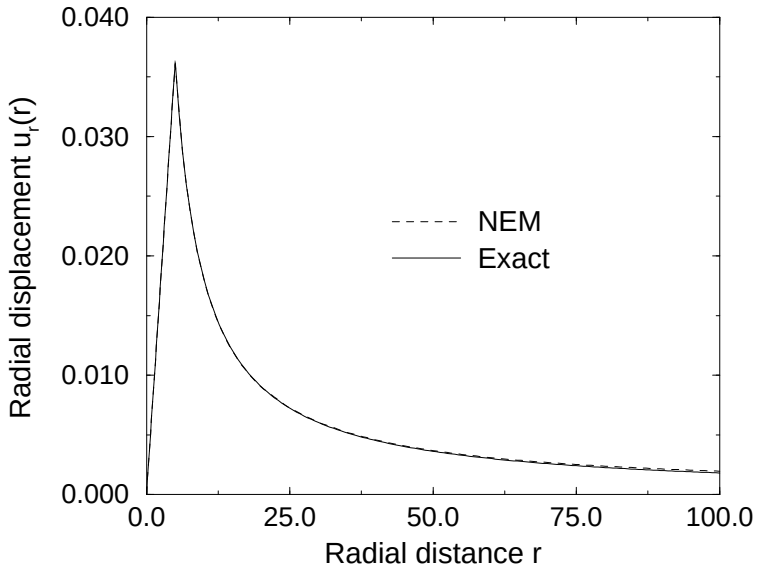
0.040
0.030
0.020
0.010
0.000
Radial displacement $u_r(r)$
NEM
Exact
0.0
25.0
50.0
75.0
100.0
Radial distance r

(a)

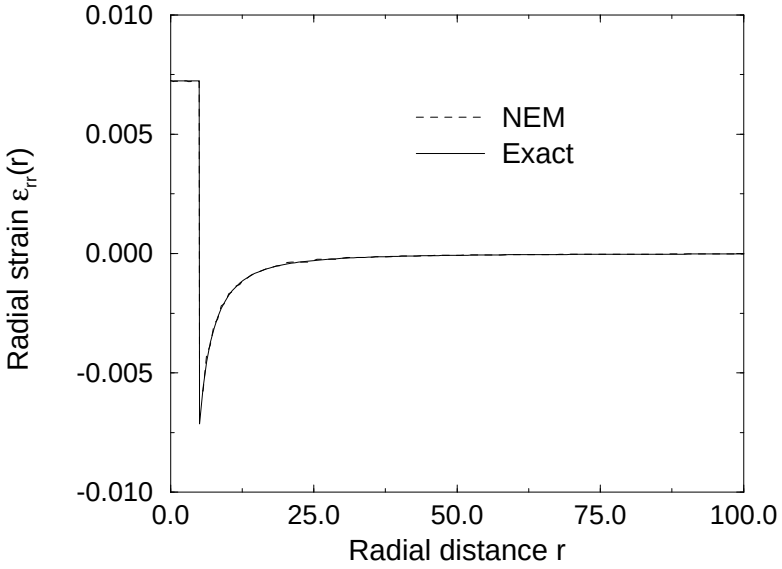
0.010
0.005
0.000
-0.005
-0.010
Radial strain $\varepsilon_{rr}(r)$
NEM
Exact
0.0
25.0
50.0
75.0
100.0
Radial distance r

(b)

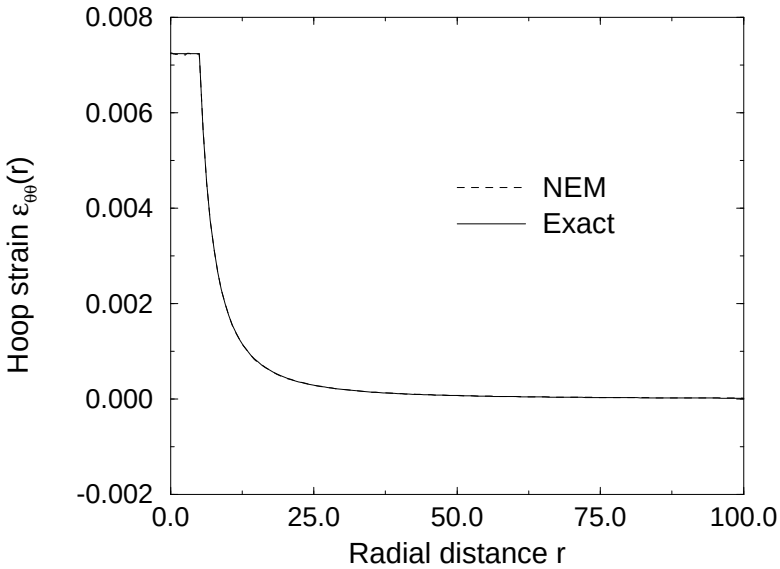
0.008
0.006
0.004
0.002
0.000
-0.002
Hoop strain $\varepsilon_{\theta\theta}(r)$
NEM
Exact
0.0
25.0
50.0
75.0
100.0
Radial distance r

(c)

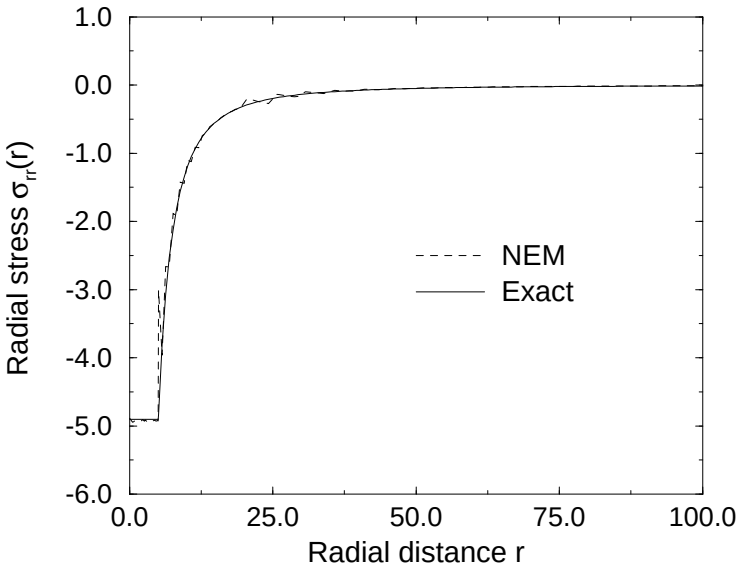
1.0
0.0
-1.0
-2.0
-3.0
-4.0
-5.0
-6.0
Radial stress $\sigma_{rr}(r)$
NEM
Exact
0.0
25.0
50.0
75.0
100.0
Radial distance r

(d)

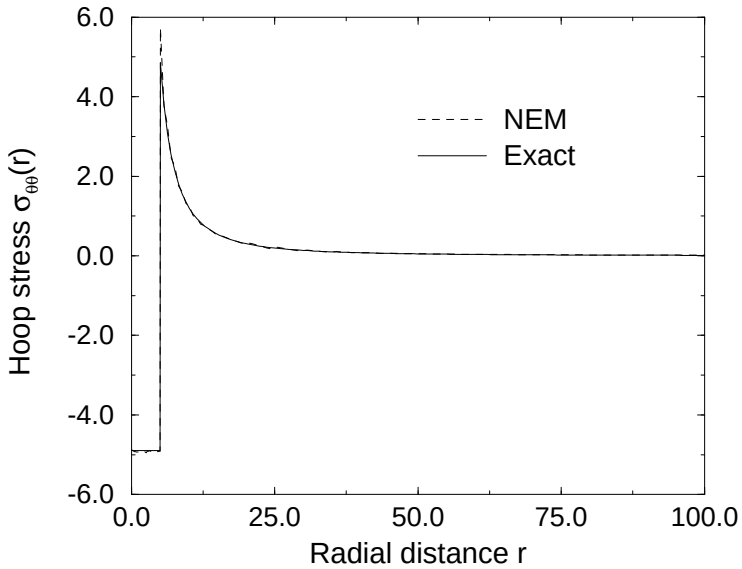

(e)

Figure 4.20: Comparison of NEM and the exact solution for an inclusion with a dilatational eigenstrain in an infinite matrix. (a) Radial displacement $u_r(r)$, (b) Radial strain $\varepsilon_{rr}(r)$, (c) Hoop strain $\varepsilon_{\theta\theta}(r)$, (d) Radial stress $\sigma_{rr}(r)$, and (e) Hoop stress $\sigma_{\theta\theta}(r)$.

domain independence of the SIFs using NEM and the excellent agreement with the reference solution results are encouraging and promising indicators for the application of NEM to SIF evaluation for 2D crack problems.

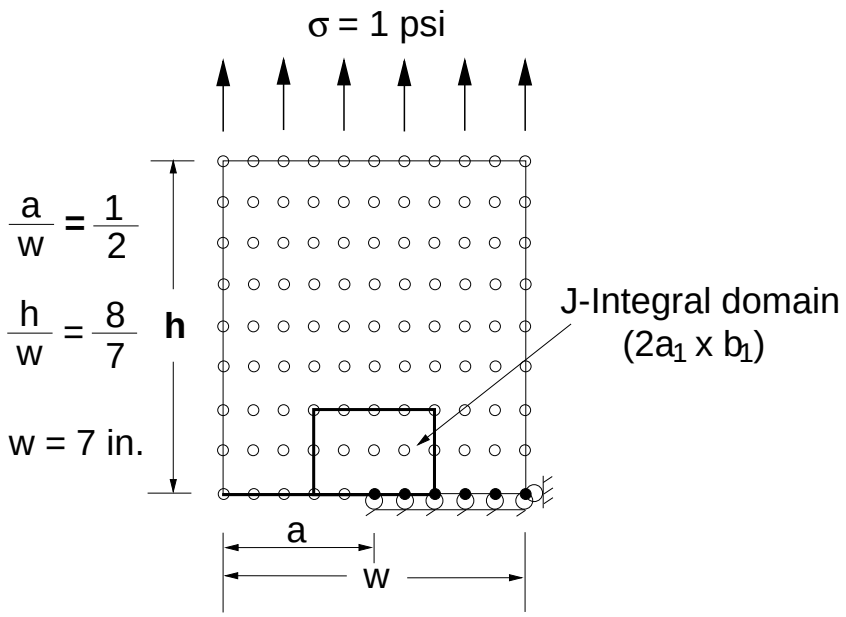

(a)

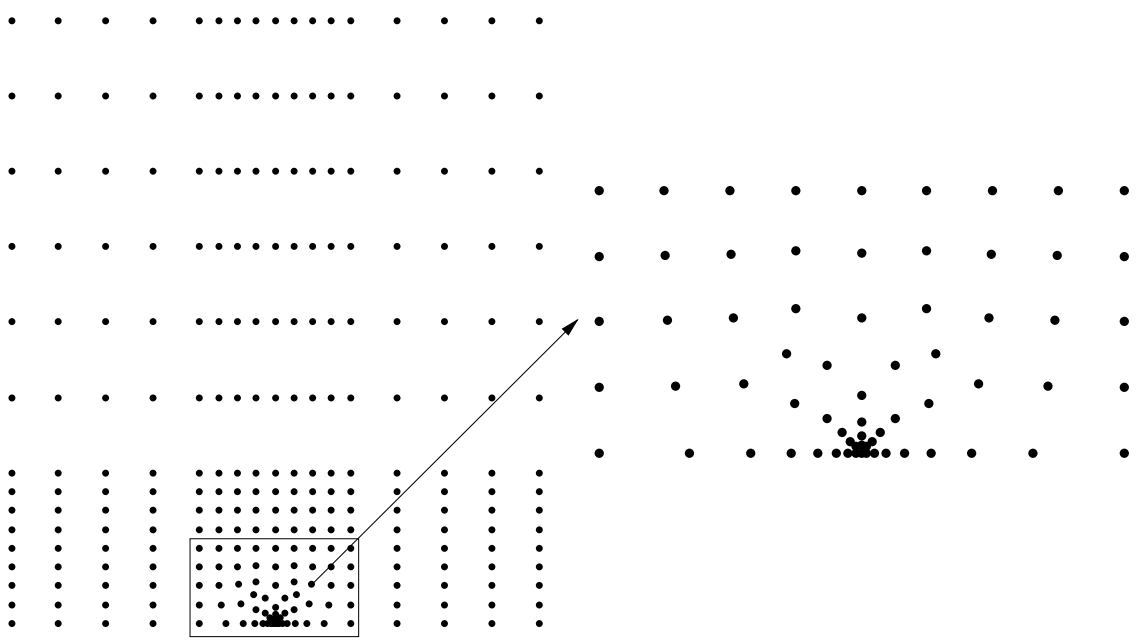

(b)

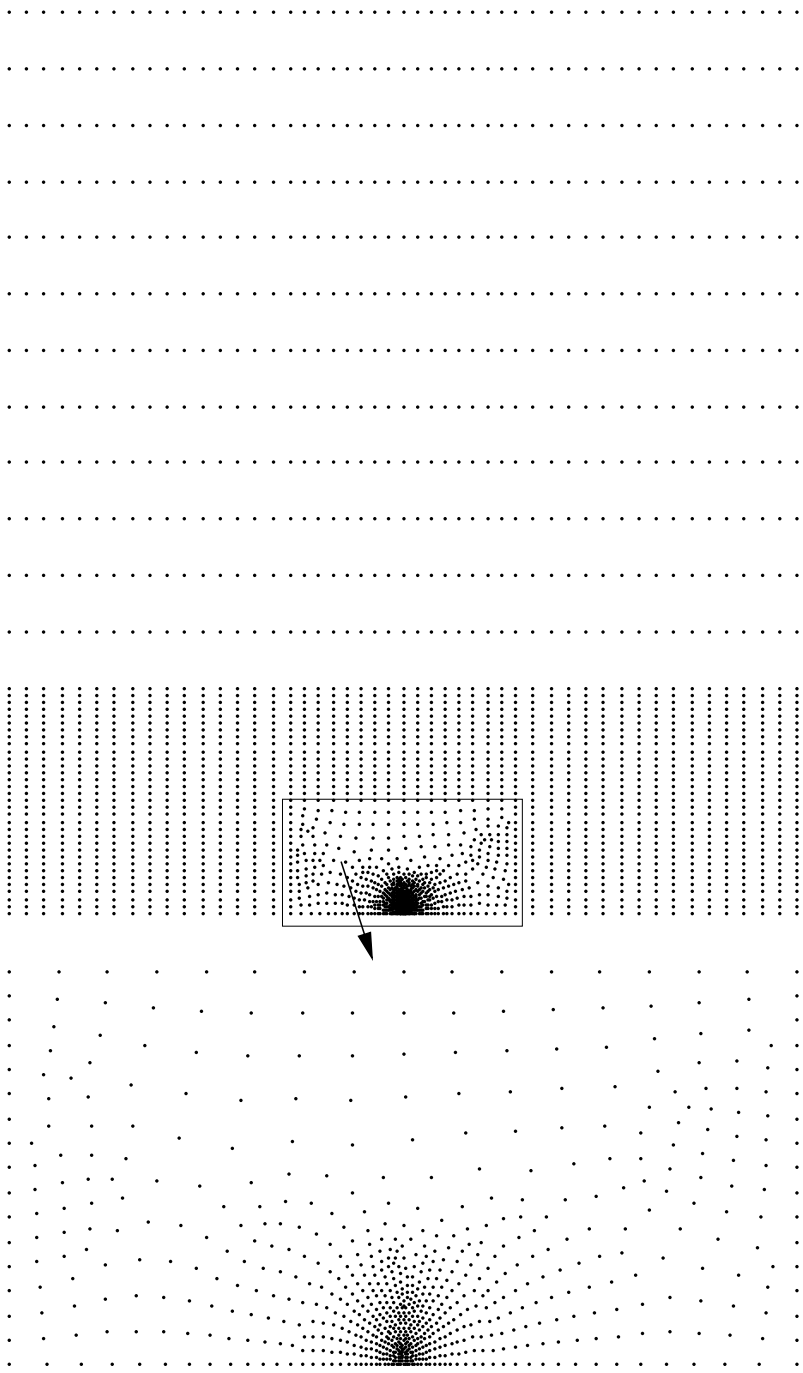

(c)

Figure 4.21: Edge-cracked plate under tension. (a) Regular grid (99 nodes), (b) Refined grid (278 nodes), and (c) Refined grid (2678 nodes)

Table 4.4: Normalized K_I: Edge-cracked plate under tension.

Nodal Grid	Domains a_1	Domains b_1	$\frac{K_I}{\sigma\sqrt{\pi a}}$ [NEM]	% Error	$\frac{K_I}{\sigma\sqrt{\pi a}}$ [FE]	% Error
Regular (99 nodes)	2.8	3.0	2.5241	10.7	2.1159	25.1
	2.8	5.0	2.5360	10.3	2.1691	23.3
	3.5	5.0	2.5310	10.5	2.1664	23.3
	3.5	6.0	2.5339	10.4	2.1806	22.8
	3.5	8.0	2.5375	10.2	2.1989	22.2
Refined (278 nodes)	1.0	2.0	2.7867	1.4	2.6567	6.0
	1.0	4.0	2.7893	1.3	2.6569	6.0
	1.0	6.0	2.7905	1.3	2.6586	5.9
	1.0	8.0	2.7911	1.2	2.6597	5.9
	3.5	8.0	2.7867	1.4	2.6752	5.3
Refined (2678 nodes)	1.0	2.0	2.8188	0.27	2.8052	0.75
	1.0	4.0	2.8188	0.27	2.8047	0.77
	1.0	6.0	2.8189	0.27	2.8049	0.76
	1.0	8.0	2.8188	0.27	2.8051	0.75
	3.5	8.0	2.8188	0.27	2.8051	0.75

Chapter 5

C^1 Natural Neighbor Interpolant for the Biharmonic Equation

In this Chapter, we present the computational implementation of a C^1 natural neighbor interpolant for the solution of PDEs. Farin (1990b) constructed a C^1 interpolant by embedding Sibson's natural neighbor coordinates in the Bernstein-Bézier surface representation of a cubic simplex. The C^1 interpolant for NEM that we propose is based on a transformation of Farin's interpolant, and as a result, interpolation to both, nodal function and nodal gradient values, is realized. This renders the C^1 NEM interpolant amenable to use in a Galerkin scheme for the solution of fourth-order elliptic PDEs.

We first present a brief overview on C^1 interpolants for the solution of higher-order PDEs. In Section 5.2, an outline of Farin's C^1 natural neighbor interpolant is presented, and then the methodology used to derive the C^1 NEM shape functions is described. The construction, properties, and numerical computations of the C^1 NEM shape functions are discussed in detail. In Section 5.4, the governing equations for the biharmonic equation together with the Galerkin formulation for NEM are described. In Section 5.5, numerical results for the biharmonic equation with Dirichlet boundary

conditions are presented.

5.1 Background

The ability to develop C^1 interpolants over an arbitrary bounded domain Ω is a much researched and far from trivial task. The higher-order smoothness or continuity requirement of interpolants is of interest since such classes of trial functions are necessary in a Galerkin formulation for the solution of higher-order elliptic partial differential equations (PDEs)—C^1 trial functions for the biharmonic (fourth-order) equation, with Kirchhoff plate bending in elasticity being a notable application and a case in point. In a general framework, C^1 continuity on the primary variable is required when the balance laws of a continuum can be cast in variational form and second-order derivatives of the primary variable appear in the variational statement. For example, in the problem of nucleation of a solid-solid phase transformation based on an energy functional that is dependent on the strain and strain gradients, the Galerkin implementation requires C^1-continuous trial functions (Chu and Moran, 1995).

In the realm of finite elements, one of the first C^1 interpolants developed was the Clough-Tocher finite element (Clough and Tocher, 1965; Strang and Fix, 1973), and in subsequent years many of its variants have emerged (Alfeld, 1984; Farin, 1985). Some of the other early developments in conforming triangular finite elements are due to de Veubeke (1968), Irons (1969), Bell (1969), and Powell and Sabin (1977). The construction of finite elements with C^1-continuity is in general unwieldy with significant complexity arising in the construction of the interpolant; moreover, the need to include first-order and second-order derivatives as additional nodal degrees of free-

dom tends to adversely affect the numerical solution. A general overview of the finite element interpolation problem for minimally C^1-continuous polynomial interpolants is presented by Peano (1979). Local C^k ($k > 0$) interpolants on a regular grid are readily constructed using splines. For irregularly-spaced data, an attractive choice for constructing C^k functions is to use C^k weight functions that have compact support; for example Shepard's interpolant (Shepard, 1968) or moving least squares (MLS) approximants (Lancaster and Salkauskas, 1981). These approaches lend themselves readily to curve and surface data fitting. In the application of MLS approximants to PDEs, however, certain issues do pose problems; for example, the non-interpolating property of MLS approximants leads to complications in the imposition of Dirichlet boundary conditions in a Galerkin scheme for the biharmonic equation (Hein, 1993; Krysl and Belytschko, 1996). Moreover, the numerical solution is sensitive to both the weight function, and its radius of support. A partial resolution to the above shortcomings is met by using smooth interpolating trial functions, as evidenced by the work of Donning (1997) in which cardinal splines are used in a displacement-based Galerkin scheme to solve shear-deformable thick as well as thin beam and plate problems using Mindlin-Reissner theory.

5.2 C^1 Natural Neighbor Interpolant

Farin (1990b) has proposed a C^1 interpolant based on Sibson's original C^0 natural neighbor interpolant. By embedding Sibson's coordinate in the Bernstein-Bézier representation of a cubic simplex, a C^1 interpolant is realized. Bernstein-Bézier patches and related concepts are widely used in the area of surface approximation and in the

field of computer-aided geometric design (Farin, 1990a). A review article on triangular Bernstein-Bézier surfaces can be found in Farin (1986), and a general treatment of multivariate polynomials over multi-dimensional simplices is given by de Boor (1987).

In what follows, multi-index notation denoted by the bold characters $\mathbf{i}$ and $\mathbf{j}$ is used (see Section 2.1.1) In the context of what follows, we let $\mathbf{i} = (i_1, i_2, \ldots, i_n)$ be a multi-index with norm $|\mathbf{i}| = i_1 + i_2 + \ldots + i_n$ (Farin, 1990a). Let $\boldsymbol{\xi} = (\xi_1, \xi_2, \ldots, \xi_n)$, with the property $\sum_I \xi_I = 1$, be the barycentric coordinate of a simplex $\delta \in \mathbb{R}^{n-1}$. A Bernstein-Bézier surface of degree m over the simplex δ can be written in the form (de Boor, 1987)

$$b(\boldsymbol{\xi}) = \sum_{|\mathbf{i}|=m} B^m_{\mathbf{i}}(\boldsymbol{\xi}) b_{\mathbf{i}}, \tag{5.1}$$

where $b_{\mathbf{i}}$ is known as the Bézier ordinate associated with the control point $\mathbf{i}/m$. The control net of $b(\boldsymbol{\xi})$ is the network of $(n+1)$-dimensional points $(\mathbf{i}/m, b_{\mathbf{i}})$. In Eq. (5.1), $B^m_{\mathbf{i}}(\boldsymbol{\xi})$ are m-variate Bernstein polynomials in n variables. To elaborate, they are the terms in the multinomial expansion of unity, i.e.,

$$(\xi_1 + \xi_2 + \cdots + \xi_n)^m = \sum_{|\mathbf{i}|=m} B^m_{\mathbf{i}}(\boldsymbol{\xi}), \qquad B^m_{\mathbf{i}}(\boldsymbol{\xi}) = \binom{m}{\mathbf{i}} \xi_1^{i_1} \xi_2^{i_2} \ldots \xi_n^{i_n}, \tag{5.2}$$

where $\binom{m}{\mathbf{i}}$ is the multinomial coefficient which is defined as

$$\binom{m}{\mathbf{i}} = \frac{m!}{i_1! \, i_2! \, \ldots i_n!}. \tag{5.3}$$

In one-dimension with $n = 2$, we have $\xi_1 = 1 - x$ and $\xi_2 = x$ as the barycentric coordinates of a simplex $\delta \in \mathbb{R}$. The univariate linear Bernstein polynomials ($m = 1$)

are $\{1-x,\ x\}$; the quadratic polynomials ($m = 2$) are $\{(1-x)^2,\ 2(1-x)x,\ x^2\}$; and the cubic polynomials ($m = 3$) are $\{(1-x)^3,\ 3(1-x)^2x,\ 3(1-x)x^2,\ x^3\}$, where $x \in [0,\ 1]$. Multivariate Bernstein polynomials have properties very much like their univariate counterparts. From Eq. (5.2), some of the important properties of multivariate Bernstein polynomials such as partition of unity, positivity, and cardinal interpolation, are easily inferred. The control points (circles) and associated Bézier ordinate values ($b_{\mathbf{i}}$) for a cubic Bernstein-Bézier triangular patch are shown in Fig. 5.1. The interested reader can refer to Böhm, Farin, and Kahmann (1984), Farin (1986), and Farin (1990a) for further details on the properties and applications of triangular Bernstein-Bézier patches.

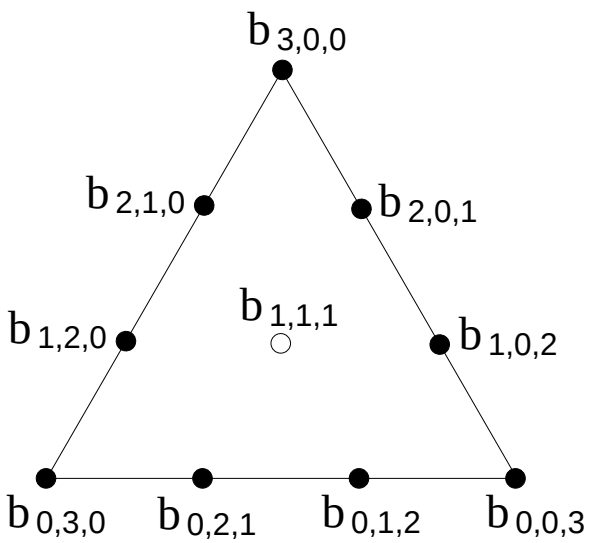

Figure 5.1: Cubic Bernstein-Bézier triangular patch.

Consider a point $\mathbf{x} \in \Omega \subset \mathbb{R}^2$ that has n natural neighbors. Let the natural neighbor coordinates of $\mathbf{x}$ be $\mathbf{\Phi} : \Omega \to \mathbb{R}^n$, where $\mathbf{\Phi} = \big(\phi_1(\mathbf{x}),\ \phi_2(\mathbf{x}), \ldots,\ \phi_n(\mathbf{x})\big)$. Since $\sum_I \phi_I(\mathbf{x}) = 1$, we note that $\mathbf{\Phi}$ can be considered as a barycentric coordinate

(non-unique) of the n-gon in the plane. The generalization of Bézier surfaces over a convex polygonal domain was proposed by Loop and DeRose (1989). By using $\mathbf{\Phi}$ instead of $\boldsymbol{\xi}$ in Eq. (5.1), we can construct the surface (Farin, 1990b)

$$w^m(\mathbf{\Phi}) = \sum_{|\mathbf{i}|=m} B^m_{\mathbf{i}}(\mathbf{\Phi}) b_{\mathbf{i}}. \tag{5.4}$$

In the above equation, the Bézier ordinate $b_{\mathbf{i}}$ is associated with the control point $\mathbf{q}_{\mathbf{i}} \in \mathbb{R}^2$, where $\mathbf{q}_{\mathbf{i}}$ are the projection of the control points of the m-variate Bézier polynomial over the $(n-1)$-dimensional simplex onto the plane (Farin, 1990b):

$$\mathbf{q}_{\mathbf{i}} = \sum_{|\mathbf{j}|=1} B^1_{\mathbf{j}}(\mathbf{i}/m)\mathbf{x}_{\mathbf{j}}, \qquad |\mathbf{i}| = m. \tag{5.5}$$

On the basis of Eq. (5.5), one can infer that the components of the barycentric coordinate $\boldsymbol{\xi}$ of the $(n-1)$-dimensional simplex is identical to that of the Sibson coordinate $\mathbf{\Phi}$ of the mapped n-gon on the plane.

The connectivity rule for Bézier simplexes states that the domain simplex has all vertices connected to all other vertices. If $\mathbf{q}_{\mathbf{i}}$ and $\mathbf{q}_{\mathbf{j}}$ are two Bézier points in the n-gon simplex, then the rule indicates that there must exist integers r and s such that the multi-indices $\mathbf{i}$ and $\mathbf{j}$ satisfy

$$\mathbf{i} - \mathbf{e}_r = \mathbf{j} - \mathbf{e}_s, \tag{5.6}$$

where $\mathbf{e}_\alpha = (\delta_{1\alpha}, \delta_{2\alpha}, \ldots, \delta_{k\alpha}, \ldots, \delta_{n\alpha})$ denotes the multi-index having zero in all components except for the αth component, which is one. The projection of the control net of a cubic tetrahedron ($m = 3,\ n = 4$) onto the plane is shown in Fig. 5.2.

In Fig. 5.2, the open circles are "boundary" control points, and the filled circles are center control points. The center control points are located at the centroid of the corresponding triangle; for instance, $\mathbf{q}_{1,1,1,0} = \frac{1}{3}(\mathbf{q}_{3,0,0,0} + \mathbf{q}_{0,3,0,0} + \mathbf{q}_{0,0,3,0})$.

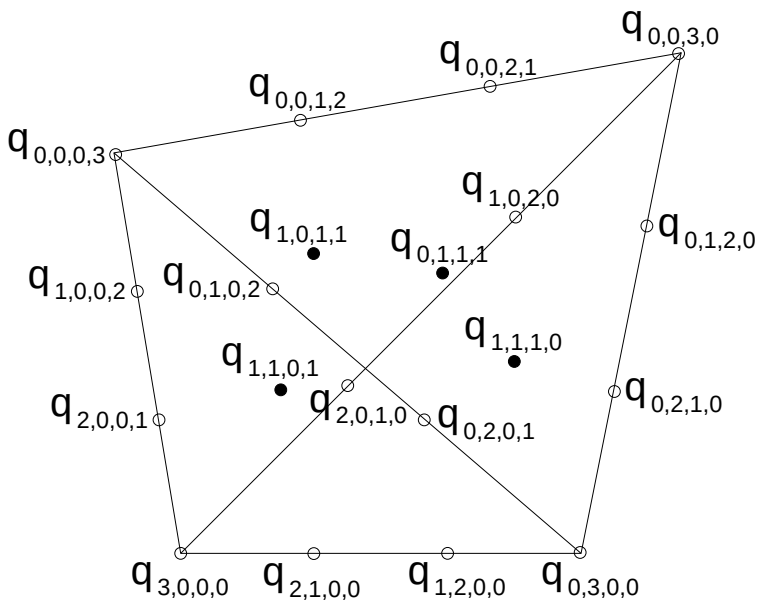

Figure 5.2: Projection of the control net of a cubic tetrahedron onto the plane (Farin, 1990b).

If we choose $m = 1$ in Eq. (5.4) and let $w_I = w(\mathbf{x}_I)$ denote the nodal function value, we obtain

$$w^1(\mathbf{x}) = \sum_{I=1}^{n} \phi_1^{\delta_{1I}}(\mathbf{x})\phi_2^{\delta_{2I}}(\mathbf{x}) \ldots \phi_n^{\delta_{nI}}(\mathbf{x}) b_{\mathbf{e}_I} = \sum_{I=1}^{n} \phi_I(\mathbf{x}) w_I \tag{5.7}$$

which is the original Sibson interpolant. Hence, Eq. (5.4) can be viewed as a generalized form of the Sibson interpolant.

For $m = 3$, we arrive at the following surface representation (Farin, 1990b):

$$w^3(\mathbf{\Phi}) = \sum_{|\mathbf{i}|=3} B^3_{\mathbf{i}}(\mathbf{\Phi}) b_{\mathbf{i}}, \tag{5.8}$$

which is the C^1 interpolant that we use in the natural element method.

5.2.1 Properties

Farin (1990b) has outlined the properties of the C^1 interpolant given in Eq. (5.8). Here we discuss some of the important properties that are germane to a Galerkin formulation that is pursued in this work.

Smoothness Farin (1990b) has shown that the interpolant proposed in Eq. (5.8) is $C^1(\Omega)$. Consider an open bounded domain $\Omega \subset \mathbb{R}^2$. Let $\mathbf{x} \in \Omega$ be any point that has n natural neighbors, and $\mathbf{x}_I$ be the nodal coordinate of node I ($I = 1, n$). Sibson coordinates $\phi_I(\mathbf{x})$ are continuously differentiable at all points $\mathbf{x} \neq \mathbf{x}_I$. Since $B^3_{\mathbf{i}}$ in Eq. (5.8) is composed of products of $C^0(\Omega)$ natural neighbor shape functions raised to a power, it is evident that the new interpolant is also continuously differentiable at all points $\mathbf{x} \neq \mathbf{x}_I$. The "boundary" control points for the n-gon with respect to node I lie along the lines joining $\mathbf{x}_I$ and the remaining $n-1$ nodes. Let these $n-1$ directions be denoted by d_j ($j = 1, n-1$). The control points in the tangent plane with respect to node I are the ones that lie along d_j and are connected to the control point $\mathbf{q}_{3\mathbf{e}_I}$ (node I)—see Eq. (5.6). Farin (1990b) noted that the directional derivative at $\mathbf{x}_I$ along an arbitrary direction d is a linear combination of the directional derivatives along the directions d_j. Moreover, since all the control points are coplanar, the directional

derivative along d is also in the plane, and hence the differentiability at $\mathbf{x} = \mathbf{x}_I$ is met. By virtue of the above inferences, the $C^1(\Omega)$ continuity of the interpolant is established.

Quadratic Completeness The $C^1(\Omega)$ interpolant has quadratic completeness, i.e., it can exactly reproduce a general quadratic function (Farin, 1990b). As opposed to the above, the $C^1(\Omega)$ interpolant proposed by Sibson (1981) can reproduce only spherical quadratics, i.e., functions of the form $a_0 + a_1 x + a_2 y + a_3(x^2 + y^2)$. By virtue of the quadratic completeness property, Farin's $C^1(\Omega)$ interpolant can exactly represent a state of constant curvature (second derivatives of the displacement for the thin plate problem) which is required in order to pass the patch test for a fourth-order PDE such as the biharmonic equation.

By judicious choice of the Bézier ordinates, Farin (1983) realized a quadratic precision interpolant. For a cubic n-gon simplex in the plane, there are $n^2 + \binom{n}{3}$ control points, and consequently the same number of Bézier ordinates. Of these, n^2 control points lie along the lines joining nodes $\mathbf{x}_I$ and $\mathbf{x}_J$ $(I < J \leq n)$, with four control points lying along any one such line. For instance, if $I = 1$, $J = 3$, and $n = 4$, the control points along the line joining $\mathbf{x}_1$ and $\mathbf{x}_3$ are $\mathbf{q}_{3,0,0,0}$, $\mathbf{q}_{2,0,1,0}$, $\mathbf{q}_{1,0,2,0}$, and $\mathbf{q}_{0,0,3,0}$. The associated "boundary" Bézier ordinates to these n^2 control points are of two distinct types, namely ordinates $b_{\mathbf{i}}$ whose subscript contains one 3 and all other zeros (for e.g., $b_{0,3,0,0}$), or ordinates $b_{\mathbf{i}}$ whose subscript have one 2, one 1, and all other zeros (for e.g., $b_{1,2,0,0}$). The former (nodal or vertex ordinates) are precisely equal to the nodal function value, and the latter Bézier ordinates are easily found in the tangent planes (see Section 5.3.2). The additional $\binom{n}{3}$ control points are

associated with "free" Bézier ordinates $b_{\mathbf{i}}$ whose subscript contains three 1's and all other zeros (for e.g., $b_{1,1,1,0}$). The Bézier ordinates mentioned within braces are for $n = 4$; the control points for this case are indicated in Fig. 5.2. An optimal choice for the center Bézier ordinate is given by $b_{1,1,1,0} = \frac{3}{2}a - \frac{1}{2}c$ (Farin, 1983), where a is the centroid of the tangent Bézier ordinates and c is the centroid of the vertex (nodal) Bézier ordinates. The above choice of the center Bézier ordinate guarantees quadratic precision. An illustration of the evaluation of the Bézier ordinates for a cubic Bernstein-Bézier triangular patch is shown in Fig. 5.3. Referring to Fig. 5.3, we can express $b_{1,1,1}$ as (Farin, 1983; Farin, 1990b)

$$b_{1,1,1} = \frac{3}{2}a - \frac{1}{2}c, \tag{5.9a}$$

where

$$a = \frac{b_{2,1,0} + b_{1,2,0} + b_{2,0,1} + b_{1,0,2} + b_{0,2,1} + b_{0,1,2}}{6}, \quad c = \frac{b_{3,0,0} + b_{0,3,0} + b_{0,0,3}}{3}. \tag{5.9b}$$

Interpolation in One-Dimension In one-dimension, the $C^0(\Omega)$ natural element method is identical to linear finite elements (see Section 3.3.6). We now consider the $C^1(\Omega)$ natural neighbor interpolant in one-dimension. Let $\Omega = (0, 1) \subset \mathbb{R}$ be an open bounded domain. Any point $x \in \Omega$ has two natural neighbors, but a point $x \in \partial\Omega$ has only one neighbor. Let $x \in \Omega$ be a point that has two natural neighbors at $x = 0$

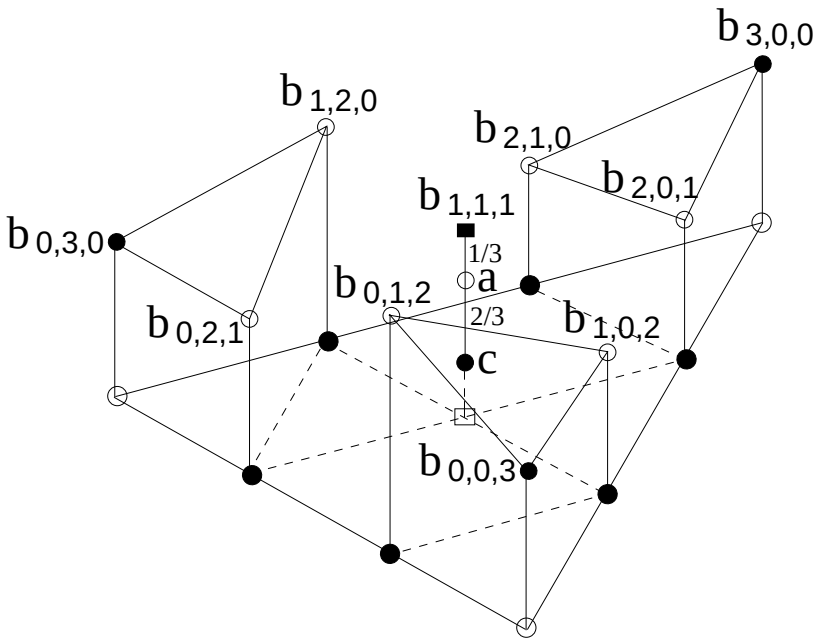

Figure 5.3: Evaluation of the Bézier ordinates for a cubic triangular surface patch (Böhm et al., 1984).

and $x = 1$. Then, Eq. (5.8) reduces to

$$w(\mathbf{\Phi}) = \sum_{i_1+i_2=3} \frac{3!}{i_1!\, i_2!} \phi_1^{i_1}(\mathbf{\Phi}) \phi_2^{i_2}(\mathbf{\Phi}) b_{i_1,i_2}. \tag{5.10}$$

Since $\phi_1 = 1 - x$ and $\phi_2 = x$ are the natural neighbor shape functions (barycentric coordinates) of the point x, we can expand the above equation to obtain

$$w(x) = (1-x)^3 b_{3,0} + 3(1-x)^2 x b_{2,1} + 3(1-x)x^2 b_{1,2} + x^3 b_{0,3} \tag{5.11}$$

which is a cubic polynomial curve between the two nodes. In the above equation, $b_{3,0} = w(0)$, $b_{0,3} = w(1)$, and $b_{2,1}$ and $b_{1,2}$ are related to the function values and their derivatives at $x = 0$ and $x = 1$, respectively.

Cubic polynomial along the boundary $\partial\Omega$ We assume that the discrete model consists of a set of nodes N that describes a convex domain $\Omega \subset \mathbb{R}^2$, with $\partial\Omega$ represented by the boundary of the convex hull $\mathrm{CH}(N)$. On the boundary of the convex hull, any point $\mathbf{x}$ has only two neighbors (Farin, 1990b). Consequently, by Eq. (5.11) in the previous sub-section, we immediately arrive at the result that cubic interpolation is realized along the boundary of the convex hull.

Interpolation in Two-Dimensions If a point $\mathbf{x} \in \Omega \subset \mathbb{R}^2$ has two natural neighbors ($n = 2$), the interpolant is cubic between the two nodes; if $n = 3$, the approximation is a cubic surface over a triangular patch; and for a regular rectangular nodal grid ($n = 4$), the approximation is a bicubic patch (Farin, 1990b).

5.2.2 NEM Trial Function

We use the interpolant presented in Eq. (5.8) as the $C^1(\Omega)$ NEM trial function. Let the point $\mathbf{x} \in \Omega \subset \mathbb{R}^2$ have n natural neighbors, with $\phi_I(\mathbf{x})$ the natural neighbor shape function of node I ($I = 1, n$). Consider an interpolation scheme for a scalar-valued function $w(\mathbf{x})$: $\Omega \subset \mathbb{R}^2 \to \mathbb{R}$, in the form:

$$w^h(\mathbf{\Phi}) = \sum_{|\mathbf{i}|=3} B^3_{\mathbf{i}}(\mathbf{\Phi}) b_{\mathbf{i}}, \tag{5.12}$$

where the dependence on position $\mathbf{x}$ is implicit since the components of $\mathbf{\Phi}$ are the natural neighbor shape functions that are functions of $\mathbf{x}$. We reiterate that there are $n^2 + \binom{n}{3}$ Bézier ordinates in Eq. (5.12), and consequently $n^2 + \binom{n}{3}$ terms on the right-hand side of the above equation.

The above form of the interpolant is suitable for applications in the context of data interpolation or surface approximation since nodal function values and sometimes even nodal gradient data are known *apriori*. For the numerical solution of PDEs by a Galerkin procedure, however, this is not the case since nodal function and nodal gradient values are unknowns, which are to be determined from the solution of the discrete system: $\mathbf{K}\,\mathbf{d} = \mathbf{f}$. To meet the desired goal, we suggest a transformation that renders the resulting interpolant amenable to numerical computations and implementation in the context of the numerical solution of PDEs. This is achieved by re-casting Eq. (5.12) in the following form (matrix notation):

$$w^h(\mathbf{\Phi}) = \{\mathbf{B}(\mathbf{\Phi})\}^T\{\mathbf{b}\} = \{\mathbf{B}(\mathbf{\Phi})\}^T[\mathbf{T}]\{\mathbf{w}\} = \{\mathbf{\Psi}(\mathbf{\Phi})\}^T\{\mathbf{w}\}, \tag{5.13a}$$

where

$$\{\mathbf{b}\} = [\mathbf{T}]\{\mathbf{w}\}, \quad \{\mathbf{\Psi}(\mathbf{\Phi})\}^T = \{\mathbf{B}(\mathbf{\Phi})\}^T[\mathbf{T}]. \tag{5.13b}$$

In Eq. (5.13), $\{\mathbf{B}\}$ and $\{\mathbf{b}\}$ are column vectors of dimension $n^2 + \binom{n}{3}$, and $[\mathbf{T}]$ is a transformation matrix of dimensions $(n^2 + \binom{n}{3}) \times 3n$. The transpose of the shape function vector $\{\mathbf{\Psi}(\mathbf{\Phi})\}^T = \{\psi_1(\mathbf{\Phi}), \psi_2(\mathbf{\Phi}), \psi_3(\mathbf{\Phi}), \ldots, \psi_{3n-2}(\mathbf{\Phi}), \psi_{3n-1}(\mathbf{\Phi}), \psi_{3n}(\mathbf{\Phi})\}$, and the transpose of the nodal vector $\{\mathbf{w}\}^T = \{w_1, \theta_{1x}, \theta_{1y}, \ldots, w_n, \theta_{nx}, \theta_{ny}\}$, where $w_I = w(\mathbf{x}_I)$ are the nodal function values, and $\theta_{Ix} = w_{,x}(\mathbf{x}_I)$ and $\theta_{Iy} = w_{,y}(\mathbf{x}_I)$ are the nodal gradient values. For the thin plate problem, w_I are the nodal displacements, and θ_{Ix} and θ_{Iy} are the nodal rotations. The matrix $[\mathbf{T}]$ is a transformation matrix that maps the nodal function and gradient values to the Bézier ordinates. The

transformation from $\{\mathbf{B}(\mathbf{\Phi})\} \rightarrow \{\mathbf{\Psi}(\mathbf{\Phi})\}$ that we propose in Eq. (5.13b) is based on a simple observation. In order to construct a $C^1(\Omega)$ surface over an unstructured nodal grid, in general the nodal function values and nodal gradient values are required. In the Bernstein-Bézier surface representation given in Eq. (5.12), the vertex Bézier ordinates are identical to the nodal function values, and the tangent and center Bézier ordinates are related to the nodal function and nodal gradient data. Hence in its current form, the local interpolant is dependent on coefficients ($\mathbf{b}$) that vary from point to point. The matrix $[\mathbf{T}]$ facilitates the representation of the interpolant in terms of nodal function values and nodal gradients, which renders it amenable to use in a PDE-setting; moreover, interpolation to both is realized (see Section 5.3.3). In light of the above, we can view the C^1 NEM interpolant as a bivariate generalization of one-dimensional Hermite cubic polynomials. In one-dimension, the equivalence of the NEM interpolant to cubic Hermite finite elements is shown in Section 5.3.2.

On constructing the transformation matrix $[\mathbf{T}]$ and carrying out the matrix-vector multiplication indicated in Eq. (5.13b), we can express the $C^1(\Omega)$ NEM trial function in standard shape function notation as:

$$w^h(\mathbf{x}) = \sum_{j=1}^{3n} \psi_j(\mathbf{x}) w_j, \tag{5.14}$$

where $\psi_{3I-2}(\mathbf{x})$, $\psi_{3I-1}(\mathbf{x})$, and $\psi_{3I}(\mathbf{x})$ are the shape functions for node I that are associated with the nodal degrees of freedom w_I, θ_{Ix}, and θ_{Iy}, respectively.

Support of C^1 Shape Functions Consider node $I \in N$, where N is the set consisting of n natural neighbors for a point $\mathbf{x} \in \Omega \subset \mathbb{R}^2$. The $C^1(\Omega)$ shape functions

associated with node I are $\psi_{3I-2}(\mathbf{x})$, $\psi_{3I-1}(\mathbf{x})$, and $\psi_{3I}(\mathbf{x})$. These shape functions are derived from a Bernstein-Bézier surface representation, in which the natural neighbor shape functions are used as barycentric coordinates of a point $\mathbf{x}$. Consequently, the $C^1(\Omega)$ shape functions retain the compact support properties of $\phi_I(\mathbf{x})$, and hence a local interpolant is realized. Akin to $\phi_I(\mathbf{x})$, the support of the shape functions $\psi_{3I-2}(\mathbf{x})$, $\psi_{3I-1}(\mathbf{x})$, and $\psi_{3I}(\mathbf{x})$, are the intersection of the convex hull CH(N) with the union of all Delaunay circumcircles that pass through node I (Farin, 1990b). Consider a unit square discretized by 25 (5×5) equi-spaced nodes (Fig. 3.3a). The support for the shape functions $\phi_{3A-2}(\mathbf{x})$ and $\phi_{3A-1}(\mathbf{x})$ associated with node A are illustrated in Figs. 5.4a and 5.4b, respectively.

5.3 Numerical Computation of Shape Functions

In this section, we first present the expressions for Bernstein-Bézier basis functions as a function of Sibson's coordinate $\mathbf{\Phi}$. Then, we describe in detail the construction of the transformation matrix $[\mathbf{T}]$ and the subsequent evaluation of NEM shape functions. Lastly, some key properties of the newly developed $C^1(\Omega)$ NEM shape functions $\mathbf{\Psi}(\mathbf{\Phi})$ are presented.

5.3.1 Bernstein-Bézier Basis Functions

Bernstein-Bézier (BB) basis functions are defined in Eq. (5.2). For a cubic n-gon simplex in Sibson's coordinates, we obtain

$$B^3_{\mathbf{i}}(\mathbf{\Phi}) = \binom{3}{\mathbf{i}} \phi_1^{i_1} \phi_2^{i_2} \ldots \phi_n^{i_n}, \tag{5.15}$$

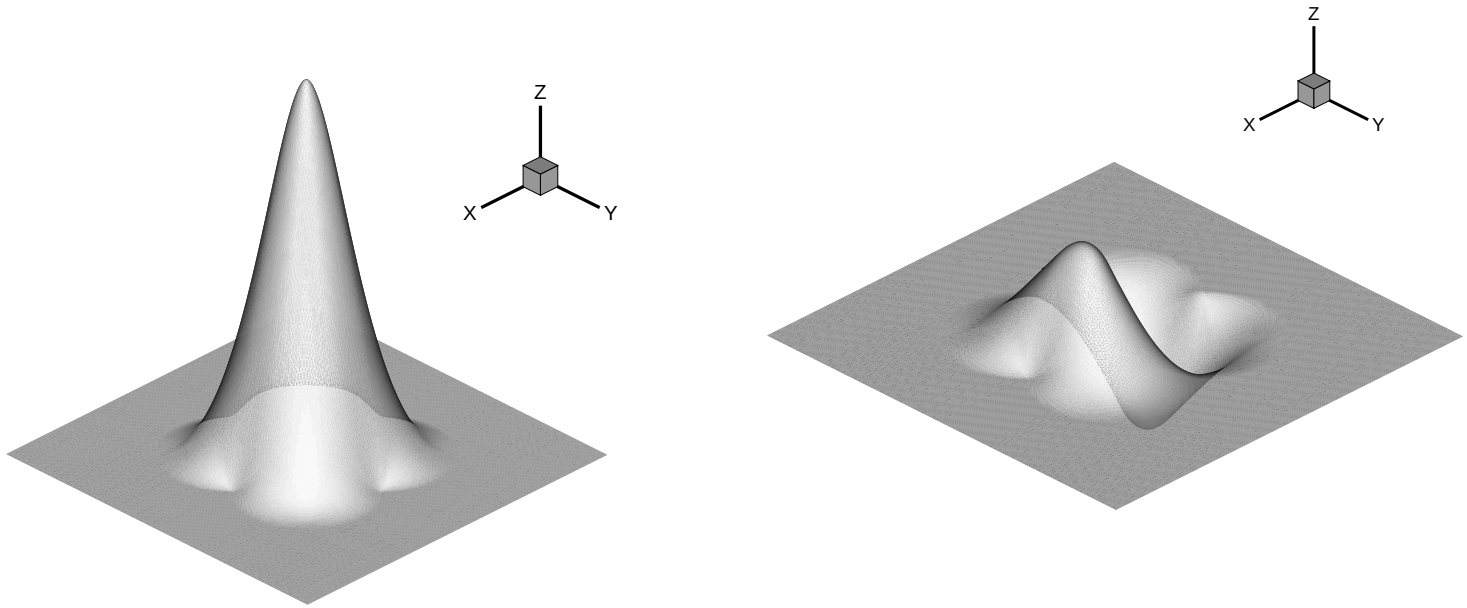

(a) (b)

Figure 5.4: Support for $C^1(\Omega)$ NEM shape function. (a) Shape function $\psi_{3A-2}(\mathbf{x})$, and (b) Shape function $\psi_{3A-1}(\mathbf{x})$.

where $\mathbf{i} = i_1 + i_2 + \cdots + i_n = 3$. For the cubic case, only three distinct types of basis functions arise, namely those corresponding to $\mathbf{i} = 3\mathbf{e}_I$, $\mathbf{i} = 2\mathbf{e}_I + \mathbf{e}_J$, and $\mathbf{i} = \mathbf{e}_I + \mathbf{e}_J + \mathbf{e}_K$. For convenience, we let $I \equiv 1$, $J \equiv 2$, and $K \equiv 3$. Then, the corresponding BB-basis functions are given by

$$B_{3,0,0}(\mathbf{x}) = \phi_1^3(\mathbf{x}), \quad B_{2,1,0}(\mathbf{x}) = 3\phi_1^2(\mathbf{x})\phi_2(\mathbf{x}), \quad B_{1,1,1}(\mathbf{x}) = 6\phi_1(\mathbf{x})\phi_2(\mathbf{x})\phi_3(\mathbf{x}). \tag{5.16}$$

By definition, the three basis functions can be represented in the form

$$B_{i_1,i_2,i_3}(\mathbf{x}) = \frac{3!}{i_1!\,i_2!\,i_3!}\phi_1^{i_1}(\mathbf{x})\phi_2^{i_2}(\mathbf{x})\phi_3^{i_3}(\mathbf{x}), \tag{5.17}$$

where the choices (3, 0, 0), (2, 1, 0), and (1, 1, 1) for the 3-tuple (i_1, i_2, i_3) lead to the equations indicated in Eq. (5.16). The first derivatives of $B_{i_1,i_2,i_3}(\mathbf{x})$ can now be written as

$$\frac{\partial B_{i_1,i_2,i_3}(\mathbf{x})}{\partial \alpha} = B_{i_1,i_2,i_3}(\mathbf{x})C_{i_1,i_2,i_3}(\mathbf{x}), \;\; C_{i_1,i_2,i_3}(\mathbf{x}) = \sum_{k=1}^{3} i_k \frac{\phi_{k,\alpha}(\mathbf{x})}{\phi_k(\mathbf{x})}, \;\; (\alpha = x,\, y), \tag{5.18}$$

and its second derivatives are given by

$$\frac{\partial^2 B_{i_1,i_2,i_3}(\mathbf{x})}{\partial\alpha\partial\beta} = \frac{\partial B_{i_1,i_2,i_3}(\mathbf{x})}{\partial\beta}C_{i_1,i_2,i_3}(\mathbf{x}) + B_{i_1,i_2,i_3}(\mathbf{x})\frac{\partial C_{i_1,i_2,i_3}(\mathbf{x})}{\partial\beta}, \tag{5.19a}$$

where

$$\frac{\partial C_{i_1,i_2,i_3}(\mathbf{x})}{\partial\beta} = \sum_{k=1}^{3} i_k \frac{\phi_k(\mathbf{x})\phi_{k,\alpha\beta}(\mathbf{x}) - \phi_{k,\alpha}(\mathbf{x})\phi_{k,\beta}(\mathbf{x})}{\phi_k^2(\mathbf{x})}, \quad (\alpha,\, \beta = x,\, y). \tag{5.19b}$$

From the viewpoint of theoretical exposition, the above expressions for the Bernstein-Bézier basis function derivatives are compact and appealing. Nevertheless, in the numerical implementation, the derivatives of the basis functions given in Eq. (5.16) are explicitly computed. By this approach, simplifications arise and one can group like terms together which leads to fewer arithmetic operations in the computations.

5.3.2 Construction of Transformation Matrix [T]

As can be inferred from Section 5.2.2, the construction of the transformation matrix $[\mathbf{T}]$ is the key step in transforming the Bernstein-Bézier representation of the trial function to the shape function form given in Eq. (5.14). Since this is central to the computational methodology that is adopted here, a detailed description of its formation is shown below.

We first present the relations between Bézier ordinates and the nodal function and gradient values, and then proceed to outline the structure and computational algorithm to construct the transformation matrix $[\mathbf{T}]$. The nodal or vertex Bézier ordinates are equal to the nodal function values, i.e.,

$$b_{\mathbf{i}} = w_I, \quad \mathbf{i} = 3\mathbf{e}_I \tag{5.20}$$

for the Bézier ordinate at node I. The tangent Bézier ordinates are related to the nodal function and nodal gradient values. Let d be the direction along the line $\mathbf{x}_I$ to $\mathbf{x}_J$ and $\hat{d}$ be that from $\mathbf{x}_J$ to $\mathbf{x}_I$. The directional derivative of the function $w(\mathbf{x})$

along the directions d and $\hat{d}$ are given by

$$\frac{\partial w(\mathbf{x})}{\partial d} = \boldsymbol{\nabla} w(\mathbf{x}) \cdot \mathbf{d} = \frac{\partial w(\mathbf{x})}{\partial x} d_x^{IJ} + \frac{\partial w(\mathbf{x})}{\partial y} d_y^{IJ}, \tag{5.21a}$$

$$\frac{\partial w(\mathbf{x})}{\partial \hat{d}} = \boldsymbol{\nabla} w(\mathbf{x}) \cdot \hat{\mathbf{d}} = -\left(\frac{\partial w(\mathbf{x})}{\partial x} d_x^{IJ} + \frac{\partial w(\mathbf{x})}{\partial y} d_y^{IJ} \right), \tag{5.21b}$$

where $\hat{\mathbf{d}} = -\mathbf{d}$, and $d_x^{IJ} = x_J - x_I$ and $d_y^{IJ} = y_J - y_I$ are the Cartesian components of the vector $\mathbf{d}$. The directional derivative at $\mathbf{x}_I$ along d and the directional derivative at $\mathbf{x}_J$ along $\hat{d}$ can be expressed as

$$\frac{\partial w(\mathbf{x}_I)}{\partial d} = \theta_{Ix} d_x^{IJ} + \theta_{Iy} d_y^{IJ}, \tag{5.22a}$$

$$\frac{\partial w(\mathbf{x}_J)}{\partial \hat{d}} = -\left(\theta_{Jx} d_x^{IJ} + \theta_{Jy} d_y^{IJ} \right). \tag{5.22b}$$

The tangent Bézier ordinates that lie in the tangent plane are determined through the relations (Farin, 1990a)

$$\frac{\partial w(\mathbf{x}_I)}{\partial d} = 3(b_{\mathbf{i}} - b_{\mathbf{j}}), \quad \mathbf{i} = 2\mathbf{e}_I + \mathbf{e}_J, \ \mathbf{j} = 3\mathbf{e}_I, \tag{5.23a}$$

$$\frac{\partial w(\mathbf{x}_J)}{\partial \hat{d}} = 3(b_{\mathbf{i}} - b_{\mathbf{j}}), \quad \mathbf{i} = \mathbf{e}_I + 2\mathbf{e}_J, \ \mathbf{j} = 3\mathbf{e}_J, \tag{5.23b}$$

which on using Eqs. (5.20) and (5.22) and re-arranging terms results in the following expressions for the tangent Bézier ordinates:

$$b_{2\mathbf{e}_I + \mathbf{e}_J} = \frac{1}{3} \left(\theta_{Ix} d_x^{IJ} + \theta_{Iy} d_y^{IJ} \right) + w_I, \tag{5.24a}$$

$$b_{\mathbf{e}_I + 2\mathbf{e}_J} = -\frac{1}{3} \left(\theta_{Jx} d_x^{IJ} + \theta_{Jy} d_y^{IJ} \right) + w_J. \tag{5.24b}$$

Now, the center Bézier ordinates are computed using Eq. (5.9). Consider the center ordinate $b_{\mathbf{i}}$ with subscript $\mathbf{i} = \mathbf{e}_I + \mathbf{e}_J + \mathbf{e}_K$, i.e., the corresponding control point lies at the centroid of triangle $(\mathbf{x}_I, \mathbf{x}_J, \mathbf{x}_K)$. Hence, on using Eqs. (5.20) and (5.24) in conjunction with Eq. (5.9), we obtain the following expression for the center ordinate:

$$b_{\mathbf{i}} = \frac{w_I + w_J + w_K}{3} + \frac{\alpha_I\theta_{Ix} + \beta_I\theta_{Iy} + \alpha_J\theta_{Jx} + \beta_J\theta_{Jy} + \alpha_K\theta_{Kx} + \beta_K\theta_{Ky}}{4}, \tag{5.25a}$$

$$\mathbf{i} = \mathbf{e}_I + \mathbf{e}_J + \mathbf{e}_K, \tag{5.25b}$$

where

$$\alpha_I = \frac{d_x^{IJ} + d_x^{IK}}{3}, \qquad \alpha_J = \frac{-d_x^{IJ} + d_x^{JK}}{3}, \qquad \alpha_K = \frac{-d_x^{IK} - d_x^{JK}}{3}, \tag{5.26a}$$

$$\beta_I = \frac{d_y^{IJ} + d_y^{IK}}{3}, \qquad \beta_J = \frac{-d_y^{IJ} + d_y^{JK}}{3}, \qquad \beta_K = \frac{-d_y^{IK} - d_y^{JK}}{3}, \tag{5.26b}$$

$$d_x^{IJ} = x_J - x_I, \qquad d_x^{IK} = x_K - x_I, \qquad d_x^{JK} = x_K - x_J, \tag{5.26c}$$

$$d_y^{IJ} = y_J - y_I, \qquad d_y^{IK} = y_K - y_I, \qquad d_y^{JK} = y_K - y_J. \tag{5.26d}$$

The storage structure for the transformation matrix $[\mathbf{T}]$ is shown in Fig. 5.5, and a pseudo-code for its construction is presented in Table 5.1. The map from the nodal function values to the vertex Bézier ordinates is stored in the first n rows; the next $n^2 - n$ rows pertain to the tangent Bézier ordinates; and the last block of $\binom{n}{3}$ rows relate the nodal function and gradient values to the center Bézier ordinates. In Fig. 5.6, the vertex, tangent, and center Bézier ordinates with respect to node 1 are indicated for a pentagonal simplex ($n = 5$). An outline of the algorithm presented in Table 5.1 follows. The matrix $[\mathbf{T}]$ as well as an $n \times n$ matrix $[\mathbf{R}]$ are initialized

to zero. The matrix $[\mathbf{R}]$ stores the row number of the contribution in $[\mathbf{T}]$ due to the tangent Bézier ordinates. For the first block of n rows, Eq. (5.20) is invoked so as to set the Ith row and $(3I-2)$-column position in $[\mathbf{T}]$ to unity. In the second block (tangent ordinates), the entries in $[\mathbf{T}]$ are evaluated using Eq. (5.24). The loops are executed such that for any node I $(1 \leq I \leq n-1)$, the entries for all tangent ordinates along the line joining $\mathbf{x}_I$ to $\mathbf{x}_J$ $(I < J \leq n)$ are computed. In Fig. 5.6, the filled square corresponds to the Bézier ordinate given by Eq. (5.24a), and the open square corresponds to that given by Eq. (5.24b). Lastly, the entries in the matrix $[\mathbf{T}]$ due to the center ordinates (see filled ellipses in Fig. 5.6) are stored. This involves the 3-tuple $(I,\, J,\, K)$ such that $1 \leq I \leq n-2$, $I < J \leq n-1$, and $J < K \leq n$. Here, the entries in $[\mathbf{T}]$ are computed using Eqs. (5.25) and (5.26). Both $[\mathbf{T}]$ as well as $[\mathbf{R}]$ are required to evaluate the parameters that appear in Eq. (5.26). In addition to storing the entries in $[\mathbf{T}]$, the BB-basis functions and its derivatives given in Section 5.3.1 are also computed within each block. Once the construction of the transformation matrix $[\mathbf{T}]$ is complete, a matrix-vector product is carried out to compute the shape functions $\psi_j(\mathbf{x})$ and their derivatives $\psi_{j,\alpha}(\mathbf{x})$ and $\psi_{j,\alpha\beta}(\mathbf{x})$ $(\alpha,\, \beta = x,\, y)$:

$$\{\mathbf{\Psi}(\mathbf{\Phi})\}^T = \{\mathbf{B}(\mathbf{\Phi})\}^T[\mathbf{T}], \tag{5.27a}$$

$$\{\mathbf{\Psi}_{,\alpha}(\mathbf{\Phi})\}^T = \{\mathbf{B}_{,\alpha}(\mathbf{\Phi})\}^T[\mathbf{T}], \tag{5.27b}$$

$$\{\mathbf{\Psi}_{,\alpha\beta}(\mathbf{\Phi})\}^T = \{\mathbf{B}_{,\alpha\beta}(\mathbf{\Phi})\}^T[\mathbf{T}]. \tag{5.27c}$$

In order to illustrate the shape function computations, we present two examples. First, in one-dimension, it is shown that the matrix $[\mathbf{T}]$ transforms cubic Bernstein polynomials to cubic Hermite polynomials that are used in higher-order

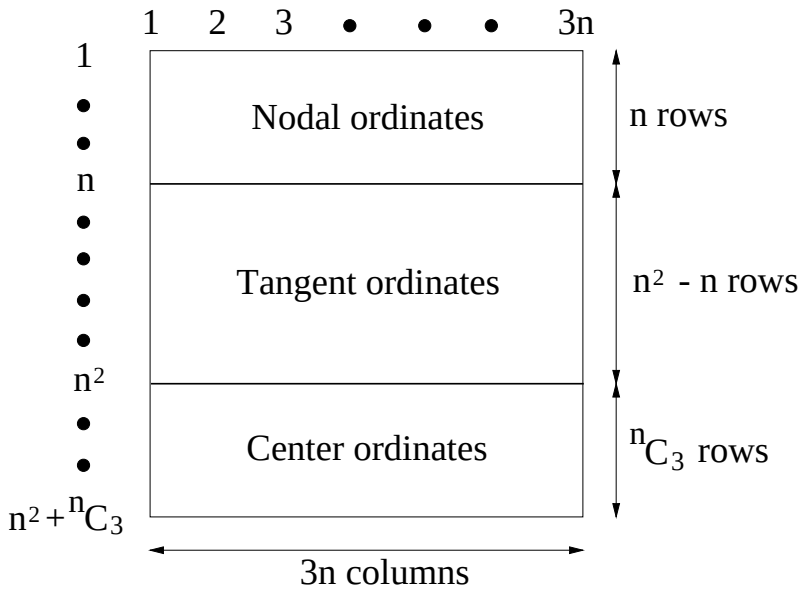

Figure 5.5: Storage structure for the transformation matrix [**T**].

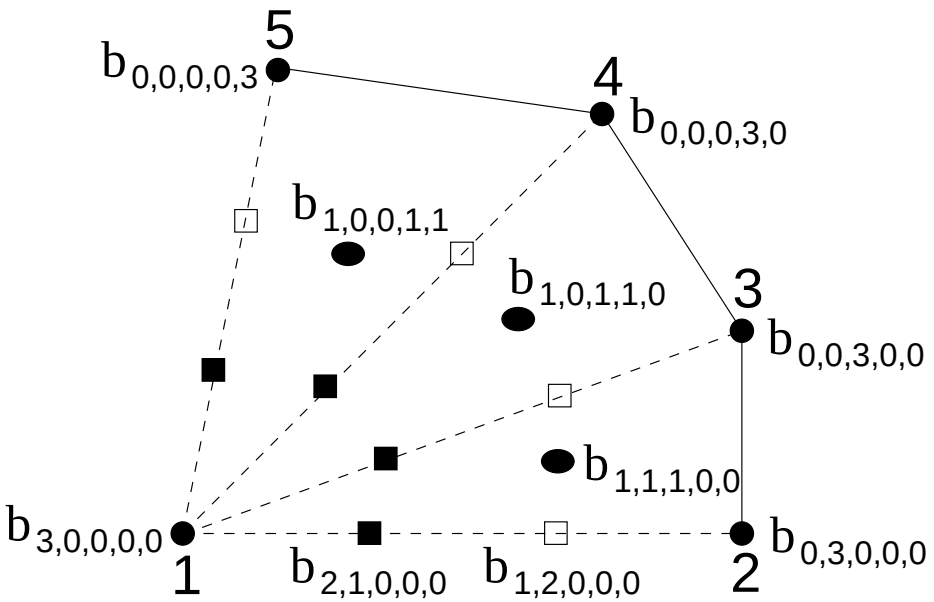

Figure 5.6: Bézier ordinates used in the algorithm for a pentagonal simplex.

1. Initialize matrix $[\mathbf{T}] = 0$;
2. Initialize matrix $[\mathbf{R}] = 0$;
3. for $I = 1 \rightarrow n$ {
   - T(I,3I − 2) = 1;

   }
4. row = n;
5. for $I = 1 \rightarrow n - 1$ {
   (a) for $J = I + 1 \rightarrow n$ {
      - row ← row + 1;
      - T(row,3I − 2) = 1; T(row,3I − 1) = $d_x^{IJ}/3$; T(row,3I) = $d_y^{IJ}/3$;
      - R(I,J) = row;
      - row ← row + 1;
      - T(row,3I − 2) = 1; T(row,3I − 1) = $-d_x^{IJ}/3$; T(row,3I) = $-d_y^{IJ}/3$;
      - R(J,I) = row;

      }
   }
6. row = n^2;
7. for $I = 1 \rightarrow n - 2$ {
   (a) for $J = I + 1 \rightarrow n - 1$ {
      i. for $K = J + 1 \rightarrow n$ {
         - row ← row + 1;
         - compute α_I, α_J, α_K, β_I, β_J, β_K using Eq. (5.26);
         - T(row,3I − 2) = 1/3; T(row,3I − 1) = $\alpha_I/4$; T(row,3I) = $\beta_I/4$;
         - T(row,3J − 2) = 1/3; T(row,3J − 1) = $\alpha_J/4$; T(row,3J) = $\beta_J/4$;
         - T(row,3K − 2) = 1/3; T(row,3K − 1) = $\alpha_K/4$;
           T(row,3K) = $\beta_K/4$;

         }
      }
   }

Table 5.1: Pseudo-code for construction of the transformation matrix $[\mathbf{T}]$.

finite elements. Then, the transformation matrix $[\mathbf{T}]$ for a cubic triangular patch ($m = 3$, $n = 3$) is presented to illustrate the computational methodology for shape function calculations.

Example 1 Consider a point $x \in \Omega = (0, 1)$ with natural neighbors at $x_1 = 0$ and $x_2 = 1$. We recall Eq. (5.11) which is the one-dimensional $C^1(\Omega)$ interpolant in BB-form:

$$w(x) = B^3_{3,0} b_{3,0} + B^3_{2,1} b_{2,1} + B^3_{1,2} b_{1,2} + B^3_{0,3} b_{0,3}, \tag{5.28a}$$

where

$$B^3_{3,0} = (1-x)^3, \quad B^3_{2,1} = 3(1-x)^2 x, \quad B^3_{1,2} = 3(1-x)x^2, \quad B^3_{0,3} = x^3. \tag{5.28b}$$

From Eq. (5.20), we immediately have $w_1 = b_{3,0}$ and $w_2 = b_{0,3}$. Let $\theta_1 = w_{,x}(x_1)$ and $\theta_2 = w_{,x}(x_2)$. Then, on using Eq. (5.24), we obtain

$$b_{2,1} = \frac{\theta_1}{3} + w_1, \tag{5.29a}$$

$$b_{1,2} = -\frac{\theta_2}{3} + w_2, \tag{5.29b}$$

and hence the transformation equation given in Eq. (5.13b) can be written as

$$\begin{Bmatrix} b_{3,0} \\ b_{0,3} \\ b_{2,1} \\ b_{1,2} \end{Bmatrix} = \begin{bmatrix} 1 & 0 & 0 & 0 \\ 0 & 0 & 1 & 0 \\ 1 & \frac{1}{3} & 0 & 0 \\ 0 & 0 & 1 & -\frac{1}{3} \end{bmatrix} \begin{Bmatrix} w_1 \\ \theta_1 \\ w_2 \\ \theta_2 \end{Bmatrix}. \tag{5.30}$$

On using Eq. (5.27a) in conjunction with Eqs. (Eq. (5.28)) and (Eq. (5.30)), we obtain the following equations for the $C^1(\Omega)$ NEM shape functions:

$$\psi_1(x) = B^3_{3,0} + B^3_{2,1} = 1 - 3x^2 + 2x^3, \tag{5.31a}$$

$$\psi_2(x) = \frac{1}{3}B^3_{2,1} = x - 2x^2 + x^3, \tag{5.31b}$$

$$\psi_3(x) = B^3_{0,3} + B^3_{1,2} = 3x^2 - 2x^3, \tag{5.31c}$$

$$\psi_4(x) = -\frac{1}{3}B^3_{1,2} = -x^2 + x^3, \tag{5.31d}$$

which are cubic Hermite polynomials.

Example 2 The Bézier ordinates for a cubic triangular patch ($m = 3$, $n = 3$) are indicated in Fig. 5.3 and the relation for the center ordinate is presented in Eq. (5.9). For any point $\mathbf{x}$ in a triangle, the natural neighbor shape functions $\phi_I(\mathbf{x})$ at $\mathbf{x}$ are identical to the barycentric coordinates of $\mathbf{x}$ (Farin, 1990b). For simplicity, we consider the $\triangle_{ABC}$ with vertices $A(0,0)$, $B(1,0)$, and $C(0,1)$. There are ten cubic triangular Bézier ordinates, of which three are vertex ordinates, six are tangent ordinates, and one is a center ("free") ordinate. On using Eqs. (5.24) and (5.25), with the parameters computed from Eq. (5.26), we can relate the nodal vector $\{\mathbf{w}\}$ to the

Bézier ordinate vector $\{\mathbf{b}\}$ through the following equation:

$$\{\mathbf{b}\} = [\mathbf{T}]\{\mathbf{w}\} \Rightarrow \begin{Bmatrix} b_{3,0,0} \\ b_{0,3,0} \\ b_{0,0,3} \\ b_{2,1,0} \\ b_{1,2,0} \\ b_{2,0,1} \\ b_{1,0,2} \\ b_{0,2,1} \\ b_{0,1,2} \\ b_{1,1,1} \end{Bmatrix} = \begin{bmatrix} 1 & 0 & 0 & 0 & 0 & 0 & 0 & 0 & 0 \\ 0 & 0 & 0 & 1 & 0 & 0 & 0 & 0 & 0 \\ 0 & 0 & 0 & 0 & 0 & 0 & 1 & 0 & 0 \\ 1 & \frac{1}{3} & 0 & 0 & 0 & 0 & 0 & 0 & 0 \\ 0 & 0 & 0 & 1 & -\frac{1}{3} & 0 & 0 & 0 & 0 \\ 1 & 0 & \frac{1}{3} & 0 & 0 & 0 & 0 & 0 & 0 \\ 0 & 0 & 0 & 0 & 0 & 0 & 1 & 0 & -\frac{1}{3} \\ 0 & 0 & 0 & 1 & -\frac{1}{3} & \frac{1}{3} & 0 & 0 & 0 \\ 0 & 0 & 0 & 0 & 0 & 0 & 1 & \frac{1}{3} & -\frac{1}{3} \\ \frac{1}{3} & \frac{1}{12} & \frac{1}{12} & \frac{1}{3} & -\frac{1}{6} & \frac{1}{12} & \frac{1}{3} & \frac{1}{12} & -\frac{1}{6} \end{bmatrix} \begin{Bmatrix} w_1 \\ \theta_{1x} \\ \theta_{1y} \\ w_2 \\ \theta_{2x} \\ \theta_{2y} \\ w_3 \\ \theta_{3x} \\ \theta_{3y} \end{Bmatrix}. \quad (5.32)$$

Let the nodes be numbered as 1, 2, and 3. Then, the BB-basis functions are

$$B_{i_1,i_2,i_3}(\mathbf{x}) = \frac{3!}{i_1!\, i_2!\, i_3!} \phi_1^{i_1}(\mathbf{x}) \phi_2^{i_2}(\mathbf{x}) \phi_3^{i_3}(\mathbf{x}), \quad (5.33)$$

where $i_1 + i_2 + i_3 = 3$ and $\phi_1(\mathbf{x}) = 1 - x - y$, $\phi_2(\mathbf{x}) = x$, and $\phi_3(\mathbf{x}) = y$ are the natural neighbor shape functions. The ten components of the vector $\{\mathbf{B}(\mathbf{\Phi})\}$ are computed from the above equation. Since $[\mathbf{T}]$ is known from Eq. (5.32), the shape function vector $\{\mathbf{\Psi}(\mathbf{\Phi})\}$ and its derivatives are readily computed from Eq. (5.27).

Remark. *A cubic Bernstein-Bézier surface representation over a triangle leads to a C^0 interpolant. In the natural element method, as a point* $\mathbf{x}$ *approaches a Delaunay edge, which is within the convex hull of the domain, the number of neighbors for* $\mathbf{x}$ *is greater than three, and consequently a smooth interpolant is realized in that region.*

5.3.3 Properties

Most of the properties of $C^0(\Omega)$ natural neighbor shape functions and Bernstein-Bézier basis functions are retained by $C^1(\Omega)$ shape functions, but there do exist a few differences and some notable exceptions. We present some of the most important properties of $C^1(\Omega)$ NEM shape functions.

Interpolation, Partition of Unity, and Quadratic Completeness The interpolant proposed in Eq. (5.14) is an alternate representation of Farin's $C^1(\Omega)$ interpolant that appears in Eq. (5.12). Since $C^1(\Omega)$ NEM shape functions are linear combinations of Bernstein-Bézier basis functions, cardinal interpolation of the function $w(\mathbf{x})$ is immediately seen:

$$\psi_{3I-2}(\mathbf{x}_J) = \delta_{IJ},\ \psi_{3I-1}(\mathbf{x}_J) = 0,\ \psi_{3I}(\mathbf{x}_J) = 0 \ \Rightarrow\ w^h(\mathbf{x_J}) = w(\mathbf{x}_J). \tag{5.34}$$

In addition, it is obvious that the quadratic precision property of Eq. (5.12) also holds for the re-cast form proposed in Eq. (5.14). By the above inferences, we immediately arrive at the following properties:

$$\sum_{j=1}^{3n} \psi_j(\mathbf{x}) w_j = w(\mathbf{x}_j) \quad \forall\ w(\mathbf{x}) = \sum_{\substack{i+j\leq 2\\ i,\,j\geq 0}} a_{ij} x^i y^j, \quad a_{ij} \in \mathbb{R}, \tag{5.35a}$$

$$\sum_{I=1}^{n} \psi_{3I-2}(\mathbf{x}) = 1. \tag{5.35b}$$

Equation (5.35a) is the statement of quadratic completeness of the NEM interpolant, and Eq. (5.35b), which can be viewed as a consequence of Eq. (5.35a) for $w(\mathbf{x}) \equiv 1$,

indicates that the NEM shape functions associated with the nodal function values form a partition of unity.

Positivity Natural neighbor shape functions $\phi_I(\mathbf{x})$ as well as Bernstein-Bézier basis functions $B^3_{\mathbf{i}}$ share the property of positivity:

$$0 \leq \phi_I(\mathbf{x}) \leq 1, \quad 0 \leq B^3_{\mathbf{i}} \leq 1. \tag{5.36}$$

As opposed to the above, only the NEM shape functions $\psi_{3I-2}(\mathbf{x})$ that correspond to the nodal function values share the above property, namely

$$0 \leq \psi_{3I-2}(\mathbf{x}) \leq 1, \tag{5.37}$$

whereas $\psi_{3I-1}(\mathbf{x})$ as well as $\psi_{3I}(\mathbf{x})$ can assume both positive as well as negative values. A shape function of the form $\psi_{3I-2}(\mathbf{x})$ is illustrated in Fig. 5.4a, and one akin to $\psi_{3I-1}(\mathbf{x})$ is shown in Fig. 5.4b.

Interpolation to Nodal Rotations It was mentioned in Section 5.3.2 that the NEM interpolant in Eq. (5.14) interpolates to both, nodal function and nodal gradient values. The former is evident by virtue of Eq. (5.34). The latter is shown below.

Claim. *The $C^1(\Omega)$ interpolant in Eq. (5.14) interpolates to nodal gradient values:*

$$w^h_{,x}(\mathbf{x}_I) = \theta_{Ix}, \quad w^h_{,y}(\mathbf{x}_I) = \theta_{Iy}. \tag{5.38}$$

Proof. Consider a cubic n-gon simplex in the plane, where n is the number of natural neighbors for a point $\mathbf{x} \in \Omega$. The Bézier ordinate at $\mathbf{x}_I$ is $b_{3\mathbf{e}_I}$, and the directional derivative along a direction d at $\mathbf{x}_I$ is influenced only by the tangent Bézier ordinates that are connected to $b_{3\mathbf{e}_I}$. These ordinates are of the form $b_{2\mathbf{e}_I+\mathbf{e}_J}$, where $J = I$ is a vertex ordinate, and the rest are tangent ordinates. It is evident that the Bézier ordinates $b_{2\mathbf{e}_I+\mathbf{e}_J}$ are related to only w_I, θ_{Ix}, and θ_{Iy}—see Eq. (5.24). The Bernstein-Bézier basis function derivatives associated with these ordinates are the only ones that are non-zero at $\mathbf{x}_I$. For simplicity, without any loss of generality, we let $I = 1$, i.e., local node 1 with nodal location $\mathbf{x}_1$ is considered. In Fig. 5.1 where $n = 3$, the ordinates of interest are $b_{3,0,0}$, $b_{2,1,0}$, and $b_{2,0,1}$, and in Fig. 5.2 where $n = 4$, the ordinates are $b_{3,0,0,0}$, $b_{2,1,0,0}$, $b_{2,0,1,0}$, and $b_{2,0,0,1}$. Hence, the vector consisting of Bernstein-Bézier basis function derivatives at the point $\mathbf{x}_1$ can be written as

$$\{\mathbf{B}_{,\alpha}(\mathbf{x}_1)\}^T = \{B_{1,\alpha}(\mathbf{x}_1), \underbrace{\ldots\ldots}_{n-1 \text{ zeros}}, \underbrace{B_{2,\alpha}(\mathbf{x}_1), 0, \ldots, B_{n,\alpha}(\mathbf{x}_1), 0}_{\frac{n^2-n}{2} \text{ zeros}}, \underbrace{\ldots\ldots}_{\binom{n}{3} \text{ zeros}}\}, \tag{5.39a}$$

where

$$B_1(\mathbf{x}) = \phi_1^3(\mathbf{x}), \quad B_J(\mathbf{x}) = 3\phi_1^2(\mathbf{x})\phi_J(\mathbf{x}), \quad (J = 2, \ldots, n), \tag{5.39b}$$

$$B_{J,\alpha}(\mathbf{x}_1) = 3\phi_{J,\alpha}(\mathbf{x}_1), \quad (J = 1, 2, \ldots, n;\ \alpha = x, y), \tag{5.39c}$$

where the interpolating property $\phi_J(\mathbf{x}_1) = \delta_{J1}$ is used to arrive at Eq. (5.39c). Now, we consider the structure of $[\mathbf{T}]$ to determine the entries that are of interest. Since the Bézier ordinates $b_{2\mathbf{e}_1+\mathbf{e}_J}$ are related to only w_1, θ_{1x}, and θ_{1y}, it suffices if we only consider the first three columns of $[\mathbf{T}]$. Let $[\hat{\mathbf{T}}]$ be such a sub-matrix of $[\mathbf{T}]$. We must

point out that the entries in $[\hat{\mathbf{T}}]$ due to the center Bézier ordinates are non-zero. The associated basis function derivatives are zero, however, and hence the center ordinates provide no contribution to any of the components in the NEM shape function vector. Using Eq. (5.24), the matrix $[\hat{\mathbf{T}}]$ can be written as

$$[\hat{\mathbf{T}}] = \left[\begin{array}{ccc} 1 & 0 & 0 \\ 0 & 0 & 0 \\ \cdots & \cdots & \cdots \\ 0 & 0 & 0 \\ \hline 1 & \alpha_x^{12} & \alpha_y^{12} \\ 0 & 0 & 0 \\ 1 & \alpha_x^{13} & \alpha_y^{13} \\ 0 & 0 & 0 \\ \cdots & \cdots & \cdots \\ \cdots & \cdots & \cdots \\ 1 & \alpha_x^{1n} & \alpha_y^{1n} \\ 0 & 0 & 0 \\ \hline c_{11} & c_{12} & c_{13} \\ \cdots & \cdots & \cdots \\ c_{m1} & c_{m2} & c_{m3} \end{array}\right], \tag{5.40}$$

where $c_{ij} \in \mathbb{R}$, $m = \binom{n}{3}$, and $\alpha_x^{1J} = d_x^{1J}/3$ and $\alpha_y^{1J} = d_y^{1J}/3$. The sub-matrices corresponding to the vertex, tangent, and center Bézier ordinates are indicated by the enclosed boxes in the above equation. By virtue of Eq. (5.26), we have

$$d_x^{1J} = x_J - x_1, \quad d_y^{1J} = y_J - y_1, \quad (J = 2, 3, \ldots, n). \tag{5.41}$$

On taking the product of Eqs. (5.39) and (5.40), we can write the non-zero $C^1(\Omega)$ shape function derivatives as

$$\psi_{1,\alpha}(\mathbf{x}_1) = \sum_{J=1}^{n} \phi_{J,\alpha}(\mathbf{x}_1), \tag{5.42a}$$

$$\psi_{2,\alpha}(\mathbf{x}_1) = \sum_{J=2}^{n} \phi_{J,\alpha}(\mathbf{x}_1) d_x^{1J}, \tag{5.42b}$$

$$\psi_{3,\alpha}(\mathbf{x}_1) = \sum_{J=2}^{n} \phi_{J,\alpha}(\mathbf{x}_1) d_y^{1J}. \tag{5.42c}$$

Since $\sum_J \phi_J(\mathbf{x}_1) = 1$, it follows that Eq. (5.42a) is identically equal to zero. On substituting Eq. (5.41) in the above equation and noting that $\phi_{1,\alpha}(\mathbf{x}_1) = -\sum_{J=2}^{n} \phi_{J,\alpha}(\mathbf{x}_1)$, we obtain

$$\psi_{1,\alpha}(\mathbf{x}_1) = 0, \tag{5.43a}$$

$$\psi_{2,\alpha}(\mathbf{x}_1) = \sum_{J=1}^{n} \phi_{J,\alpha}(\mathbf{x}_1) x_J, \tag{5.43b}$$

$$\psi_{3,\alpha}(\mathbf{x}_1) = \sum_{J=1}^{n} \phi_{J,\alpha}(\mathbf{x}_1) y_J. \tag{5.43c}$$

But the natural neighbor shape functions satisfy the local coordinate property given in Eq. (3.10), namely

$$\sum_{J=1}^{n} \phi_J(\mathbf{x}) \mathbf{x}_J = \mathbf{x}, \tag{5.44}$$

and hence on taking the derivative of the above equation with respect to x and y in succession and substituting in Eq. (5.43), we obtain

$$\psi_{1,x}(\mathbf{x}_1) = 0, \quad \psi_{2,x}(\mathbf{x}_1) = 1, \quad \psi_{3,x}(\mathbf{x}_1) = 0, \tag{5.45a}$$

$$\psi_{1,y}(\mathbf{x}_1) = 0, \quad \psi_{2,y}(\mathbf{x}_1) = 0, \quad \psi_{3,y}(\mathbf{x}_1) = 1. \tag{5.45b}$$

Now, the derivatives of the NEM trial function given in Eq. (5.14) can be written as

$$w^h_{,x}(\mathbf{x}_1) = \psi_{1,x}(\mathbf{x}_1)w_1 + \psi_{2,x}(\mathbf{x}_1)\theta_{1x} + \psi_{3,x}(\mathbf{x}_1)\theta_{1y}, \tag{5.46a}$$

$$w^h_{,y}(\mathbf{x}_1) = \psi_{1,y}(\mathbf{x}_1)w_1 + \psi_{2,y}(\mathbf{x}_1)\theta_{1x} + \psi_{3,y}(\mathbf{x}_1)\theta_{1y}, \tag{5.46b}$$

and hence on using Eq. (5.45) in the above equation, we obtain

$$w^h_{,x}(\mathbf{x}_1) = \theta_{1x}, \quad w^h_{,y}(\mathbf{x}_1) = \theta_{1y}. \tag{5.47}$$

Since the choice $I = 1$ is arbitrary, the above relations are readily extended for all I $(1 \leq I \leq n)$, which leads us to the desired result:

$$w^h_{,x}(\mathbf{x}_I) = \theta_{Ix}, \quad w^h_{,y}(\mathbf{x}_I) = \theta_{Iy}. \qquad \square \tag{5.48}$$

By virtue of Eqs. (5.34) and (5.45), we note an additional property—$C^1(\Omega)$ NEM shape functions are cardinal with respect to both, function evaluation, as well as

differentiation with respect to the coordinate directions:

$$\psi_{3I-2}(\mathbf{x}_J) = \delta_{IJ}, \qquad \psi_{3I-1}(\mathbf{x}_J) = 0, \qquad \psi_{3I}(\mathbf{x}_J) = 0, \tag{5.49a}$$

$$\psi_{3I-2,x}(\mathbf{x}_J) = 0, \qquad \psi_{3I-1,x}(\mathbf{x}_J) = \delta_{IJ}, \quad \psi_{3I,x}(\mathbf{x}_J) = 0, \tag{5.49b}$$

$$\psi_{3I-2,y}(\mathbf{x}_J) = 0, \qquad \psi_{3I-1,y}(\mathbf{x}_J) = 0, \qquad \psi_{3I,y}(\mathbf{x}_J) = \delta_{IJ}. \tag{5.49c}$$

5.4 Governing Equations and Weak Form

As a model fourth-order partial differential equation, we consider the biharmonic equation with Dirichlet boundary conditions, which is described as

$$\Delta^2 w = f \quad \text{in } \Omega, \tag{5.50a}$$

$$w = g_1 \quad \text{on } \Gamma, \tag{5.50b}$$

$$\frac{\partial w}{\partial n} = g_2 \quad \text{on } \Gamma, \tag{5.50c}$$

where $\Omega \subset \mathbb{R}^2$ is an open bounded domain and Γ is its boundary, n is the outward normal to Ω, and Δ is the Laplacian operator. Referring to the discussion in Chapter 2, we note that since the biharmonic equation is a fourth-order elliptic PDE ($m = 2$), the space of admissible functions is $V = H^2(\Omega)$. The weak or variational problem is posed as:

$$\text{Find } w \in V = H^2(\Omega) \text{ such that}$$

$$a(w, v) = \langle f, v \rangle \quad \forall\, v \in V_0 = H_0^2(\Omega), \tag{5.51}$$

where $a(w,v) : V \times V \to \mathbb{R}$ is the bilinear form for the biharmonic operator and $\langle f, v\rangle$ is the duality pairing which is defined as

$$\langle f, v\rangle = \int_\Omega f v \, d\Omega. \tag{5.52}$$

In Eq. (5.51), $V = H^2(\Omega)$ and $V_0 = H_0^2(\Omega)$ are Sobolev spaces (see Chapter 2). As opposed to the Laplace operator discussed in Chapter 2, two distinct Dirichlet (bilinear) forms exist for the biharmonic operator (Agmon, 1965):

$$a_1(w,v) = \int_\Omega \Delta w \Delta v \, d\Omega, \tag{5.53a}$$

$$a_2(w,v) = \int_\Omega \big[(w_{,xx} - w_{,yy})(v_{,xx} - v_{,yy}) + 4 w_{,xy} v_{,xy}\big] \, d\Omega. \tag{5.53b}$$

Any linear combination of the above two equations is also a Dirichlet form. For the plate problem, the bilinear form (strain energy) is given by (Landau and Lifschitz, 1970; Ciarlet, 1978):

$$a_3(w,v) = \int_\Omega \big[\Delta w \Delta v - (1-\nu)(w_{,xx} v_{,yy} + w_{,yy} v_{,xx} - 2 w_{,xy} v_{,xy})\big] d\Omega, \tag{5.54}$$

where ν is the Poisson's ratio. By application of Green's formulas given in Eq. (2.19), we have

$$\int_\Omega \Delta w \Delta v \, d\Omega = \int_\Omega \big(\Delta^2 w\big) v \, d\Omega - \int_\Gamma \Delta w_{,n} v \, d\Gamma - \int_\Gamma \Delta w v_{,n} \, d\Gamma, \tag{5.55a}$$

$$\int_\Omega \big[w_{,xx} v_{,yy} + w_{,yy} v_{,xx} - 2 w_{,xy} v_{,xy}\big] d\Omega = \int_\Gamma w_{,tt} v_{,n} \, d\Gamma - \int_\Gamma w_{,nt} v_{,t} \, d\Gamma, \tag{5.55b}$$

where n and t are the outward normal and tangential directions to Γ, and Eq. (5.55a) is obtained by replacing u by Δu in Eq. (2.19b). For the Dirichlet problem with $v \in V_0$, the boundary integrals in the above equations are zero, and w satisfies the strong form given in Eq. (5.50). The bilinear form for the biharmonic equation given in Eq. (5.53a) and that for the plate problem indicated in Eq. (5.54) are both bounded, symmetric and positive definite operators in V_0, and therefore there exists a unique solution w to the variational problem in Eq. (5.51) (Ciarlet, 1978).

Consider the Galerkin implementation for the natural element method. Using the bilinear form given in Eq. (5.53a), the weak form for the discrete problem can be stated as:

$$\begin{gathered}\text{Find } w \in V^h \subset V \quad \text{such that} \\ a_1(w^h, v^h) = \langle f, v^h \rangle \quad \forall\, v^h \in V_0^h \subset V_0. \end{gathered} \tag{5.56}$$

In a Bubnov-Galerkin procedure, the trial function w^h as well as the test function v^h are represented in terms of the same shape functions. The trial and test functions are

$$\left\{ w^h \quad v^h \right\} = \sum_{I=1}^{n} \left\{ \mathbf{\Psi}_I \right\} \left[\mathbf{w}_I \quad \mathbf{v}_I \right], \tag{5.57a}$$

where

$$\mathbf{\Psi}_I^T = \begin{Bmatrix} \psi_{3I-2} \\ \psi_{3I-1} \\ \psi_{3I} \end{Bmatrix}, \quad \mathbf{w}_I = \begin{Bmatrix} w_I^h \\ \theta_{Ix}^{w^h} \\ \theta_{Iy}^{w^h} \end{Bmatrix}, \quad \mathbf{v}_I = \begin{Bmatrix} v_I^h \\ \theta_{Ix}^{v^h} \\ \theta_{Iy}^{v^h} \end{Bmatrix}. \tag{5.57b}$$

The discrete Laplacian for the trial and test functions can be written as

$$\left\{\Delta w^h \quad \Delta v^h\right\} = \sum_{I=1}^{n} \left\{\mathbf{B}_I\right\} \left[\mathbf{w}_I \quad \mathbf{v}_I\right], \tag{5.58a}$$

where

$$\mathbf{B}_I^T = \begin{Bmatrix} \psi_{3I-2,xx} + \psi_{3I-2,yy} \\ \psi_{3I-1,xx} + \psi_{3I-1,yy} \\ \psi_{3I,xx} + \psi_{3I,yy} \end{Bmatrix}. \tag{5.58b}$$

On substituting the trial and test functions in Eq. (5.56) and using the arbitrariness of nodal variations, the following discrete system of linear equations is obtained:

$$\boldsymbol{K}\mathbf{d} = \mathbf{f}, \tag{5.59}$$

where

$$\mathbf{K}_{IJ} = \int_{\Omega^h} \mathbf{B}_I^T \mathbf{B}_J \, d\Omega, \tag{5.60a}$$

$$\mathbf{f}_I = \int_{\Omega^h} \boldsymbol{\Psi}_I^T f \, d\Omega. \tag{5.60b}$$

In the above equations, $\mathbf{d}$ is the vector of nodal function and gradient values, $\boldsymbol{\Psi}_I$ is the nodal shape function vector, and $\mathbf{B}_I$ is the discrete Laplacian vector.

5.5 Numerical Results

The application of NEM to the biharmonic equation with Dirichlet boundary conditions is presented. The $L^2(\Omega)$ and energy error norms that are used in the analyses are defined as:

$$\|w - w^h\|_{L^2(\Omega)} = \left(\int_\Omega (w - w^h)^2 \, d\Omega \right)^{1/2}, \tag{5.61a}$$

$$\|w - w^h\|_{E(\Omega)} = \left(\frac{1}{2} \int_\Omega a_1(w - w^h, w - w^h) \, d\Omega \right)^{1/2}, \tag{5.61b}$$

where w and w^h are the exact and numerical (NEM) solutions, respectively. Numerical integration of the weak form is carried out using symmetric quadrature rules for a triangle (Dunavant, 1985). In the error norm computations, 25 point quadrature rule is used in each triangle. The packages *Triangle* (Shewchuk, 1996b) and *Show Me* (Shewchuk, 1996a) are used to construct and display the nodal discretization and Delaunay triangles.

5.5.1 Airy Stress Function

The Airy stress function in small displacement linear elastostatics satisfies the biharmonic equation. A wide range of two- and three-dimensional problems, ranging from homogeneous deformation to those with point and line singularities, are encompassed within this theoretical framework. In fracture mechanics, numerical methods are an invaluable tool to compute fracture parameters that are associated with the fracture and failure of cracked-bodies. Bernal and Whiteman (1970) used finite difference approximations, and Gregory et al. (1978) used local mesh refinement with modi-

fied C^1 bicubic interpolants to solve the two-dimensional biharmonic problem of an edge-cracked plate under uniaxial tension.

Let w be the Airy stress function in two-dimensional elasticity. As a benchmark problem (patch test) for the homogeneous biharmonic operator, we consider a circular plate under a biaxial state of stress:

$$\Delta^2 w = 0 \quad \text{in } \Omega, \tag{5.62a}$$

$$w = a^2 \quad \text{on } \Gamma, \tag{5.62b}$$

$$\frac{\partial w}{\partial r} = 2a \quad \text{on } \Gamma, \tag{5.62c}$$

where $\Omega = \{(x, y) : x^2 + y^2 < a^2\}$ is a circular domain of radius a and Γ is its boundary.

In polar coordinates, the exact solution for the Airy stress function is: $w(r) = r^2$. Consider a circular domain of unit radius ($a = 1$); due to symmetry, only one-quarter of the circular domain is modeled with appropriate symmetry boundary conditions. The $L^2(\Omega)$ and energy error norm results for four quasi-regular nodal grids are presented in Table 5.2. The nodal grid and the associated Delaunay triangles for a typical discretization are shown in Fig. 5.7. The nodal grids are constructed by setting a $L \times L \times L$ sub-division for the three boundaries. The case $L = 6$ is shown in Fig. 5.7, and the other grids correspond to $L = 12,\ 24$, and 48. In Fig. 5.8, the plot of w and $\partial w/\partial r$ versus the radial distance r for the $L = 6$ grid is presented. In the computations, 25 equi-distant output points between $r = 0$ and $r = 1$ are considered. Since the $C^1(\Omega)$ NEM interpolant has quadratic completeness, the numerical solution should be accurate within machine precision, which is 10^{-16} in double precision arith-

metic on a HP9000/s700 workstation. The inaccuracy in the NEM solution is due to numerical quadrature errors in the integration of the weak form, which was also observed for the patch test in two-dimensional elastostatics (see Section 4.4.2). First and foremost, the numerical integration errors stem from the fact that the support of the shape functions do not coincide with the Delaunay triangles. In addition, the entries in the stiffness matrix $\mathbf{K}$ consist of products of second-order derivatives of NEM shape functions. The integrand is a rational function, which is not accurately integrated using polynomial-precision symmetric quadrature rules over triangles. The selection of an appropriate numerical quadrature scheme for NEM, however, is still an open issue.

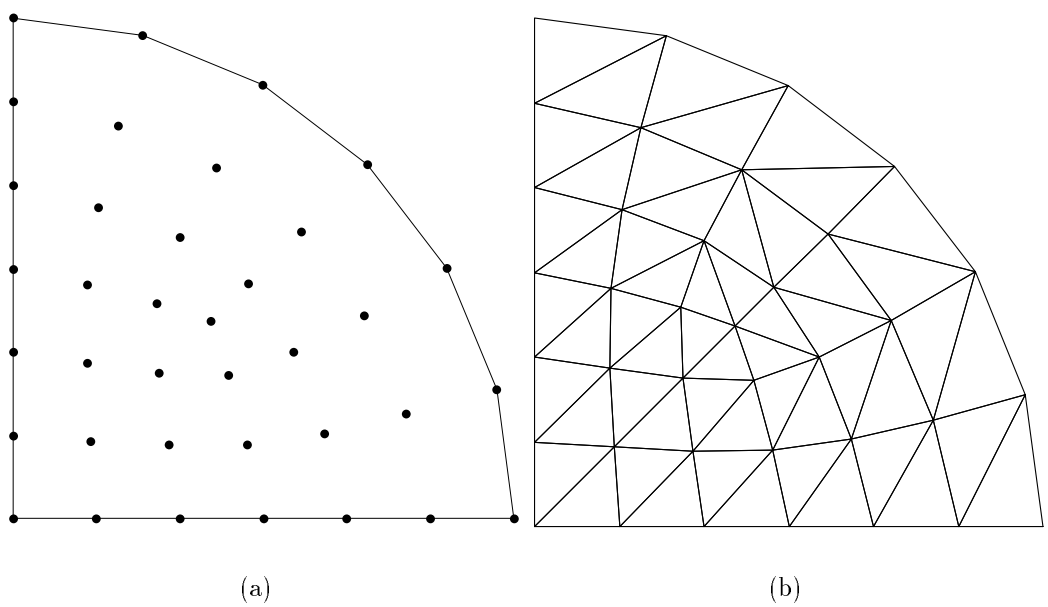

Figure 5.7: Quarter circular plate. (a) Nodal discretization (37 nodes), and (b) Delaunay triangulation.

Table 5.2: Relative error norms for the Airy stress function problem.

Nodal Grids	Quadrature	$\frac{\|w - w^h\|_{L^2(\Omega)}}{\|w\|_{L^2(\Omega)}}$	$\frac{\|w - w^h\|_{E(\Omega)}}{\|w\|_{E(\Omega)}}$
37	3	7.2×10^{-3}	2.7×10^{-1}
	25	8.3×10^{-3}	1.1×10^{-1}
	37	9.7×10^{-3}	1.2×10^{-1}
127	3	8.2×10^{-3}	2.3×10^{-1}
	25	2.6×10^{-3}	9.6×10^{-2}
	37	3.6×10^{-3}	9.5×10^{-2}
469	3	6.9×10^{-3}	2.0×10^{-1}
	25	9.9×10^{-4}	7.3×10^{-2}
	37	1.6×10^{-3}	7.3×10^{-2}
1801	3	4.0×10^{-3}	1.5×10^{-1}
	25	4.7×10^{-4}	5.5×10^{-2}
	37	6.2×10^{-4}	5.3×10^{-2}

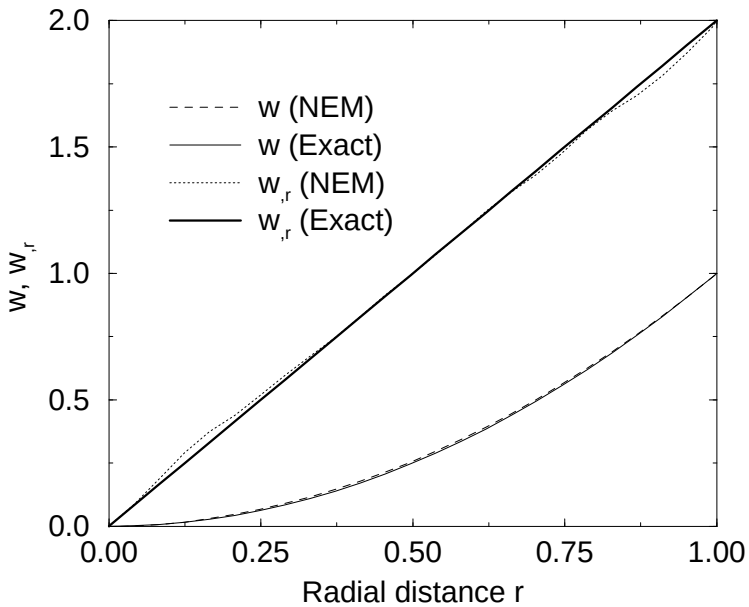

Figure 5.8: Plot of w and $w_{,r}$ versus r for the Airy stress function problem (37 nodes).

5.5.2 Clamped Circular Plate

Consider the axi-symmetric problem of a clamped circular plate under a uniform transverse unit load ($f = 1$). The governing equations are:

$$\Delta^2 w = 1 \quad \text{in } \Omega, \tag{5.63a}$$

$$w = \frac{\partial w}{\partial r} = 0 \quad \text{on } \Gamma, \tag{5.63b}$$

where $\Omega = \{(x, y) : x^2 + y^2 < a^2\}$ is a circular domain of radius a and Γ is its boundary. The exact solution to the above problem is given by (Timoshenko and

Woinowsky-Krieger, 1959)

$$w(r) = \frac{1}{64}(a^2 - r^2)^2. \tag{5.64}$$

Consider a circular domain of unit radius; due to symmetry, only one-quarter of the circular domain is modeled. The nodal discretizations used in the analyses are: 36 [A], 127 [B], 271 [C], 469 [D], 721 [E], 1027 [F], 1387 [G], and 1801 [H] nodes. The sub-division for these grids are: $L = 6,\ 12,\ 18,\ 24,\ 30,\ 36,\ 42$, and 48. In Table 5.3, the normalized center displacement for the above grids are presented, and in Fig. 5.9, the numerical results are illustrated. There is good agreement between the NEM and exact solution. The convergence to the center displacement is monotonic and the error in the center displacement is less than 2% for a grid with more than 200 nodes. The plot of w and $w_{,r}$ as a function of r is illustrated in Fig. 5.10. The grid shown in Fig. 5.7 is used, and 25 equi-spaced output points between $r = 0$ and $r = 1$ are chosen in the computations. A convergence study is carried out using the nodal grids A–H. The relative $L^2(\Omega)$ and energy error norms are shown against a measure of the nodal spacing h ($h = a/L$, $a = 1$ is the plate radius) on a log–log plot (Fig. 5.11). In Fig. 5.11, the convergence rate is indicated by the value of R. The rate of convergence in displacement and energy is 0.95 and 0.41, respectively; optimal rates are 2 and 1 in displacement and energy for a conforming finite element with quadratic completeness (Strang and Fix, 1973). In order to study the sub-optimal rates of convergence, an eigenanalysis is carried out in the following section. The results indicate that the discrete bilinear operator is V_0^h-elliptic and hence stable, while the approximation space is not well-conditioned. The sub-optimal rates of

Table 5.3: Normalized center displacement for the uniformly loaded circular plate.

Nodal Grids	Quadrature	$\frac{w^h}{w}$
37	3	1.0986
	25	1.0408
127	3	1.0817
	25	1.0224
271	3	1.0639
	25	1.0147
469	3	1.0565
	25	1.0117
721	3	1.0463
	25	1.0095
1027	3	1.0392
	25	1.0082
1387	3	1.0331
	25	1.0071
1801	3	1.0292
	25	1.0061

convergence is attributable to the latter factor in conjunction with the numerical integration errors in the computations.

5.5.3 Eigenanalysis

In order to study stability, we look at the properties of the approximation spaces and the ellipticity of the discrete bilinear operator. The public-domain eigensolver EISPACK (Smith et al., 1974) is used to solve the eigenproblems that follow.

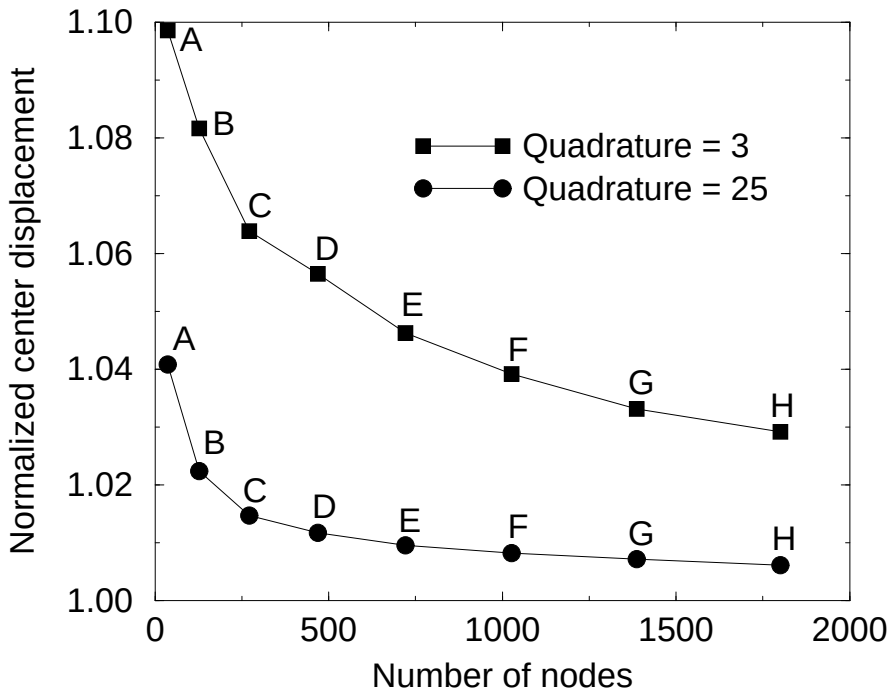

Figure 5.9: Variation of normalized center displacement with number of nodes for the uniformly loaded clamped circular plate.

Linear Independence of Shape Functions The approximation space is studied by considering the linear independence of the shape functions. To this end, we consider the following discrete eigenvalue problem:

$$\mathbf{M}\hat{\mathbf{w}} = \lambda^h \hat{\mathbf{w}}, \tag{5.65}$$

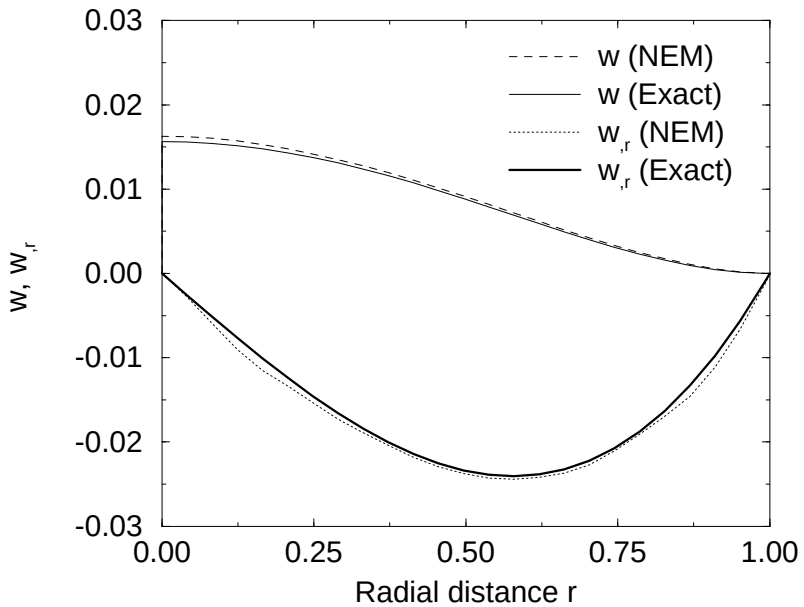

Figure 5.10: Plot of w and $w_{,r}$ versus r for the uniformly loaded clamped circular plate (37 nodes).

where $\hat{\mathbf{w}}$ and λ^h are the eigenvectors and eigenvalues of $\mathbf{M}$, and $\mathbf{M}$ is the mass matrix which is given by

$$\mathbf{M}_{IJ} = \int_\Omega \mathbf{\Psi}_I^T \mathbf{\Psi}_J \, d\Omega. \tag{5.66}$$

The condition number $\kappa(\mathbf{M}) = \lambda_{max}(\mathbf{M})/\lambda_{min}(\mathbf{M})$ is used as a measure of the linear independence of the shape functions. The leading eigenvalue λ^h_{3I-2} which corresponds to the eigenvector $\hat{\mathbf{w}}_{3I-2}$ is used to compute the condition number; the other eigenvalues are deemed spurious and vanish in the limit $h \to 0$ (Strang and Fix, 1973). In Table 5.4, the condition number is computed for the nodal grids A, B, C, D, and H (see Section 5.5.2). It is seen that the condition numbers increase markedly with nodal

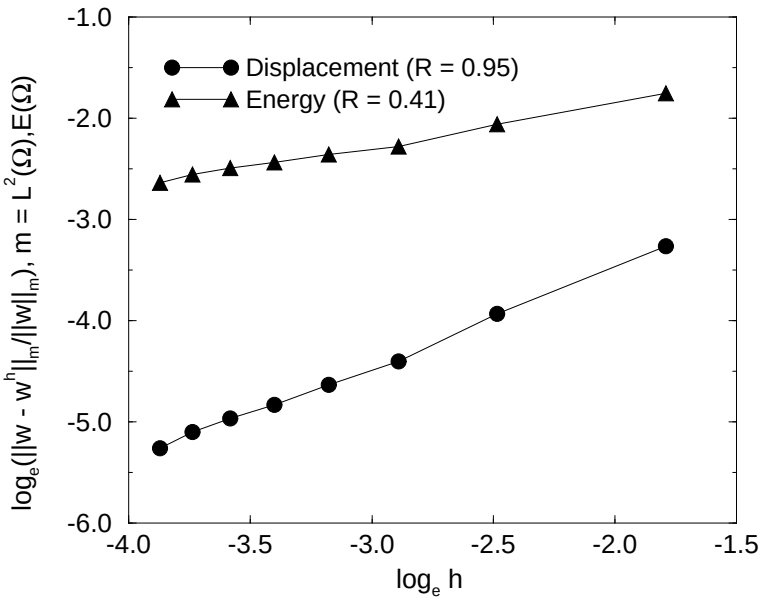

Figure 5.11: Rate of convergence in displacement and energy for the uniformly loaded clamped circular plate.

refinement thereby indicating that the system is not well-conditioned. This indicates that the $C^1(\Omega)$ NEM approximation spaces are not uniformly linearly independent. An immediate consequence of this is that the accuracy of the computed results could be affected, since if the condition number is 10^s then as many as s digits may be lost during the solution of the system $\mathbf{Kd} = \mathbf{f}$ (Strang and Fix, 1973). Keeping this in mind, we now consider the stability of the discrete operator, which is of far greater significance for the stability and convergence of the numerical method.

Ellipticity The continuity of the discrete bilinear operator $a(w^h, v^h)$: $V^h \times V_0^h \to \mathbb{R}$ is established by virtue of choosing conforming finite-dimensional subspaces $w^h \in V^h$ and $v^h \in V_0^h$. For showing V_0^h-ellipticity of the operator, it suffices if the following

Table 5.4: Condition number of the mass matrix.

Nodal Grids	$\kappa = \dfrac{\lambda^h_{max}}{\lambda^h_{min}}$
37	8.57×10^3
127	8.35×10^4
271	2.69×10^5
469	5.87×10^5
1801	9.42×10^9

condition is satisfied:

$$a(v^h, v^h) \geq \alpha \|v^h\|^2 \quad \forall\, v^h \in V_0^h \subset H_0^2(\Omega), \tag{5.67}$$

where the positive constant α is bounded away from zero. The ellipticity constant for the discrete operator is numerically estimated by considering the generalized eigenproblem associated with the biharmonic equation:

$$\Delta^2 \tilde{w} = \lambda \tilde{w} \quad \text{in } \Omega, \tag{5.68a}$$

$$\tilde{w} = \tilde{w}_{,n} = 0 \quad \text{on } \Gamma, \tag{5.68b}$$

where $\tilde{w}$ is the natural mode of vibration of the plate, $\lambda = \omega^2$ is the eigenvalue, and ω the natural frequency of vibration. The equivalent variational form for the

eigenproblem is:

$$\text{Find } \tilde{w} \in V = H^2(\Omega) \text{ such that}$$
$$\int_\Omega \Delta\tilde{w}\Delta\tilde{v}\, d\Omega = \lambda(\tilde{w}, \tilde{v}) \quad \forall\ \tilde{v} \in V_0 = H_0^2(\Omega). \tag{5.69}$$

The weak form for the discrete problem is posed as:

$$\text{Find } \tilde{w}^h \in V^h \subset V \text{ such that}$$
$$\int_\Omega \Delta\tilde{w}^h\Delta\tilde{v}^h\, d\Omega = \lambda^h(\tilde{w}^h, \tilde{v}^h) \quad \forall\ \tilde{v}^h \in V_0^h \subset V_0. \tag{5.70}$$

By substituting the discrete trial and test functions in the above equation, and using the arbitrariness of nodal variations, we obtain the following discrete eigensystem:

$$\mathbf{K}\bar{\mathbf{w}} = \lambda^h\mathbf{M}\bar{\mathbf{w}}, \tag{5.71}$$

where $\bar{\mathbf{w}}$ and λ^h are the natural eigenmodes and eigenvalues, respectively, $\mathbf{K}_{IJ}$ is the nodal stiffness matrix which is defined in Eq. (5.60a), and $\mathbf{M}_{IJ}$ is the mass matrix given in Eq. (5.66). For the symmetric bilinear form in Eq. (5.70) there exists an increasing sequence of strictly positive eigenvalues for the eigenproblem. By considering the Rayleigh quotient $R(v^h) = a(v^h, v^h)/(v^h, v^h)$ for the discrete problem in conjunction with Eqs. (5.71) and (5.67), we obtain the following result for the ellipticity constant:

$$\alpha = \inf\ \{R(v^h) : v^h \in V_0^h\} = \lambda_1^h, \tag{5.72}$$

where λ_1^h is the lowest eigenvalue with $\omega_1^h = \sqrt{\lambda_1^h}$ the corresponding fundamental frequency. The fundamental frequency that corresponds to the lowest eigenvalue is computed for the nodal grids A–D. The reference solution for the fundamental frequency is $\omega_1 = 10.21$ (Leissa, 1969). The results for the normalized fundamental frequency are presented in Table 5.5; there is good agreement between the numerical solution (NEM) and the reference solution. Clearly, $\alpha = (\omega_1^h)^2$ is approximately a constant and is bounded away from zero. This implies that the ellipticity condition given in Eq. (5.67) is satisfied, and hence the discrete bilinear operator is stable.

Table 5.5: Normalized fundamental frequency for the clamped circular plate.

Nodal Grids	$\frac{\omega_1^h}{\omega_1}$
37	0.9854
127	0.9927
271	0.9951
469	0.9962

Chapter 6

Mixed Natural Element Method in Linear Elasticity

In this Chapter, we pursue a mixed displacement-pressure formulation for the natural element method in linear elastostatics. In the following section, a brief background on mixed formulations is presented. Then, the NEM displacement and pressure interpolants are presented, followed by the governing equations for the boundary value problem of linear elastostatics (incompressible and compressible cases). Finally, applications of the mixed natural element method for the cantilever beam in bending, and for the plate with a circular hole under uniaxial tension are presented.

6.1 Background

Variational formulations that are based on Hellinger-Reissner principle and the Hu-Washizu principle (Washizu, 1982) are well-established and widely-used in finite elements. The term mixed methods refers to finite element methods in which two different fields (for eg., displacement and stress or displacement and strain) are approximated as primary variables; in linear elastostatics, mixed methods assume a particular form of the Hellinger-Reissner variational principle. There are significant

advantages that accrue when one departs from a displacement-based Galerkin method to one involving a two-field or three-field variational principle. The motivation and interest in mixed finite element methods stems from quite a few factors: first, in structural analysis the stress tensor $\boldsymbol{\sigma}$ is very often the key field variable of interest, which can be directly obtained from the solution of a mixed analysis; mixed formulations impose less stringent continuity requirements on the trial and test function spaces, and as a result C^0 trial functions suffice for fourth-order problems that are posed in a mixed variational framework; mixed methods facilitate the representation of smoothly varying stress (pressure) fields by using C^0 interpolation for the stresses (pressure); and lastly, the judicious choice of functions spaces for the primary fields in mixed formulations permits robust and accurate solutions of boundary value problems in limiting cases, such as near incompressibility (Poisson locking) in linear elastostatics when the Poisson's ratio $\nu \to 0.5$, and membrane and shear locking in thin beam and plate problems as the thickness $t \to 0$. A caveat to the above optimism is that the choice of function spaces for the primary fields in mixed methods can not be arbitrary; the accuracy and convergence of the method relies on how well the discrete finite-dimensional subspaces approximate their continuous counterparts, and more importantly, if the discrete function spaces satisfy the Ladyzhenskaya-Babuška-Brezzi (LBB) or inf-sup stability condition (Ladyzhenskaya, 1969; Babuška, 1971; Brezzi, 1974).

Locking in finite elements has primarily been approached using modified variational principles, such as assumed strain methods (Simo and Hughes, 1986), assumed stress methods (Pian and Sumihara, 1984), and selective reduced integration procedures (Hughes, 1987). Brezzi and Fortin (1991) present a detailed analysis of these

methods which are encompassed within the general framework of mixed methods, and Arnold (1990) presents a lucid account of mixed finite element methods for elliptic problems. It is well known that low-order, h-version finite elements cause Poisson locking as the incompressible limit is approached ($\nu \to 0.5$ or $\lambda \to \infty$). The incompressibility constraint tends to impose far too many constraints in the discrete finite element space, and the trial function space is reduced to nullity leading to the phenomena of mesh locking ($\mathbf{u} \cong 0$). For analytical as well as computational issues related to locking, see Babuška and Suri (1992), Suri (1996), and Chilton and Suri (1997). Mixed methods with displacements and pressure as independent variables, and selective reduced integration procedures have been successful in ameliorating this problem. Malkus and Hughes (1978) have shown the equivalence of mixed finite element methods to selective reduced integration techniques.

The scope and application of meshless methods (Belytschko et al., 1996) in mixed formulations has not been explored to any depth so far. In meshless methods, there is greater flexibility than finite elements in the choice and smoothness (C^k, $k > 0$) of trial function spaces. Donning (1997) used the notion of locking-free interpolants that are based on cardinal splines to solve thin as well as thick beam and plate problems using Mindlin-Reissner theory. By judicious choice of local basis functions in the Partition of Unity Method (PUM) (Melenk and Babuška, 1996), Babuška and Zhang (1998) provided a theoretical basis for removing locking in the thin beam limit.

6.2 Displacement and Pressure Interpolation

We consider the interpolation schemes for the displacements and the presurre in the mixed natural element method. The displacement vectors $\mathbf{u}^h(\mathbf{x}) : \Omega \subset \mathbb{R}^2 \to \mathbb{R}^2$ are interpolated using natural neighbor shape functions, and can be written in the form:

$$\mathbf{u}^h(\mathbf{x}) = \sum_{I=1}^{n} \phi_I(\mathbf{x})\mathbf{u}_I, \tag{6.1}$$

where $\mathbf{u}_I$ $(I = 1, 2, \ldots, n)$ are the vectors of nodal displacements at the n natural neighbors, and $\phi_I(\mathbf{x})$ are the shape functions associated with each node.

The pressure field is interpolated by an interpolation scheme akin to Eq. (6.1):

$$p^h(\mathbf{x}) = \sum_{I=1}^{n} \psi_I(\mathbf{x})\bar{p}_I, \tag{6.2}$$

where $\psi_I(\mathbf{x})$ is the shape function associated with node I and $\bar{p}_I$ are the nodal pressures. We consider $\psi_I(\mathbf{x})$ to be of the general form

$$\psi_I(\mathbf{x}) = \frac{\big(\phi_I(\mathbf{x})\big)^k}{\sum_J \big(\phi_J(\mathbf{x})\big)^k}, \tag{6.3}$$

where k is a non-negative integer. The case $k = 1$ reduces to natural neighbor interpolation, and all other k render shape functions that form a partition of unity, with the resulting interpolant satisfying only constant completeness. For $k > 1$, numerical studies show that severe Poisson locking results; the cases $k = 0$ and $k = 1$ performed well in the near incompressible limit and hence merit investigation. These two cases are considered for the interpolation of the pressure field, and Eq. (6.2) takes

the specific forms:

$$p^h(\mathbf{x}) = \sum_{I=1}^{n} \frac{1}{n}\bar{p}_I, \tag{6.4a}$$

$$p^h(\mathbf{x}) = \sum_{I=1}^{n} \phi_I(\mathbf{x})\bar{p}_I. \tag{6.4b}$$

The shape functions $\psi_I(\mathbf{x})$ for $k = 0$ that are used to interpolate the pressure need some elaboration. On the basis of Eq. (6.4a) in conjunction with the variation of natural neighbors for a point $\mathbf{x}$, we note that the shape functions $\psi_I(\mathbf{x}) = 1/n$ are C^{-1} with discontinuities along the union of the boundary of support of $\phi_I(\mathbf{x})$ and the intersection of the boundary of support $\partial\Omega_{J_c}$ of all other $\phi_J(\mathbf{x})$ with the domain of support Ω_{I_c} of node I—see Section 3.3.4. The variation of natural neighbors for a regular (5×5) grid is shown in Fig. 3.5. Since the shape function $\psi_I(\mathbf{x}) = 1/n$ is the inverse of the number of natural neighbors for a point $\mathbf{x}$, the above inference is readily observed. An alternate C^{-1} pressure interpolant can be constructed using the well-known concept of nearest neighbors in computational geometry (Preparata and Shamos, 1985). This leads to the interpolation scheme known as nearest neighbor interpolation. In this approach, if $\mathbf{x} \in T_I$, where T_I is the Voronoi polygon of node I, then we assign the nodal pressure $\bar{p}_I$ to $p(\mathbf{x})$. In essence, the pressure field is assumed to be a constant over the Voronoi polygon T_I. In the context of natural neighbor interpolation, if $\phi_I = \|\boldsymbol{\phi}\|_\infty$, then $\psi_I(\mathbf{x}) = 1$ and $\psi_J(\mathbf{x}) = 0 \ \forall \ J \neq I$, and therefore

$$p(\mathbf{x}) = \bar{p}_I \quad \text{if } \mathbf{x} \in T_I. \tag{6.5}$$

6.3 Governing Equations and Mixed Formulation

6.3.1 Strong Form

Consider an open bounded domain $\Omega \subset \mathbb{R}^2$ with boundary Γ. Let $\mathbf{n}$ be the unit normal vector to Γ; the closure of Ω is denoted by $\bar{\Omega} = \Omega \cup \Gamma$. In Section 4.3, the field equations for compressible elasticity, essential and traction boundary conditions, and the principle of virtual work (weak form) are presented. Here, we consider the governing equations for two-dimensional small displacement elastostatics, with validity for both compressible and incompressible material behavior. The presentation closely follows that which is pursued in Section 4.3, and we repeat some of the equations for clarity and completeness. Let the prescribed values of tractions on the traction boundary Γ_t be $\bar{\mathbf{t}}$ and that on the essential boundary Γ_u be $\bar{\mathbf{u}}$ ($\Gamma = \Gamma_u \cup \Gamma_t$). We let $\boldsymbol{\sigma}$ be the Cauchy stress for a kinematically admissible displacement field $\mathbf{u}$, and $\mathbf{b}$ be the body force per unit volume. The strong form for the elastostatic boundary value problem is given by (Hughes, 1987)

$$\text{Given } \mathbf{b} : \Omega \times \Omega \to \mathbb{R}^2,\ \bar{\mathbf{u}} : \Gamma_u \times \Gamma_u \to \mathbb{R}^2,\ \text{and } \bar{\mathbf{t}} : \Gamma_t \times \Gamma_t \to \mathbb{R}^2$$

$$\text{Find } \mathbf{u} : \bar{\Omega} \times \bar{\Omega} \to \mathbb{R}^2,\ p : \bar{\Omega} \to \mathbb{R} \text{ such that}$$

$$\boldsymbol{\nabla} \cdot \boldsymbol{\sigma} + \mathbf{b} = 0 \quad \text{in } \Omega, \tag{6.6a}$$

$$\boldsymbol{\nabla} \cdot \mathbf{u} + \frac{p}{\lambda} = 0 \quad \text{in } \Omega, \tag{6.6b}$$

$$\mathbf{u} = \bar{\mathbf{u}} \quad \text{on } \Gamma_u, \tag{6.6c}$$

$$\boldsymbol{\sigma} \cdot \mathbf{n} = \bar{\mathbf{t}} \quad \text{on } \Gamma_t, \tag{6.6d}$$

where the Cauchy stress tensor $\boldsymbol{\sigma}$ is related to the small strain tensor $\boldsymbol{\varepsilon}$ and the pressure parameter p (hydrostatic pressure if $\nu = 0.5$) for an isotropic linear elastic material through the constitutive relation:

$$\sigma_{ij} = -p\delta_{ij} + \bar{C}_{ijkl}\varepsilon_{kl}, \tag{6.6e}$$

$$\bar{C}_{ijkl} = \mu(\delta_{ik}\delta_{jl} + \delta_{il}\delta_{jk}). \tag{6.6f}$$

In Eq. (6.6), λ and μ are Lamé parameters which for plane strain are defined as

$$\lambda = \frac{\nu E}{(1+\nu)(1-2\nu)}, \quad \mu = \frac{E}{2(1+\nu)}, \tag{6.7}$$

where ν is the Poisson's ratio. The kinematic relation between the small strain tensor $\boldsymbol{\varepsilon}$ and the displacement vector $\mathbf{u}$ is

$$\boldsymbol{\varepsilon} = \frac{1}{2}\left(\boldsymbol{\nabla}\mathbf{u} + (\boldsymbol{\nabla}\mathbf{u})^T\right). \tag{6.8}$$

6.3.2 Weak Form

We first define the trial and test spaces for the displacements and the pressure. Following Hughes (1987), we let

$$\mathbf{u} \in \mathbf{V} = (H^1(\Omega))^2 \quad \text{(displacement trial solution space)}, \tag{6.9a}$$

$$\mathbf{v} \in \mathbf{V}_0 = (H_0^1(\Omega))^2 \quad \text{(displacement test function space)}, \tag{6.9b}$$

$$p,\, q \in P = L^2(\Omega) \quad \text{(space of pressures—trial and test functions)}, \tag{6.9c}$$

where the Sobolev spaces $H^1(\Omega)$ and $H_0^1(\Omega)$ are defined in Section 2.1.1.

Let $(\mathbf{u}, p) \in \mathbf{V} \times P$ be the trial function pair, and $(\mathbf{v}, q) \in \mathbf{V}_0 \times P$ the corresponding test functions. On taking the product of Eq. (6.6a) with v_i and Eq. (6.6b) with q, and then integrating their sum over the domain Ω, we obtain

$$\underbrace{\int_\Omega \sigma_{ji,j} v_i \, d\Omega + \int_\Omega b_i v_i \, d\Omega}_{(A)} + \int_\Omega \left(u_{k,k} + \frac{p}{\lambda} \right) q \, d\Omega = 0, \tag{6.10}$$

and on using Eq. (4.10) for the integrals marked by (A), we obtain

$$-\int_\Omega \sigma_{ij}(\mathbf{u}) \varepsilon_{ij}(\mathbf{v}) \, d\Omega + \int_\Omega b_i v_i \, d\Omega + \int_{\Gamma_t} \bar{t}_i v_i \, d\Gamma + \int_\Omega u_{k,k} q \, d\Omega + \frac{1}{\lambda} \int_\Omega pq \, d\Omega = 0. \tag{6.11}$$

Now, on using the constitutive equation given in Eqs. (6.6e) and (6.6f), we can write the above equation as

$$\begin{aligned} 2\mu \int_\Omega \varepsilon_{ij}(\mathbf{u}) \varepsilon_{ij}(\mathbf{v}) \, d\Omega - \int_\Omega p v_{k,k} \, d\Omega - \int_\Omega u_{k,k} q \, d\Omega - \frac{1}{\lambda} \int_\Omega pq \, d\Omega \\ = \int_\Omega b_i v_i \, d\Omega + \int_{\Gamma_t} \bar{t}_i v_i \, d\Gamma, \end{aligned} \tag{6.12}$$

and since the test functions v_i and q are independent and arbitrary, we obtain the Hermann variational (weak) form, which is posed as (Hermann, 1965; Hughes, 1987):

Find $(\mathbf{u}, p) \in \mathbf{V} \times P$ such that

$$\bar{a}(\mathbf{u}, \mathbf{v}) + b(\mathbf{v}, p) = \langle \mathbf{b}, \mathbf{v} \rangle + \langle \bar{\mathbf{t}}, \mathbf{v} \rangle \quad \forall \ \mathbf{v} \in \mathbf{V}_0, \tag{6.13a}$$

$$b(\mathbf{u}, q) - \frac{1}{\lambda}(p, q) = 0 \quad \forall \ q \in P, \tag{6.13b}$$

where

$$\bar{a}(\mathbf{u},\mathbf{v}) = 2\mu \int_\Omega \varepsilon_{ij}(\mathbf{u})\varepsilon_{ij}(\mathbf{v})\, d\Omega, \tag{6.13c}$$

$$b(\mathbf{v},p) = -\int_\Omega p\boldsymbol{\nabla}\cdot\mathbf{v}\, d\Omega. \tag{6.13d}$$

In a displacement-pressure mixed formulation for linear elasticity, the bilinear form $\bar{a}(\mathbf{u},\mathbf{v}) : \mathbf{V}\times\mathbf{V}_0 \to \mathbb{R}$ is symmetric, bounded, and positive definite. Hence, for the displacement-pressure pair $(\mathbf{u},p)$ to be the unique solution to the system in Eq. (6.13), the bilinear form $b(\mathbf{v},p) : \mathbf{V}_0\times P \to \mathbb{R}$ must satisfy the LBB stability condition (Brezzi and Fortin, 1991):

$$\inf_{p\in P}\sup_{\mathbf{v}\in\mathbf{V}_0}\frac{|b(\mathbf{v},p)|}{||\mathbf{v}||\mathbf{v}||p||_P} \geq \beta > 0, \tag{6.14}$$

where β is a constant.

In the numerical implementation, finite-dimensional subspaces are used as the trial and test spaces for the displacements and pressure. Let $\mathbf{V}^h \subset \mathbf{V}$ and $\mathbf{V}_0^h \subset \mathbf{V}_0$ be the trial and test spaces for the displacements, and $P^h \subset P$ be the trial and test space for the pressure. The weak form for NEM can be written as

Find $(\mathbf{u}^h, p^h) \in \mathbf{V}^h \times P^h$ such that

$$\bar{a}(\mathbf{u}^h,\mathbf{v}^h) + b(\mathbf{v}^h,p^h) = \langle\mathbf{b},\mathbf{v}^h\rangle + \langle\bar{\mathbf{t}},\mathbf{v}^h\rangle \quad \forall\ \mathbf{v}^h \in \mathbf{V}_0^h, \tag{6.15a}$$

$$b(\mathbf{u}^h,q^h) - \frac{1}{\lambda}(p^h,q^h) = 0 \quad \forall\ q^h \in P^h. \tag{6.15b}$$

The LBB stability condition for the discrete problem is similar to Eq. (6.14), with

the trial and test functions in the continuous space being replaced by their discrete counterparts.

6.3.3 Discrete System for NEM

Consider the numerical implementation for the mixed natural element method. In a Galerkin procedure, the displacement trial and test functions are interpolated using the same set of shape functions and likewise for the pressure trial and test functions. The trial and test functions are:

$$\mathbf{u}^h(\mathbf{x}) = \sum_{I=1}^{n} \phi_I(\mathbf{x})\mathbf{u}_I, \quad \mathbf{v}^h(\mathbf{x}) = \sum_{I=1}^{n} \phi_I(\mathbf{x})\mathbf{v}_I, \tag{6.16a}$$

$$p^h(\mathbf{x}) = \sum_{I=1}^{n} \psi_I(\mathbf{x})\bar{p}_I, \quad q^h(\mathbf{x}) = \sum_{I=1}^{n} \psi_I(\mathbf{x})\bar{q}_I. \tag{6.16b}$$

The strain-displacement relation for the displacement trial function can be written as

$$\boldsymbol{\varepsilon}^h(\mathbf{x}) = \sum_{I=1}^{n} \mathbf{B}_I\mathbf{u}_I, \tag{6.17}$$

where

$$\mathbf{B}_I = \begin{bmatrix} \phi_{I,1}(\mathbf{x}) & 0 \\ 0 & \phi_{I,2}(\mathbf{x}) \\ \phi_{I,2}(\mathbf{x}) & \phi_{I,1}(\mathbf{x}) \end{bmatrix}. \tag{6.18}$$

The divergence of the displacement trial solution is given by

$$\boldsymbol{\nabla} \cdot \mathbf{u}^h(\mathbf{x}) = \sum_{I=1}^{n} \tilde{\mathbf{B}}_I \mathbf{u}_I, \tag{6.19}$$

where

$$\tilde{\mathbf{B}}_I = \begin{bmatrix} \phi_{I,1}(\mathbf{x}) & \phi_{I,2}(\mathbf{x}) \end{bmatrix}. \tag{6.20}$$

On substituting the displacement and pressure trial and test functions in Eq. (6.15) and using the arbitrariness of displacement and pressure nodal variations, the following discrete system of linear equations is obtained (Hughes, 1987):

$$\begin{bmatrix} \bar{\mathbf{K}} & \mathbf{G} \\ \mathbf{G}^T & \mathbf{M} \end{bmatrix} \begin{Bmatrix} \mathbf{d} \\ \mathbf{p} \end{Bmatrix} = \begin{Bmatrix} \mathbf{f} \\ \mathbf{0} \end{Bmatrix}, \tag{6.21}$$

where

$$\bar{\mathbf{K}}_{IJ} = \int_{\Omega^h} \mathbf{B}_I^T \bar{\mathbf{C}} \mathbf{B}_J \, d\Omega, \tag{6.22a}$$

$$\mathbf{G}_{IJ} = -\int_{\Omega^h} \tilde{\mathbf{B}}_I^T \psi_J \, d\Omega, \tag{6.22b}$$

$$\mathbf{M}_{IJ} = -\frac{1}{\lambda} \int_{\Omega^h} \psi_I \psi_J \, d\Omega, \tag{6.22c}$$

$$\mathbf{f}_I = \int_{\Omega^h} \phi_I \mathbf{f} \, d\Omega + \int_{\Gamma_t^h} \phi_I \bar{\mathbf{t}} \, d\Gamma. \tag{6.22d}$$

In the above equations, $\mathbf{d}$ is the vector of nodal displacements and $\mathbf{p}$ is the vector of nodal pressures. The matrix $\bar{\mathbf{K}}$ is symmetric and positive definite, and the matrix $\mathbf{M}$ is symmetric and negative definite ($\mathbf{M} = \mathbf{0}$ when $\nu = 0.5$). The matrix $\mathbf{G}$ corresponds

to the discrete gradient operator, and $\mathbf{G}^T$ to the discrete divergence operator.

6.4 Numerical Results and Discussions

The application of the mixed natural element method to problems in small displacement compressible as well as near incompressible two-dimensional elastostatics, in the absence of body forces, is presented. In the computations, numerical integration is carried out using symmetric quadrature rules for a triangle (Dunavant, 1985). Three point quadrature rule is used in the numerical integration of the weak form; the error norm computations are carried out using 25 point quadrature rule in each triangle.

6.4.1 Cantilever Beam

In Fig. 4.10, a cantilever beam subjected to a parabolic end load is illustrated. The beam has length L, height D, and unit thickness. The problem description and illustration for this problem are given in Section 4.4.4. The displacement vector solution and the exact stresses are given in Eqs. (4.28) and (4.30). In the numerical model, the analytical displacement solution from Eq. (4.28) is prescribed on the boundary Γ_u: $x_1 = 0$, $-D/2 \leq x_2 \leq D/2$ (Fig. 4.10). On the remaining boundaries, exact tractions are specified. The following parameters are used in the numerical computations: $P = -1000$ lb, $D = 1$ in., $L = 4$ in., $E = 3 \times 10^7$ psi, and plane strain conditions are assumed.

The mixed natural element displacement-pressure formulation is applied to both the compressible and near incompressible cases. The numerical computations are carried out using four different nodal discretizations, namely 85 nodes, 297 nodes,

1105 nodes, and 1701 nodes. Equal nodal spacing in the x_1- and x_2-direction is used in each of the above grids. A sample nodal discretization (85 nodes) is shown in Fig. 4.11. In Table 6.1, the normalized end displacement $\big(u_2^h(4,0)/u_2(4,0)\big)$ is presented for varying Poisson's ratio using FEM, C^0 NEM, and the mixed formulation. The results presented in Table 6.1 are for the nodal discretization shown in Fig. 4.11. Bilinear quadrilateral elements with 3×3 Gauss quadrature are used in the finite element computations, and three point symmetric quadrature rule over triangles is used in the NEM computations. Clearly, severe locking is observed for both, FEM and NEM as $\nu \to 0.5$; the mixed C^0–C^0 method does lock to some degree, but the mixed C^0–C^{-1} method does seem to alleviate locking as the incompressible limit is approached. The results for the mixed C^0–C^{-1} formulation are accurate for the entire range of values of ν.

A convergence study for the cantilever beam problem is carried out. We define the $L^2(\Omega)$ and energy error norms used in the analysis as:

$$\|\mathbf{u} - \mathbf{u}^h\|_{L^2(\Omega)} = \Big(\big(\mathbf{u} - \mathbf{u}^h, \mathbf{u} - \mathbf{u}^h\big)\Big)^{1/2}, \tag{6.23a}$$

$$\|\mathbf{u} - \mathbf{u}^h\|_{E(\Omega)} = \left(\frac{1}{2} a\big(\mathbf{u} - \mathbf{u}^h, \mathbf{u} - \mathbf{u}^h\big)\right)^{1/2}, \tag{6.23b}$$

where

$$a(\mathbf{u}, \mathbf{u}) = 2\mu\big(\boldsymbol{\varepsilon}(\mathbf{u}), \boldsymbol{\varepsilon}(\mathbf{u})\big) + (p, \operatorname{div} \mathbf{u}). \tag{6.23c}$$

In Figures 6.1 and 6.2, the relative displacement and energy error norms are plotted against the nodal spacing h on a log-log plot. Results are presented for the mixed

Table 6.1: Normalized end displacement for the cantilever beam problem.

ν	FEM	NEM		
	(3×3)	C^0	Mixed (C^0–C^0)	Mixed (C^0–C^{-1})
0.3	0.9651	0.9692	0.9739	0.9903
0.4	0.9373	0.9436	0.9676	0.9924
0.4999	0.1873	0.1950	0.9495	0.9901
0.4999999	0.1775	0.2103	0.9490	0.9903

C^0–C^0 displacement-pressure and C^0–C^{-1} displacement-pressure formulations. The error norm computations are carried out for three different values of the Poisson's ratio: $\nu = 0.3$, $\nu = 0.4$, and $\nu = 0.4999$ (near incompressibility). The rate of convergence is denoted by the value of R. The results indicate that optimal convergence in displacement and energy is attained for all three values of ν. The absolute accuracy of the C^0–C^{-1} formulation is better than that obtained for the C^0–C^0 formulation.

The pressure computations are carried out along the mid-section of the beam using the mixed C^0–C^0 and C^0–C^{-1} methods. The results are computed at 100 equi-distant points between $y = -0.5$ in. and $y = 0.5$ in. In Fig. 6.3, the variation of the pressure parameter p for the 85 node grid is shown for the compressible case ($\nu = 0.3$). The

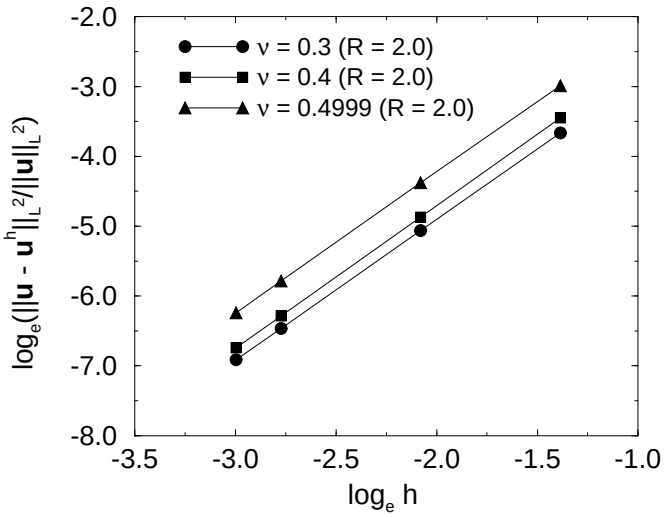

(a)

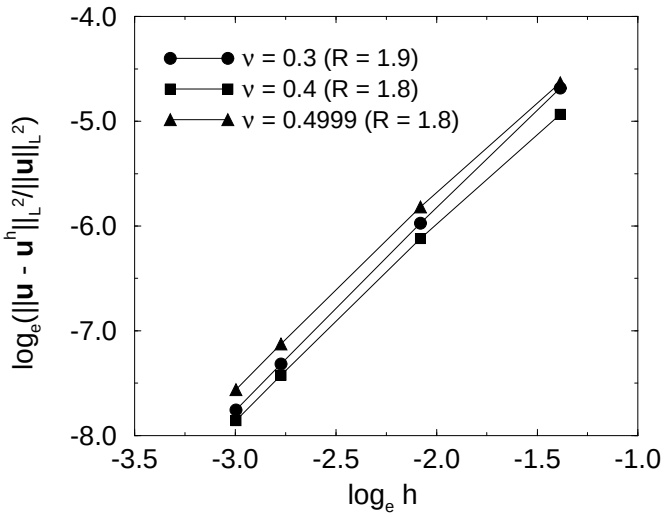

(b)

Figure 6.1: Rate of convergence in displacement for the cantilever beam problem. (a) C^0–C^0 method, and (b) C^0–C^{-1} method.

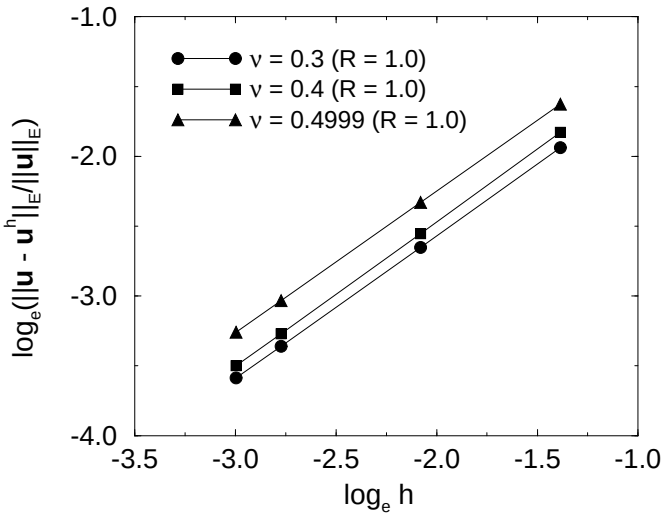

(a)

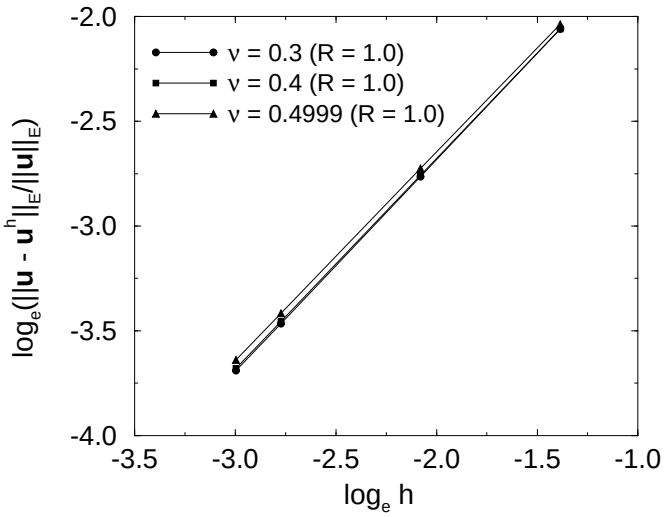

(b)

Figure 6.2: Rate of convergence in energy for the cantilever beam problem. (a) C^0–C^0 method, and (b) C^0–C^{-1} method.

pressure parameter p is given by

$$p = \frac{-\sigma_{kk} + 2\mu\varepsilon_{kk}}{3}, \tag{6.24}$$

and hence in the incompresssible limit (div $\mathbf{u} = \varepsilon_{kk} = 0$), p is the hydrostatic pressure. In Fig. 6.4, the hydrostatic pressure is plotted for the near incompressible case (85 and 1701 nodal grids). The pressure oscillation for the C^0–C^0 method are fairly pronounced, while the results for the C^0–C^{-1} method are less oscillatory.

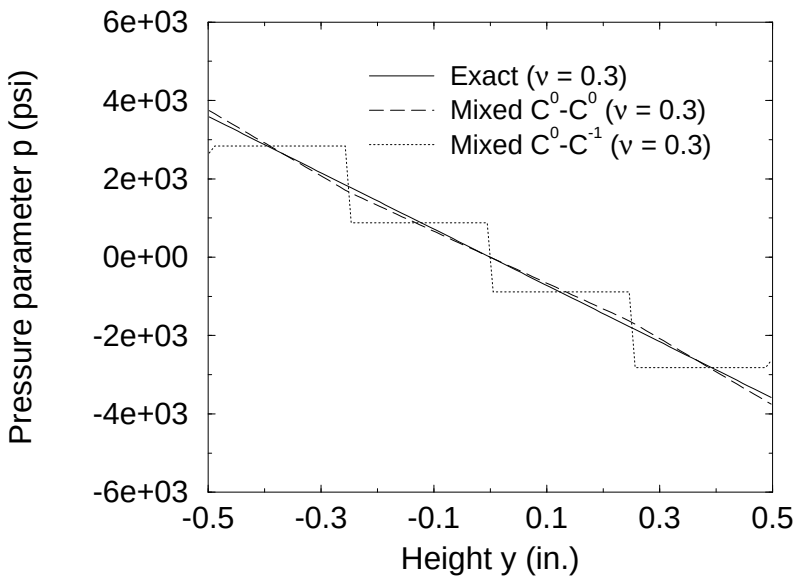

Figure 6.3: Variation of the pressure parameter p for the beam model.

6.4.2 Infinite Plate with a Circular Hole

In order to test the accuracy of the mixed formulation in near incompressible elasticity, it is imperative that we also study its performance for non-uniform nodal discretiza-

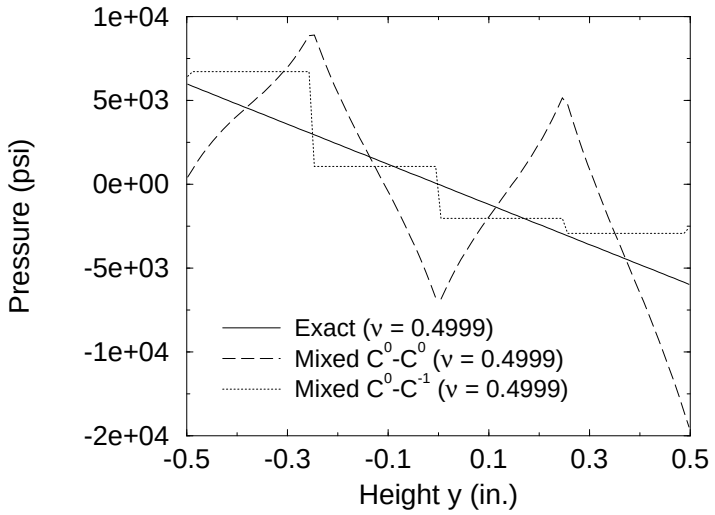

(a)

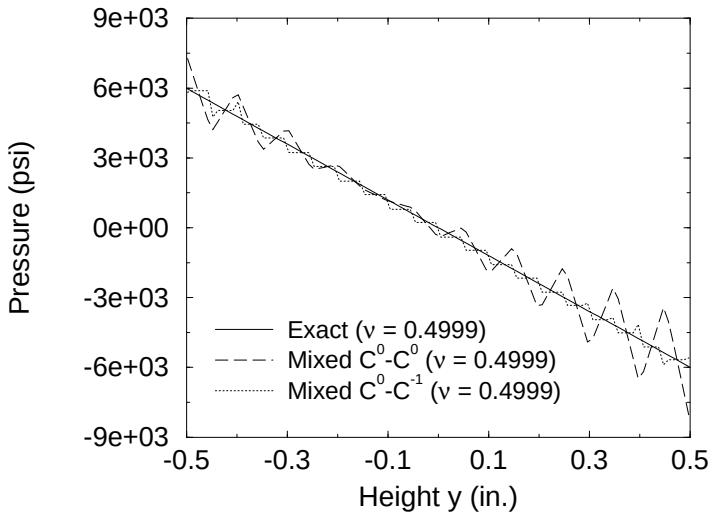

(b)

Figure 6.4: Variation of hydrostatic pressure for the beam model. (a) 85 nodes, and (b) 1701 nodes.

tions. We consider the problem of an infinite plate with a traction free circular hole under unidirectional tension along the x_1-direction (Fig. 4.6). The illustration of the model problem, with a description of the essential and traction boundary conditions is discussed in Section 4.4.3. The exact stress solution is given in Eq. (4.25) and the exact displacement components are presented in Eq. (4.26).

In the numerical computations, $a = 1$ in., $L = 5$ in., and plane strain conditions are assumed. The mixed natural element displacement-pressure formulation is applied to both the compressible and near incompressible cases. A convergence study is carried out using four different nodal discretizations (Fig. 4.7). The $L^2(\Omega)$ and energy error norms used in the computations are defined in Eq. (6.23). In Figures 6.5 and 6.6, the relative displacement and energy error norms are plotted against the square root of the number of nodes on a log-log plot. Results are presented for the mixed C^0–C^0 displacement-pressure and C^0–C^{-1} displacement-pressure formulations. The error norm computations are carried out for three different values of the Poisson's ratio: $\nu = 0.3$, $\nu = 0.4$, and $\nu = 0.4999$ (near incompressibility). The convergence rates which are denoted by R are indicated on the plots. The results indicate that near optimal convergence in displacement and energy is attained for all three values of ν. The absolute accuracy of the C^0–C^{-1} formulation is better than that obtained for the C^0–C^0 formulation; the relative error norms using the mixed C^0–C^{-1} method are independent of the Poisson's ratio ν.

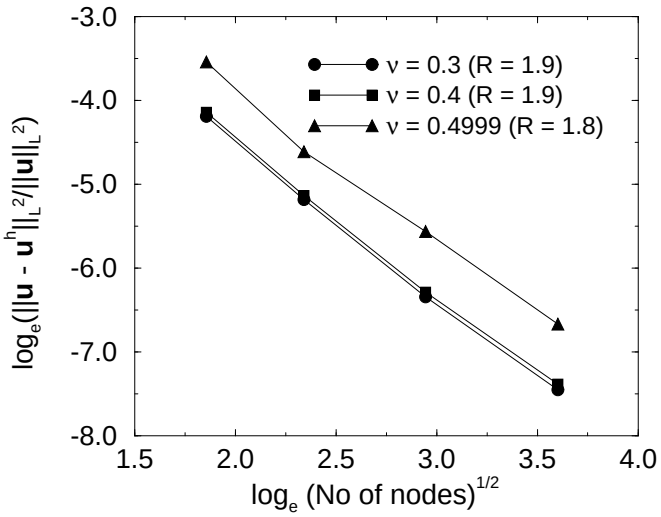

(a)

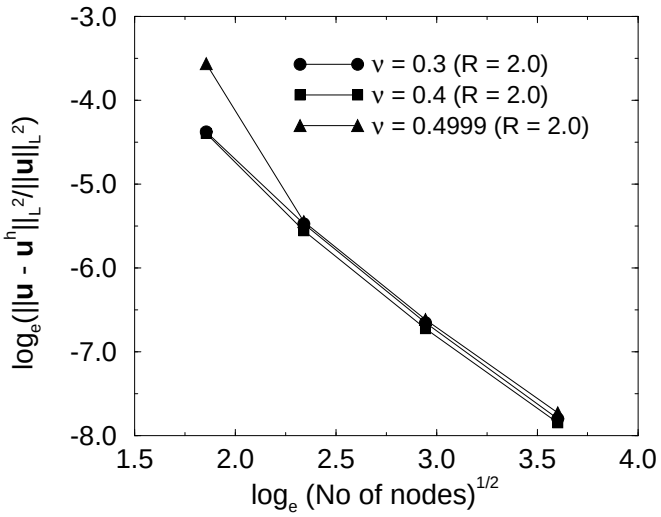

(b)

Figure 6.5: Rate of convergence in displacement for the plate with a hole problem. (a) C^0–C^0 method, and (b) C^0–C^{-1} method.

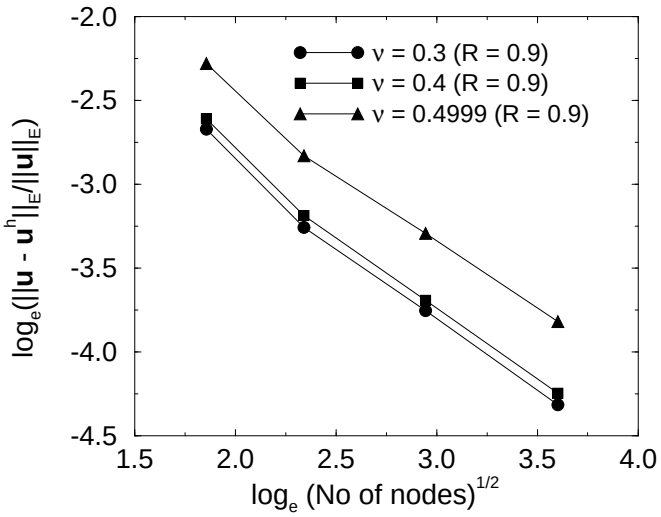

(a)

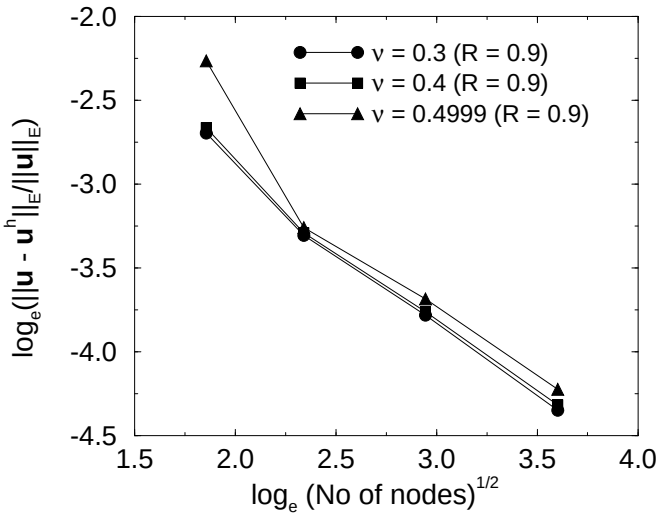

(b)

Figure 6.6: Rate of convergence in energy for the plate with a hole problem. (a) C^0–C^0 method, and (b) C^0–C^{-1} method.

Chapter 7

Conclusions

In this thesis, the application of the Natural Element Method (NEM) to elliptic boundary value problems in two-dimensional solid mechanics is explored. In NEM, the interpolants used to construct the trial and test functions are known as natural neighbor (n-n) interpolants. These interpolants are based on the Dirichlet or Voronoi tessellation of a set (N) of distinct nodes in the plane. The Voronoi tessellation is a unique and geometrically fundamental construct that defines a set of nodes. Natural neighbor interpolants have optimum spatial adjacency properties, and are sensitive to the position and the density of nodes. Natural neighbor interpolants are smooth (C^∞) everywhere, except at the nodes where they are C^0. In one-dimension, C^0 NEM interpolation is identical to linear finite elements. In the natural element method, natural neighbor interpolants are used as the trial and test functions. In two-dimensions, one way to approach the computation of natural neighbor shape functions is to calculate the areas of polygons that are obtained as the solution to a constrained linear programming problem (Lasserre, 1983). An alternate approach due to Watson (1994) for natural neighbor shape function computations was used in this thesis. The computational algorithm is based on the signed summation of areas

formed by the vertices of natural neighbor circumcircles and the point $\mathbf{x}$ in the plane. A displacement-based Bubnov-Galerkin procedure was used to obtain the discrete equations in the natural element method.

The application of the C^0 natural element element to problems in two-dimensional elasticity was studied, and comparisons made to results obtained using constant strain finite elements as well as to reference solutions to validate the accuracy and convergence of the numerical method. First, an eigenanalysis was carried out to ascertain the properties of the C^0 NEM approximation spaces. Numerical results for the eigenproblem indicated that the C^0 NEM interpolant was linearly independent for both, uniform and non-uniform nodal discretizations. The condition numbers of the mass matrices using NEM were comparable to those obtained using constant strain finite elements. In the patch tests, issues pertaining to the accurate integration of the weak form were raised. Benchmark problems, such as the cantilever beam, plate with a hole, and hollow cylinder under internal pressure, which have gradients in the strain and stress solutions were solved. The numerical results were in excellent agreement with exact and analytical solutions for these problems. The ability to model material discontinuities was illustrated by solving the bi-material problem of an inclusion with a constant eigenstrain, embedded in an infinite matrix. The numerical results showed good agreement with the exact solution. The modeling of non-convex bodies, such as two-dimensional bodies with crack surfaces, was also described. The benchmark problem of an edge-crack under mode I loading was considered to test the accuracy of NEM in stress intensity factor computations. The stress intensity factors computed using NEM were within 0.3% of the reference solution, and very good domain independence was achieved.

The construction of conforming (C^k, $k > 0$) finite element spaces for $2m$ ($m > 1$) order elliptic PDEs is a non-trivial task. A desirable property of such approximation spaces in a Galerkin setting is that they interpolate nodal data for all gradients less than order m. This facilitates the imposition of essential boundary conditions by setting the appropriate nodal variables to the imposed essential boundary data. In light of the above, the C^1 natural neighbor interpolant proposed by Farin (1990b) is an attractive choice. Farin (1990b) has developed a C^1 interpolant by embedding Sibson's coordinate (Sibson, 1980) in the Bernstein-Bézier surface representation of a cubic simplex. The C^1 NEM interpolant that we proposed was constructed by a suitable transformation of Bernstein basis functions that appear in Farin's C^1 interpolant. This transformation resulted in the representation of the interpolant in terms of nodal function and nodal gradient values, which rendered it amenable to use in a Galerkin scheme for the solution of PDEs. The C^1 NEM interpolant has quadratic completeness, interpolates to nodal function and nodal gradient values, and reduces to a cubic polynomial on the boundary of the domain. In one-dimension, C^1 NEM interpolation is identical to cubic Hermite finite elements. In the application to the biharmonic equation, a standard Bubnov-Galerkin procedure was used to obtain the discrete equations. In the patch test for the biharmonic operator, issues pertaining to the accurate integration of the weak form were raised. Excellent agreement with the exact solution for the uniformly loaded clamped circular plate was obtained, and convergence to the exact center displacement was monotonic with nodal refinement. Issues pertaining to stability were probed by carrying out an eigenanalysis. Numerical results showed that the mass matrix was not well-conditioned. The satisfaction of the ellipticity condition was met, with the ellipticity constant α being the funda-

mental frequency of the clamped plate. This established the stability of the discrete biharmonic operator. The C^1 NEM results for the fundamental frequency matched the reference solution for the clamped plate problem. In this context, a potential application of the C^1 NEM interpolant is in the numerical computation of natural modes and frequencies of plates.

A mixed formulation for the natural element method in linear elastostatics was presented. A displacement-pressure mixed formulation was adopted with displacements interpolated by C^0 natural neighbor interpolants; C^0 and C^{-1} interpolation schemes were considered for the interpolation of the pressure. The mixed C^0-C^{-1} NEM method removed locking in the near incompressible limit ($\nu \to 0.5$) for the elastostatic boundary value problem; moreover, convergence rates in displacement and energy were optimal for all $\nu \in [0, 0.5)$. Numerical results for the beam in bending and for a plate with a circular hole under tension were obtained. Excellent agreement with analytical and exact solutions was obtained for problems in compressible and near incompressible media.

The computational time and costs incurred in the implementation and execution of any numerical method is a critical component in the evaluation of its feasibility, usability, and potential for mid- to large-scale applications. In the natural element method, natural neighbor coordinates are used to construct the approximation spaces. The numerical computation of the NEM interpolant is based on well-established computational geometric algorithms with optimum time-complexity. The timings involved in evaluating natural neighbor shape functions are only about twice that of constant strain finite elements. The computational costs of the C^1 natural element method are more than its C^0 variant. The increased costs are primarily due to the fact

that three degrees of freedom are associated with each node; the C^1 interpolating functions require basic linear algebra matrix-vector operations and the costs are not significantly more than those incurred in the evaluation of C^0 natural neighbor interpolants. The above facts and observations do indicate that, both the C^0 and C^1 variants of NEM are very feasible and attractive choices from the computational cost and time viewpoint.

In this thesis, various applications of the natural element method were developed and applied to elliptic boundary value problems in solid mechanics. The numerical results demonstrated the capabilities, versatility, accuracy, and robustness of the numerical method, and indicate that the natural element method is a promising numerical tool in the realm of *meshless methods* to solve boundary value problems of mathematical physics.

References

Adams, R. A. (1975). *Sobolev Spaces.* New York: Academic Press.

Agmon, S. (1965). *Lectures on Elliptic Boundary Value Problems.* New Jersey: Van Nostrand.

Ahuja, N. (1982). Dot pattern processing using Voronoi polygons as neighborhoods. *IEEE Trans. Pattern Anal. Mach. Intell. 4*, 336–343.

Alfeld, P. (1984). A bivariate C^2 Clough-Tocher scheme. *Computer Aided Geometric Design 1*, 257–267.

Alfeld, P. (1989). Scattered data interpolation in three or more variables. In T. Lyche and L. L. Schumaker (Eds.), *Mathematical Methods in Computer Aided Geometric Design*, San Diego, pp. 1–34. Academic Press.

Arnold, D. N. (1990). Mixed finite element methods for elliptic problems. *Computer Methods in Applied Mechanics and Engineering 82*, 281–300.

Aurenhammer, F. (1996). Voronoi diagrams — a survey of a fundamental geometric data structure. *ACM Transactions on Mathematical Software 23*, 469–483.

Babuška, I. (1971). Error bounds for finite element method. *Numer. Math. 16*, 322–333.

Babuška, I. and A. Aziz (1976). On the angle condition in the finite element method. *SIAM J. Numer. Analysis 13*, 214–227.

Babuška, I. and M. Suri (1992). Locking effects in the finite element aproximation of elasticity problems. *Numer. Math. 62*, 439–463.

Babuška, I. and Z. Zhang (1998). The partition of unity method for the elastically supported beam. *Computer Methods in Applied Mechanics and Engineering 152*, 1–18.

Barber, C. B., D. P. Dobkin, and H. T. Huhdanpaa (1996). The Quickhull algorithm for convex hull. *ACM Transactions on Mathematical Software 22*, 469–483.

Barber, C. B. and H. T. Huhdanpaa (1994). *Qhull (Computer Program)*. The Geometry Center, University of Minnesota, 1300 South Second Street, Minneapolis, MN 55454: Available at `http://www.geom.umn.edu/software/qhull/`.

Bazeley, G. R., Y. K. Cheung, B. M. Irons, and O. C. Zienkiewicz (1965). Triangular elements in plate bending. Conforming and non-conforming solutions. In *Proceedings of the 1st Conference on Matrix Methods in Structural Mechanics*, Wright-Patterson AFB.

Bell, K. (1969). A refined triangular plate bending finite element. *International Journal for Numerical Methods in Engineering 1*, 101–122.

Belytschko, T., Y. Krongauz, D. Organ, M. Fleming, and P. Krysl (1996). Meshless methods: An overview and recent developments. *Computer Methods in Applied Mechanics and Engineering 139*, 3–47.

Belytschko, T., Y. Y. Lu, and L. Gu (1994). Element-free Galerkin methods. *International Journal for Numerical Methods in Engineering 37*, 229–256.

Bern, M. and D. Eppstein (1995). Mesh generation and optimal triangulation. In D.-Z. Du and F. K. Hwang (Eds.), *Computing in Euclidean Geometry*, Volume 1 of *Lecture Notes Series on Computing*, pp. 23–90. Singapore: World Scientific.

Bernal, M. J. M. and J. R. Whiteman (1970). Numerical treatment of biharmonic boundary value problems with re-entrant boundaries. *The Computer Journal 13*(1), 87–91.

Böhm, W., G. Farin, and J. Kahmann (1984). A survey of curve and surface methods in CAGD. *Computer Aided Geometric Design 1*, 1–60.

Boots, B. N. (1986). *Voronoi (Thiessen) Polygons*. Norwich, UK: Geo Books.

Borgers, C. (1990). Generalized Delaunay triangulations of nonconvex domains. *Comput. Math. Appl. 20*(7), 45–49.

Bowyer, A. (1981). Computing Dirichlet tessellations. *Computer J. 24*, 162–166.

Braess, D. (1997). *Finite Elements*. Cambridge, UK: Cambridge University Press.

Braun, J. and M. Sambridge (1995). A numerical method for solving partial differential equations on highly irregular evolving grids. *Nature 376*, 655–660.

Braun, J., M. Sambridge, and H. McQueen (1995). Geophysical parameterization and interpolation of irregular data using natural neighbors. *Geophysical Journal International 122*, 837–857.

Brezzi, F. (1974). On the existence, uniqueness and approximation of saddle-point problems arising from Lagrange multipliers. *RAIRO Anal. Numér. 8*, 129–151.

Brezzi, F. and M. Fortin (1991). *Mixed and Hybrid Finite Element Methods.* New York: Springer-Verlag.

Brown, J. L. (1994). Natural neighbor interpolation on the sphere. In P. J. Laurent, A. L. Méhauté, and L. L. Schumaker (Eds.), *Wavelets, Images and Surface Fitting*, Wellesley, MA, pp. 67–74. Peters, A. K.

Brown, K. Q. (1979). Voronoi diagrams from convex hulls. *Inform. Process. Lett. 9*, 223–228.

Chilton, L. and M. Suri (1997). On the selection of a locking-free *hp* element for elasticity problems. *International Journal for Numerical Methods in Engineering 40*, 2045–2062.

Chu, Y. A. and B. Moran (1995). A computational model for nucleation of solid-solid phase transformations. *Modelling Simul. Mater. Sci. Eng. 3*, 455–471.

Ciarlet, P. G. (1978). *The Finite Element Methods for Elliptic Problems.* Amsterdam: North-Holland.

Clough, R. and J. L. Tocher (1965). Finite element stiffness matrices for analysis of plates in bending. In *Proceedings of the 1st Conference on Matrix Methods in Structural Mechanics*, Wright-Patterson AFB.

Cools, R., D. Laurie, and L. Pluym (1997). Algorithm 764: Cubpack++: A C++ package for automatic two-dimensional cubature. *ACM Transaction of Mathematical Software 19*, 309–326.

Cools, R. and P. Rabinowitz (1997). Monomial cubature rules since 'Stroud': A compilation. *Journal of Computational and Applied Mathematics 23*, 1–15.

Cordes, L. W. and B. Moran (1996). Treatment of material discontinuity in the element-free Galerkin method. *Computer Methods in Applied Mechanics and Engineering 139*, 75–89.

de Boor, C. (1987). B-form basics. In G. Farin (Ed.), *Geometric Modeling: Algorithm and New Trends*, SIAM, Philadelphia, PA, pp. 131–148.

de Veubeke, C. (1968). A conforming finite element for plate bending. *International Journal for Solids and Structures 4*, 95–108.

Delaunay, B. (1934). Sur la sphère vide. A la memoire de Georges Voronoi. *Izv. Akad. Nauk SSSR, Otdelenie Matematicheskih i Estestvennyh Nauk 7*, 793–800.

Donning, B. (1997). Meshless methods for shear-deformable beams and plates. Master's thesis, Northwestern University.

Duarte, C. A. and J. T. Oden (1996). An *H-p* adaptive method using clouds. *Computer Methods in Applied Mechanics and Engineering 139*, 237–262.

Dunavant, D. A. (1985). High degree efficient symmetrical Gaussian quadrature rules for the triangle. *International Journal for Numerical Methods in Engineering 21*, 1129–1148.

Farin, G. (1983). Smooth interpolation to scattered 3D data. In R. E. Barnhill and W. Böhm (Eds.), *Surfaces in CAGD*, Amsterdam, pp. 43–63. North-Holland.

Farin, G. (1985). A modified Clough-Tocher interpolant. *Computer Aided Geometric Design 2*, 19–27.

Farin, G. (1986). Triangular Bernstein-Bézier patches. *Computer Aided Geometric Design 3*, 83–127.

Farin, G. (1990a). *Curves and Surfaces for Computer Aided Geometric Design: A Practical Guide* (Second ed.). New York: Academic Press.

Farin, G. (1990b). Surfaces over Dirichlet tessellations. *Computer Aided Geometric Design 7*(1–4), 281–292.

Felippa, C. A., B. Haugen, and C. Militello (1995). From the individual element test to finite element templates: Evolution of the patch test. *International Journal for Numerical Methods in Engineering 38*, 199–229.

Fortune, S. (1987). A sweepline algorithm for Voronoi diagrams. *Algorithmica 2*, 153–174.

Fortune, S. (1995). Voronoi diagrams and Delaunay triangulations. In D.-Z. Du and F. K. Hwang (Eds.), *Computing in Euclidean Geometry*, Volume 1 of *Lecture Notes Series on Computing*, pp. 193–233. Singapore: World Scientific.

Gingold, R. A. and J. J. Monaghan (1977). Smoothed particle hydrodynamics: Theory and application to non-spherical stars. *Monthly Notices of the Royal Astronomical Society 181*, 375–389.

Gold, C. M. (1989). Surface interpolation, spatial adjacency and GIS. In J. Raper (Ed.), *Three Dimensional Applications in Geographical Information Systems*, London, pp. 21–35. Taylor and Francis.

Green, P. J. and R. R. Sibson (1978). Computing Dirichlet tessellations in the plane. *The Computer Journal 21*, 168–173.

Gregory, J. A., D. Fishelov, B. Schiff, and J. R. Whiteman (1978). Local mesh refinement with finite elements for elliptic problems. *Journal of Computational Physics 29*, 133–140.

Hardy, R. L. (1971). Multiquadric equations of topography and other irregular surfaces. *Journal of Geophysical Research 76*, 1905–1915.

Hein, P. (1993). Diffuse element method applied to Kirchhoff plates. Technical report, Department of Civil Engineering, Northwestern University.

Hermann, L. R. (1965). Elasticity equations for incompressible and nearly incompressible materials by a variational theorem. *AIAA Journal 3*, 1896–1900.

Hughes, T. J. R. (1987). *The Finite Element Method.* Englewood Cliffs, N.J.: Prentice-Hall.

Irons, B. (1969). A conforming quartic triangular element for plate bending. *International Journal for Numerical Methods in Engineering 1*, 29–45.

Irons, B. M. and A. Razzaque (1972). Experience with the patch test for convergence of finite elements. In A. K. Aziz (Ed.), *The Mathematical Foundations of the Finite Element Method with Applications to Partial Differential Equations*, New York. Academic Press.

Jones, N. L., S. J. Owens, and E. C. Perry (1995). Plume characterization with natural neighbor interpolation. In *Proceedings GEOENVIRONMENT 2000, Geotechnical Engineering and Environmental Engineering Divisions/ASCE*, New York, N.Y., pp. 331–345.

Krysl, P. and T. Belytschko (1996). Analysis of thin plates by the element-free Galerkin method. *Computational Mechanics 17*, 26–35.

Ladyzhenskaya, O.-A. (1969). *The Mathematical Theory of Viscous Flow* (Second ed.). New York: Gordon and Breach.

Lancaster, P. and K. Salkauskas (1981). Surfaces generated by moving least squares methods. *Mathematics of Computation 37*, 141–158.

Landau, L. D. and E. M. Lifschitz (1970). *Theory of Elasticity* (Second ed.). Oxford: Pergamon Press.

Lasserre, J. B. (1983). An analytical expression and an algorithm for the volume of a convex polyhedron in R^n. *Journal of Optimization Theory and Applications 39*(3), 363–377.

Lawson, C. L. (1977). Software for C^1 surface interpolation. In J. R. Rice (Ed.), *Mathematical Software III*, Volume 3, New York, N.Y. Academic Press.

Lee, D. T. and B. J. Schachter (1980). Two algorithms for constructing a Delaunay triangulation. *Internat. J. Comput. Inform. Sci. 9*, 219–242.

Leissa, A. W. (1969). *Vibration of Plates*. NASA-SP-160, National Aeronautics Space Administration.

Liu, W. K., S. Jun, and Y. F. Zhang (1995). Reproducing kernel particle methods. *International Journal for Numerical Methods in Engineering 20*, 1081–1106.

Lo, S. H. (1989, November). Delaunay triangulation of non-convex planar domains. *Internat. J. Numer. Methods Eng. 28*(11), 2695–2707.

Loop, C. T. and T. D. DeRose (1989, July). A multisided generalization of Bézier surfaces. *ACM Transactions on Graphics 8*(3), 204–234.

Lucy, L. B. (1977). A numerical approach to the testing of fusion process. *The Astronomical Journal 88*, 1013–1024.

Lyness, J. N. and D. Jespersen (1975). Moderate degree symmetric quadrature rules for the triangle. *Journal of the Institute of Mathematics and its Applications 15*, 19–32.

Mackinnon, R. J. and G. F. Carey (1987). Treatment of material discontinuities in finite element computations. *International Journal for Numerical Methods in Engineering 24*, 393–417.

Malkus, D. S. and T. J. R. Hughes (1978). Mixed finite element methods—reduced and selective integration techniques: A unification of concepts. *Computer Methods in Applied Mechanics and Engineering 15*, 63–81.

Malvern, L. E. (1969). *Introduction to the Mechanics of a Continuous Medium.* Englewood Cliffs, New Jersey: Prentice-Hall.

Melenk, J. M. and I. Babuška (1996). The partition of unity finite element method: Basic theory and applications. *Computer Methods in Applied Mechanics and Engineering 139*, 289–314.

Moran, B. and C. F. Shih (1987). Crack tip and associated domain integrals from momentum and energy balance. *Engineering Fracture Mechanics 27*(6), 615–641.

Mulmuley, K. (1994). *Computational Geometry: An Introduction Through Randomized Algorithms.* Englewood Cliffs, NJ: Prentice Hall.

Mura, T. (1987). *Micromechanics of Defects in Solids.* The Hague, Netherlands: Martinus Nijhoff.

Nayroles, B., G. Touzot, and P. Villon (1992). Generalizing the finite element method: Diffuse approximation and diffuse elements. *Computational Mechanics 10*, 307–318.

Oñate, E., S. Idelsohn, O. C. Zienkiewicz, R. L. Taylor, and C. Sacco (1996). A stabilised finite point method for analysis of fluid mechanics problems. *Computer Methods in Applied Mechanics and Engineering 139*, 315–346.

Okabe, A., B. Boots, and K. Sugihara (1992). *Spatial Tessellations: Concepts and Applications of Voronoi Diagrams.* Chichester, England: John Wiley & Sons.

O'Rourke, J. (1994). *Computational Geometry in C.* Cambridge University Press.

Owens, S. J. (1992). An implementation of natural neighbor interpolation in three dimensions. Master's thesis, Brigham Young University.

Peano, A. (1979). Conforming approximations for Kirchhoff plates and shells. *International Journal for Numerical Methods in Engineering 14*, 1273–1291.

Perez, C. and L. Traversoni (1996). Finite element simulation of shallow waters using natural neighbors techniques. In *Computational Methods in Surface Flows and Transport Problems: Internation Conference on Computational Methods in Water Resources*, Volume 2, pp. 239–245.

Pian, T. H. H. and K. Sumihara (1984). Rational approach for assumed stress elements. *International Journal for Numerical Methods in Engineering 22*, 173–181.

Piper, P. (1993). Properties of local coordinates based on Dirichlet tessellations. In G. Farin, H. Hagen, and H. Noltemeier (Eds.), *Geometric Modelling*, Volume 8, Wien New York, pp. 227–239. Springer-Verlag.

Powell, M. J. and M. A. Sabin (1977). Piecewise quadratic approximations on triangles. *ACM Transactions on Mathematical Software 3*, 316–325.

Powell, M. J. D. (1987). Radial basis functions for multivariable interpolation. In *Algorithms for Approximations*, Clarendon Press, pp. 143–168.

Preparata, F. and M. Shamos (1985). *Computational Geometry: An Introduction.* New York, N.Y.: Springer-Verlag.

Reddy, B. D. (1998). *Introductory Functional Analysis: With Applications to Boundary Value Problems and Finite Elements.* New York: Springer-Verlag.

Rippa, S. (1984). Interpolation and smoothing of scattered data by radial basis functions. Master's thesis, Tel Aviv University.

Robinson, J. A. (1995). Image coding with ridge and valley primitives. *IEEE Transactions on Communications 43*(6), 2095–2102.

Shamos, M. I. (1978). *Computational Geometry.* Ph.D. thesis, Department of Computer Science, Yale University, New Haven, CT.

Shepard, D. (1968). A two-dimensional interpolation function for irregularly spaced points. In *ACM National Conference*, pp. 517–524.

Shewchuk, J. R. (1996a). *Show Me: A Display Program for Meshes and More.* School of Computer Science, Carnegie Mellon University, Pittsburgh, PA 15213: Available at `http://www.cs.cmu.edu/~quake/showme.html`.

Shewchuk, J. R. (1996b). *Triangle: A Two-Dimensional Quality Mesh Generator and Delaunay Triangulator.* School of Computer Science, Carnegie Mellon University, Pittsburgh, PA 15213: Available at `http://www.cs.cmu.edu/~quake/triangle.html`.

Shewchuk, J. R. (1996c, May). Triangle: Engineering a 2D Quality Mesh Generator and Delaunay Triangulator. In *First Workshop on Applied Computational Geometry*, pp. 124–133. Association for Computing Machinery.

Sibson, R. (1980). A vector identity for the Dirichlet tesselation. *Mathematical Proceedings of the Cambridge Philosophical Society 87*, 151–155.

Sibson, R. (1981). A brief description of natural neighbor interpolation. In V. Barnett (Ed.), *Interpreting Multivariate Data*, Chichester, pp. 21–36. John Wiley.

Simo, J. C. and T. J. R. Hughes (1986). On the variational foundations of assumed strain methods. *Journal of Applied Mechanics 53*(1), 51–54.

Smith, B. T., J. M. Boyle, B. S. Garbow, Y. Ikebe, V. C. Klema, and C. B. Moler (1974). *Matrix Eigensystem Routines—EISPACK Guide.* New York: Springer-Verlag.

Strang, G. and G. Fix (1973). *An Analysis of the Finite Element Method.* Englewood Cliffs, N.J.: Prentice-Hall.

Stroud, A. H. (1971). *Approximate Calculation of Multiple Integrals.* Englewood Cliffs, N.J.: Prentice-Hall.

Sukumar, N. (1998). Mixed formulation for the natural element method in linear elasticity. in preparation.

Sukumar, N. and B. Moran (1998, April). C^1 natural neighbor interpolant for partial differential equations. *Numerical Methods for Partial Differential Equations*. submitted.

Sukumar, N., B. Moran, and T. Belytschko (1998, March). The natural element method in solid mechanics. *International Journal for Numerical Methods in Engineering*. accepted for publication.

Sulsky, D., Z. Chen, and H. L. Schreyer (1994). A particle method for history-dependent materials. *Computer Methods in Applied Mechanics and Engineering 118*, 179–186.

Suri, M. (1996). Analytical and computational assessment of locking in the *hp* finite element method. *Computer Methods in Applied Mechanics and Engineering 133*, 347–371.

Szabó, B. and I. Babuška (1991). *Finite Element Analysis*. New York: John Wiley and Sons.

Tada, H., P. C. Paris, and G. R. Irwin (1977). *The Stress Analysis of Cracks Handbook*. St. Louis, MO: Del Research Corporation.

Timoshenko, S. P. and J. N. Goodier (1970). *Theory of Elasticity* (Third ed.). New York: McGraw Hill.

Timoshenko, S. P. and S. Woinowsky-Krieger (1959). *Theory of Plates and Shells* (Second ed.). New York: McGraw Hill.

Traversoni, L. (1993). An algorithm for natural spline interpolation. *Numerical Algorithms 5*, 63–70.

Traversoni, L. (1994). Natural neighbor finite elements. In *International Conference on Hydraulic Engineering Software, Hydrosoft Proceedings*, Volume 2, pp. 291–297. Computational Mechanics Publications.

Traversoni, L. and O. Palacios (1991). A building method for hierarchical covering spheres of a given set of points. In P. J. Laurent, A. L. Méhauté, and L. L. Schumaker (Eds.), *Curves and Surfaces*, Boston, MA, pp. 457–460. Academic Press.

Voronoi, G. M. (1908). Nouvelles applications des paramètres continus à la théorie des formes quadratiques. deuxième Mémoire: Recherches sur les parallélloèdres primitifs. *J. Reine Angew. Math. 134*, 198–287.

Washizu, K. (1982). *Variational methods in elasticity and plasticity* (Third ed.). Oxford: Pergamon Press.

Watson, D. F. (1981). Computing the n-dimensional Delaunay tessellation with application to Voronoi polytopes. *The Computer Journal 24* (2), 167–172.

Watson, D. F. (1988). Natural neighbor sorting on the N-dimensional sphere. *Pattern Recognition 21*(1), 63–67.

Watson, D. F. (1992). *Contouring: A Guide to the Analysis and Display of Spatial Data*. Oxford: Pergamon Press.

Watson, D. F. (1994). *nngridr: An implementation of natural neighbor interpolation*. David Watson.

Watson, D. F. and G. M. Philip (1987). Neighborhood-based interpolation. *Geobyte 2*(2), 12–16.